General Disclaimer

One or more of the Following Statements may affect this Document

- This document has been reproduced from the best copy furnished by the organizational source. It is being released in the interest of making available as much information as possible.

- This document may contain data, which exceeds the sheet parameters. It was furnished in this condition by the organizational source and is the best copy available.

- This document may contain tone-on-tone or color graphs, charts and/or pictures, which have been reproduced in black and white.

- This document is paginated as submitted by the original source.

- Portions of this document are not fully legible due to the historical nature of some of the material. However, it is the best reproduction available from the original submission.

NASA Contractor Report 167897

CREEP CRACK-GROWTH: A NEW PATH-INDEPENDENT INTEGRAL ($\underline{T}_c$), AND COMPUTATIONAL STUDIES

R. B. Stonesifer and S. N. Atluri

Georgia Institute of Technology
Atlanta, Georgia

July 1982

Prepared for

Table of Contents

i

SECTION I

INTRODUCTION

Fracture Problems and Fracture Criteria: A Review

Characterizing the displacement, stress and strain fields associated
with stationary and propagating cracks in solids characterized by various
idealized constitutive relations is one of the most important areas of study
in fracture mechanics. The importance of these studies is not only that we can
predict the stress or displacement fields in a cracked body, but also that
knowing the nature of such fields we can possibly correlate observed fracture
behavior with some aspect of these fields and thus arrive at valid fracture
criteria.

Criteria for Crack Growth Initiation

The two macroscopic aspects of fracture for which correlations are commonly
sought are the initiation of crack growth and the rate of crack growth. The
most notable initiation correlations are with the elastic stress intensity
factor, K_I, for the elastic (and/or small scale yielding) case [1,2] and with
the J_1-integral for cases in which plasticity may not be limited to the crack-
tip [3,4]. The conditions under which these correlations are independent of·
geometry are discussed in the cited references. The critical values of K_I and
J_1 for a given material are denoted K_{Ic} and J_{1c}, respectively. It is implied
by the use of the subscripts "I" and "1" that these criteria are for the crack

opening mode (i.e., mode I). While similar criteria might be expected for the sliding and tearing modes (i.e., modes II and III), the experimental data for such studies is lacking.

Both K_I and J_1 have been shown to be crack-tip field parameters and both can be evaluated experimentally through energy considerations. The linear elastic, mode I crack-tip field determined in [5] shows that the asymptotic crack-tip fields are proportional to K_I. Similarly, the asymptotic, mode I, crack-tip fields for power-law deformation theory plasticity have been shown [6,7] to depend upon the single parameters J_1.[1] In the case of small scale yielding, K_I is easily related to the energy release rate, G_I [8], which is a measure of the potential energy decrease due to an increase in crack length. The quantity J_1 has a similar potential energy interpretation in the case of deformation theory plasticity, and becomes identical to G_I for small scale yielding of a stationary crack.

In the foregoing discussion, the time dependence of the material's response and of the applied loading is assumed to be negligible. For creep crack growth these assumptions are no longer valid. We now consider crack growth initiation in materials which exhibit creep behavior. While a significant number of creep fracture experiments have been reported in the literature, it appears that the primary interest has been to find a creep crack growth rate criterion as opposed to an initiation criterion. As a result of this emphasis, many investigators use notched specimens rather than precracked specimens and many do not report data which could be useful in addressing the question of initiation. At present there seems to be some indication [9,10] that when precracked specimens are used, the time required for creep crack growth initiation is negligible when

---

[1] The deformation theory of plasticity precludes elastic unloading from an elastic-plastic state and thus is mathematically equivalent to nonlinear elasticity. The crack-tip fields associated with power-law deformation plasticity are commonly referred to as HRR fields after the authors of references [6] and [7].

compared to the life of the specimen. It should be understood that this is not a universally acknowledged conclusion [11] and that further study is indicated.

As noted previously, the second macroscopic aspect of fracture for which correlations with crack-tip fields are commonly sought is crack growth or propagation. The following summarizes the development of criteria relating to this aspect.

Criteria for Crack Propagation

Slow crack growth occurring under constant load implies that the material response is time dependent and is generally classified as creep crack growth. If the material's time dependent nature is negligible under the subject conditions, then it is assumed that crack growth requires an increase in applied load. This latter case is typical of situations in which small scale yield conditions are not met and for which J_1 has been found to correlate with crack growth initiation. The primary interest in this quasi-static mode of crack growth is that for some materials and geometries, the increase in load carrying capacity of the structure during quasi-static crack growth is significant. This implies that design procedures can be developed to take advantage of this added margin of safety. To justify such a procedure, however, there must be some dependable means of predicting the crack growth versus load behavior as well as predicting at what load the crack becomes unstable (i.e., is no longer quasi-static). As noted, J_1 is generally accepted as a valid initiation criterion for this problem. For prediction of the subsequent growth, however, there are at least two proposed criteria which appear to provide reasonable correlations with experimental data. The first growth criterion can be stated as $J_1 = J_{1R}(\Delta a)$, where $J_{1R}(0) = J_{1c}$ and $J_{1R}(\Delta a)$ is assumed to be a material property which depends on the amount of crack growth, a [12,13]. The subscript "R" denotes that this quantity characterizes the material's resistance to cracking. While strong theoretical

- 3 -

arguments can be given as to why this criterion should not be valid (except possibly for very limited amounts of crack growth [14]), it has been demonstrated that reasonable predictions can result from the use of this criterion for at least some classes of problems [12,15].

Based on the theoretical objections to the use of J_{1R} except for limited crack growth, a second criterion which is based on the crack-tip deformation has been proposed [16,17]. This criterion results from finite element simulations of quasi-static crack growth experiments which indicate that the crack-tip opening angle, CTOA (defined by the first finite element behind the crack-tip) becomes constant during crack growth. Whereas the CTOA, so defined, is clearly a mesh dependent quantity, the concept of crack-tip deformations becoming constant with crack growth is physically meaningful. The procedure for applying this criterion in finite element based predictions of crack growth behavior is to use J_{1c} for initiation and J_{1R} for crack growth prediction until the computed CTOA has become constant with crack growth. Continued growth is then governed by this constant value of CTOA. Alternatively, a predetermined CTOA resistance curve can be used throughout growth. Crack growth instability is assumed to occur (for either CTOA or J_{1R} as the criterion) when further increase in crack length results in the criterion for growth being exceeded without further increase in applied loading. The J_{1R} and CTOA criteria appear to provide reasonable correlation of ductile slow crack growth behavior for a variety of materials, geometries and load conditions [15,18,19].

Creep crack growth generally becomes a concern when components are operated at elevated temperatures. Whereas quasi-static crack growth can be on the order of mm/sec, typical creep crack growth rates are on the order of μm/sec. Compared to elastic-plastic quasi-static crack growth, the problem of creep crack initiation and growth is a relatively new area of study.

- 4 -

Numerous experimental studies have been undertaken with the purpose of finding a parameter which correlates with creep crack propagation rate. (See, for example, the review article [20] and [21-24].) Most of these investigations consider as candidate parameters, K_I, some form of net section (or reference) stress, and in more recent studies C^*. The C^* parameter is the steady-state creep analogue of J_1 (in the sense of [25]) in that the definition of C^* is the same as that for J_1 except displacements and strains are replaced by their respective rates [26].

It is illustrated in Fig. 1.1 that the above three parameters can be expected to correlate three distinctly different creep crack growth situations. In Fig. 1.1a, a crack and its associated ligament are shown for a material and geometry which results in negligible creep strains everywhere except in the vicinity of the crack-tip. This condition is analogous to that of small scale yielding in elastic-plastic fracture. Fig. 1.1b represents a situation in which C^* might be considered an appropriate parameter. This situation is characterized (i) by the body being essentially at steady-state creep conditions (which implies very slow crack propagation) and (ii) by the creep-damage process-zone being local to, and therefore controlled by, the crack-tip field. Fig. 1.1c illustrates the type of situation for which net section stress might be expected to control crack growth. In this case, the main feature is the widespread creep damage zone.

It is seen from Fig. 1.1 that intermediate situations can occur. For example, suppose a particular material and geometry results in a crack propagation rate such that elastic strain rates are not negligible compared to creep strain rates (i.e., nonsteady creep) and at the same time, creep strains are no longer localized to the crack-tip region. While neither K_I or C^* could be valid parameters for this case, it appears reasonable to expect that crack growth

elastic

creep zone

a. K_I,$(\Delta T)_c$ controlled behavior

steady-state creep

creep damage process zone

b. C^*,$(\Delta T)_c$ controlled behavior

c. σnet controlled behavior
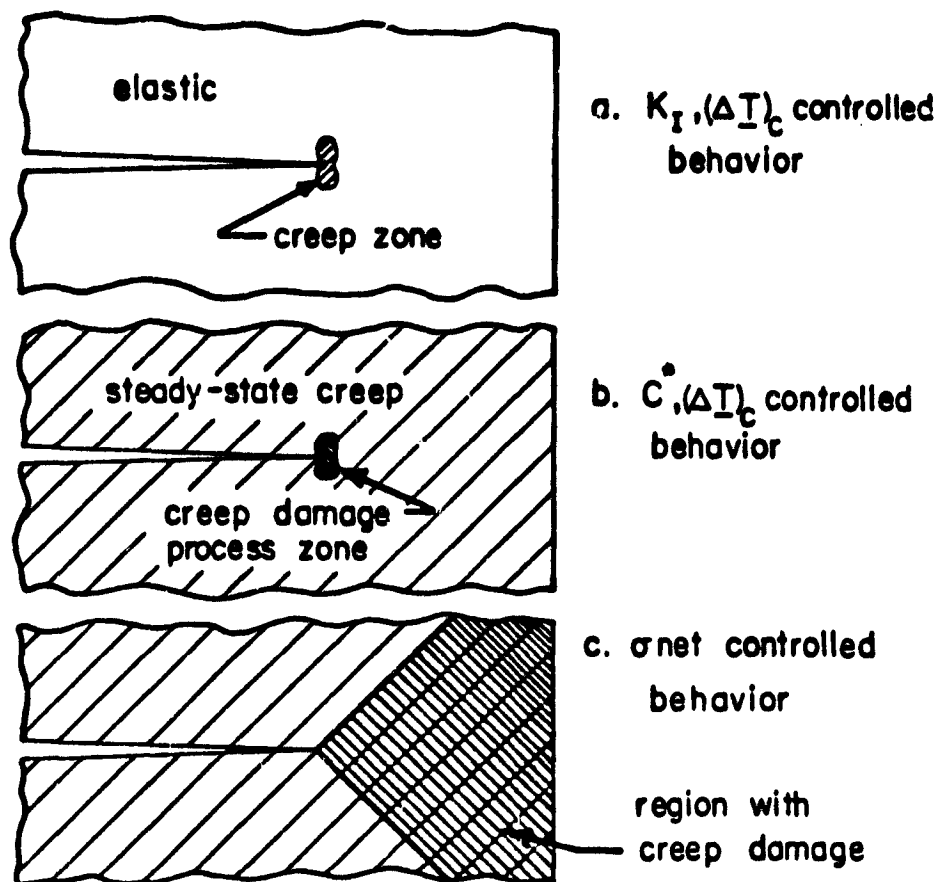
region with creep damage

Fig. 1.1   Conditions for which creep crack growth parameters are expected to be valid

- 6 -

rate is still determined by the local crack-tip field since the creep damage process zone is still assumed to be local to the crack-tip.

A parameter which is apparently capable of spanning the gap between K_I controlled growth and C^* controlled growth has been introduced [27]. This parameter is referred to as $(\Delta \underline{T})_c$ and is defined by a path-independent vector integral. A detailed discussion of a generalized C^* (i.e., $\underline{C}^*$) and $(\Delta \underline{T})_c$ is given in Section II of this work with a principal result being that the energy relationship commonly used for experimental measurement of C^* does not apply to C^* but rather applies to the $(\Delta \underline{T})_c$ parameter. This means that the experimental results are actually showing a correlation with $(\Delta \underline{T})_c$ rather than with C^*. Based on the theoretical validity of $(\Delta \underline{T})_c$ as a crack-tip field parameter for nonsteady as well as steady-state creep and based on the mounting experimental evidence that crack propagation rate correlates well with $(\Delta \underline{T})_c$, it seems the creep crack growth rate problem is close to having a solution.

Motivation for the Present Work

In the following, we review previous studies to the extent required to place the present study in perspective and briefly introduce the present work. The nonlinear nature of creep constitutive relations precludes analytical solutions for either stationary or propagating cracks in a creeping material. For stationary cracks in a power-law creep material, however, it is known that the HRR fields are present in the vicinity of the crack-tip [26]. (Since the singularity in creep strain rates is greater than that in the stresses, and thus elastic strains, it follows that the HRR field exists at the crack-tip during nonsteady as well as steady-state creep.) For propagating cracks, it appears that the HRR fields no longer exist at the crack-tip, but that analytical tools exist to determine the fields which do exist [28,]9]. While knowledge of the crack-tip field is

valuable, the solution of boundary value problems must depend on numerical methods. The finite element method, in particular, shows promise for solving creep crack growth problems.

Only a few studies on finite element modeling of creep crack growth have been reported. The earliest is apparently that of Ohtani and Nakamura [30]. This study simulated crack growth with a node-release technique and assumed a critical crack-tip plastic strain criterion for creep crack growth. The rate constitutive law contained an elastic term and a creep term based on the generalization of the uniaxial Norton power law.

Hinnerchs [31] uses the Bodner-Partom constitutive law [32] and a node-release technique for modeling crack growth. In this work, several candidate criteria are examined by simulating crack growth experiments. Due to the apparently limited crack growth (<0.5 mm), the short test durations (one hour) and the lack of crack growth measurement data (which requires the development of a so-called hybrid experimental-numerical procedure to estimate the crack growth history), it seems the general applicability of the conclusions from this study are questionable. It also seems likely that the methods for evaluating C* in this study are incorrect[1] and thus the conclusions concerning C* should be regarded accordingly.

Ehlers and Riedel [33] have conducted a finite element analysis of a stationary crack in a compact specimen. The primary emphasis in this study is on the nature of the crack-tip field during the transition from the initial elastic field to the steady-state creep field.

---

[1] While the details of the numerical procedures for evaluating C* are not given in [31], it appears that the W* term of C* (see Section II) is incorrectly interpreted as a history dependent quantity as opposed to a quantity dependent solely on the steady-state stress and strain rate.

The strength of the HRR field during the transition period is determined through fitting the near tip equivalent stress field. The calculations use eight-noded isoparametric elements with quarter-point elements being used at the crack-tip so as to have an $r^{-1/2}$ strain singularity. Creep crack growth and creep crack growth criteria are not considered in this study.

The finite element equations for the creep crack growth model being used in the present study are derived from the principle of virtual work in Section III. Section V presents the results of several analyses involving both stationary cracks and propagating cracks. The creep crack growth simulation is via a mesh shifting/remeshing procedure. Calculations are made using the quarter-point element technique as well as with a specially developed (Section IV) compatible element which incorporates the HRR, $r^{-n/(1+n)}$, strain singularity.

An important aspect of the current work is the study of the $(\Delta \underline{T})_c$ parameter. In particular, the meaning of $(\Delta \underline{T})_c$, its relationship to C_1^*, and its calculation within the context of finite element analysis are explored in depth.

A series of crack propagation calculations are combined with analytical and experimental results in Section V to show that creep crack growth in 304 stainless steel at 650^0C occurs under essentially steady-state creep conditions. This implies that the crack growth rate for a given crack length and load can be determined from a steady-state creep solution which does not depend on the previous load and crack growth histories. This observation implies that simple crack growth prediction methodologies may be developed.

SECTION II

DERIVATION OF THE $(\Delta \underline{T})_c$, $\underline{J}$ AND $\underline{C}^*$ INTEGRALS

Preliminaries

We shall consider problems which exhibit the following constitutive behavior:

$$\dot{\epsilon}_{ij} = \dot{\epsilon}^e_{ij} + \dot{\epsilon}^c_{ij} = L_{ijk\ell}\overset{*}{\sigma}_{k\ell} + (3/2)\gamma(\sigma_{eq})^{n-1}\sigma'_{ij} \tag{2.1}$$

We denote the cartesian coordinates of the undeformed body as x_i. Defining $\dot{u}_i$ as the rate of displacement (or velocity) of a material particle from the current configuration, then $\dot{\epsilon}_{ij}$ is the symmetric part of the rate of displacement gradient $\dot{e}_{ij} \equiv (\underline{\nabla}_t\dot{\underline{u}})^T = \frac{\partial\dot{u}_i}{\partial y_j} \equiv \dot{\epsilon}_{ij} + \dot{\omega}_{ij}$. The gradient operator $\underline{\nabla}_t$ is with respect to the current coordinates y_i where it is understood that $y_i = x_i + u_i$. $L_{ijk\ell}$ is the tensor of instantaneous elastic moduli. We let $\overset{*}{\sigma}_{k\ell}$ denote the corotational rate (or "Zaremba-Jaumann rate") of the Kirchhoff stress σ_{ij} where σ_{ij} is related to the Cauchy stress τ_{ij} by $\sigma_{ij} = J\tau_{ij}$ ($J = \det[\frac{\partial y_m}{\partial x_n}]$). The equivalent Kirchhoff stress σ_{eq} is related to the deviatoric Kirchhoff stress σ'_{ij} ($= \sigma_{ij} - 1/3\,\sigma_{kk}\delta_{ij}$) by $\sigma_{eq} = (3/2)(\sigma'_{ij}\sigma'_{ij})^{1/2}$. The parameters γ and n are those of the familiar Norton's law

$$\dot{\epsilon}_{eq} = \gamma(\sigma_{eq})^n$$

were

$$\dot{\epsilon}_{eq} = [(2/3)\dot{\epsilon}_{ij}\dot{\epsilon}_{ij}]^{1/2}$$

We will use the notation: $(\underset{\sim}{\ })$ denotes a second order tensor; $(\underline{\ })$ implies a vector; $\underline{a} = \underset{\sim}{B} \cdot \underline{c}$ implies $a_i = B_{ij}c_j$; $\underset{\sim}{A} = \underset{\sim}{B} \cdot \underset{\sim}{C}$ implies $A_{ij} = B_{ik}C_{kj}$; $\underset{\sim}{A} : \underset{\sim}{B} = A_{ij}B_{ij}$. Also note that $\underline{\nabla}_t \underset{\sim}{B} : \underset{\sim}{C}$ implies $\dfrac{\partial B_{ik}}{\partial y_i} C_{jk}$ and $\underline{\nabla}_t \cdot \underset{\sim}{B}$ implies $\dfrac{\partial B_{ij}}{\partial y_i}$.

A Conservation Law for Finite Elastic and
Nonsteady Creep Material Behavior

The discovery of conservation laws and the possibility of deriving path-independent integrals from these laws are not particularly recent occurrences as discussed in [34]. However, the literature in this area has been rather piece-meal and therefore difficult to assimilate. The recent work of Atluri [27] has done much to unify and generalize this subject and is the basis for the following presentation.

We will consider a very general conservation law which has been given by Atluri, but will limit our discussion of this law to materials characterized by (2.1). We will use cartesian coordinates exclusively. Note that by special selection of material constants (i.e., $\gamma=0$), (2.1) can be specialized to elasticity. Alternatively, by assuming that the stresses are invariant with time, (2.1) can be specialized to steady-state creep behavior.

In the following presentation, the current configuration (i.e., the config-uration at time t) is the reference configuration. There may be initial stresses existing for this reference configuration. If stresses do exist, then they are assumed to satisfy the linear and angular momentum balance condition (i.e., equilibrium)

$$\underline{\nabla}_t \cdot \underset{\sim}{\tau} + \rho_t(\underline{f}_t - \underline{a}_t) = 0; \quad \underset{\sim}{\tau} = \underset{\sim}{\tau}^T$$

where ρ_t, $\underline{f}_t$ and $\underline{a}_t$ are the current mass density, body force vector and accel-eration vector.

A conservation integral relation given by Atluri [27] for a closed volume V_t (at the current time, t), which is free from singularities and any other defects (which would preclude the application of the divergence theorem), is:

$$\underline{0} = \int_{V_t} (\underline{\nabla}_t \Delta W - (\underline{\nabla}_t \underline{\tau}):\Delta\underline{e} - \underline{\nabla}_t \cdot [(\underline{\tau}+\Delta\underline{t}) \cdot \Delta\underline{e}] \tag{2.2}$$

$$- \rho_t(\underline{f}-\underline{a}) \cdot \Delta\underline{e})dV + \int_{S_t} [\underline{n}_t \cdot (\underline{\tau}+\Delta\underline{t}) - \underline{\bar{t}}] \cdot \Delta\underline{e}dS$$

$$+ \int_{S_e} \underline{n}_t \cdot (\underline{\tau}+\Delta\underline{t}) \cdot (\Delta\underline{e}-\Delta\underline{\bar{e}})dS$$

In (2.2), $\Delta\underline{t}$ is the incremental first-Piola-Kirchhoff (nonsymmetric) stress ($\Delta\underline{t} = [\Delta\underline{\sigma} - \Delta\underline{e} \cdot \underline{\sigma}]/J$) where $\Delta\underline{\sigma}$ is the material increment of Kirchhoff stress. The current mass density is denoted ρ_t, and $\underline{f}$ and $\underline{a}$ are the body force and acceleration vectors at time $t+\Delta t$, respectively. S_t and S_e are the portions of the boundary of V_t upon which prescribed tractions, $\underline{\bar{t}}$, are acting and at which prescribed displacement gradients, $\Delta\underline{\bar{e}}$, exist, respectively. The current outward normal to S_t or S_e is $\underline{n}_t$. The quantity ΔW, discussed in detail in [27], is the incremental stress-working density in time Δt, and is given by:

$$\Delta W = \underline{\tau}:\Delta\underline{e} + \frac{1}{2}\Delta\underline{t}^T:\Delta\underline{e} \equiv \underline{\tau}:\Delta\underline{e} + \Delta U \tag{2.3}$$

where

$$\Delta U = \frac{1}{2}\Delta\underline{t}^T:\Delta\underline{e} \tag{2.4}$$

The validity of (2.2) is readily verified through the two identities [27]:

$$\underline{\nabla}_t \Delta W = \underline{\nabla}_t(\underline{\tau}:\Delta\underline{e}) + \underline{\nabla}_t \Delta U = \underline{\nabla}_t \underline{\tau}:\underline{e} \tag{2.5}$$

$$+ \underline{\nabla}_t \Delta\underline{e}:\underline{\tau} + \underline{\nabla}_t \Delta\underline{e}:\Delta\underline{t}^T$$

and

$$\underline{\nabla}_t \cdot [(\underline{\tau}+\Delta\underline{t}) \cdot \Delta\underline{e}] = [\underline{\nabla}_t \cdot (\underline{\tau}+\Delta\underline{t})] \cdot \Delta\underline{e} + \underline{\nabla}_t \Delta\underline{e}:(\underline{\tau}+\Delta\underline{t})^T \tag{2.6}$$

the satisfaction of linear momentum balance in V_t:

$$\underline{\nabla}_t \cdot [\underline{\tau} + \Delta\underline{\tau}] + \rho_t(\underline{f} - \underline{a}) = 0 \qquad (2.7)$$

and the satisfaction of the boundary conditions:[1]

$$\underline{n}_t \cdot [\underline{\tau} + \Delta\underline{\tau}] = \underline{\bar{t}} \text{ on } S_t \qquad (2.8)$$

$$\Delta\underline{e} = \Delta\underline{\bar{e}} \text{ on } S_e \qquad (2.9)$$

Note that identity (2.5) assumes that $\underline{\tau}$ (the initial stress for the increment) is an explicit function of its position in V_t. The existence of ΔU is shown and discussed in the work of Atluri [:5].

Having the relation (2.2) it is now possible to specialize this relation to finite elastic behavior or to steady-state creep behavior. However, since we are primarily interested in the path-independent integrals which can be obtained from (2.2) we will postpone the specialization till after we have derived the general path-independent integral $(\Delta\underline{T})_c$.

Path-Independent Integrals for Fracture Analysis

The conservation integral (2.2) is used [27] to obtain a path-independent integral which is applicable to the analysis of cracks by considering a volume $V_t - V_\epsilon$ such as illustrated in Fig. 2.1. (Note that a two-dimensional case is illustrated for simplicity). The use of the divergence theorem for the region depicted in Fig. 2.1 results in (2.2) being rewritten

$$\int_{\Gamma_{234}} [\underline{n}_t \Delta W - \underline{n}_t \cdot (\underline{\tau} + \Delta\underline{\tau}) \cdot \Delta\underline{e}] dS \qquad (2.10)$$

$$+ \int_{V_t - V_\epsilon} [(-\underline{\nabla}_t \underline{\tau}) : \Delta\underline{e} - \rho_t(\underline{f} - \underline{a}) \cdot \Delta\underline{e}] dV$$

[1] The validity of (2.2) does __not__ require $S_t + S_e = \partial V_t$ where ∂V_t denotes the surface bounding V_t. Therefore, ∂V_t need not coincide with the boundary of the body under consideration.

$$+ \int_{\Gamma_{12}} \underline{n}_t \Delta W dS + \int_{\Gamma_{45}} \underline{n}_t \Delta W dS - \int_{S_t} \bar{\underline{t}} \cdot \Delta \underline{e} dS$$

$$- \int_{S_e} \underline{n}_t \cdot (\underline{\tau} + \Delta \underline{\tau}) \cdot \Delta \bar{\underline{e}} dS$$

$$= \int_{\Gamma_\epsilon} [\underline{n}_t \Delta W - \underline{n}_t \cdot (\underline{\tau} + \Delta \underline{\tau}) \cdot \Delta \underline{e}] dS \equiv (\Delta \underline{T})_c^\epsilon \qquad (2.10)$$

In writing (2.10) it has been assumed that $S_e + S_t = \Gamma_{12} + \Gamma_{45}$, which implies that Γ_{234} does not coincide with any exterior boundaries. This has been assumed purely for convenience of notation. We have also used the notation $\Gamma_\epsilon = \Gamma_{165}$. Noting that (2.10) contains two equalities, it can be verified by inspection that $(\Delta \underline{T})_c^\epsilon$ depends on ϵ (or more generally Γ_ϵ) but that it does not depend on the selection of Γ_{234}. In this sense $(\Delta \underline{T})_c^\epsilon$ is path-independent (i.e., independent of the selected far-field path). Following the reasoning of Atluri [27], we define $(\Delta T)_c$ as the limit of $(\Delta \underline{T})_c^\epsilon$ as ϵ goes to zero.[1]

$$(\Delta \underline{T})_c = \underset{\epsilon \to 0}{Lt} \int_{\Gamma_\epsilon} [\underline{n}_t \Delta W - \underline{n}_t \cdot (\underline{\tau} + \Delta \underline{\tau}) \cdot \Delta \underline{e}] dS \qquad (2.11)$$

$$\equiv \int_{\Gamma_{234}} [\underline{n}_t \Delta W - \underline{n}_t \cdot (\underline{\tau} + \Delta \underline{\tau}) \cdot \Delta \underline{e}] dS$$

$$+ \underset{\epsilon \to 0}{Lt} \left\{ \int_{V_t - V_\epsilon} [(-\underline{\nabla}_t \cdot \underline{\tau}) : \Delta \underline{e} - \rho_t (\underline{f} - \underline{a}) \cdot \Delta \underline{e}] dV \right.$$

$$+ \int_{\Gamma_{12}} \underline{n}_t \Delta W dS + \int_{\Gamma_{45}} \underline{n}_t \Delta W dS - \int_{S_t} \bar{\underline{t}} \cdot \Delta \underline{e} dS$$

$$\left. - \int_{S_e} \underline{n}_t \cdot (\underline{\tau} + \Delta \underline{\tau}) \cdot \Delta \bar{\underline{e}} dS \right\}$$

---

[1] The existence of the limit is shown in Appendix A.
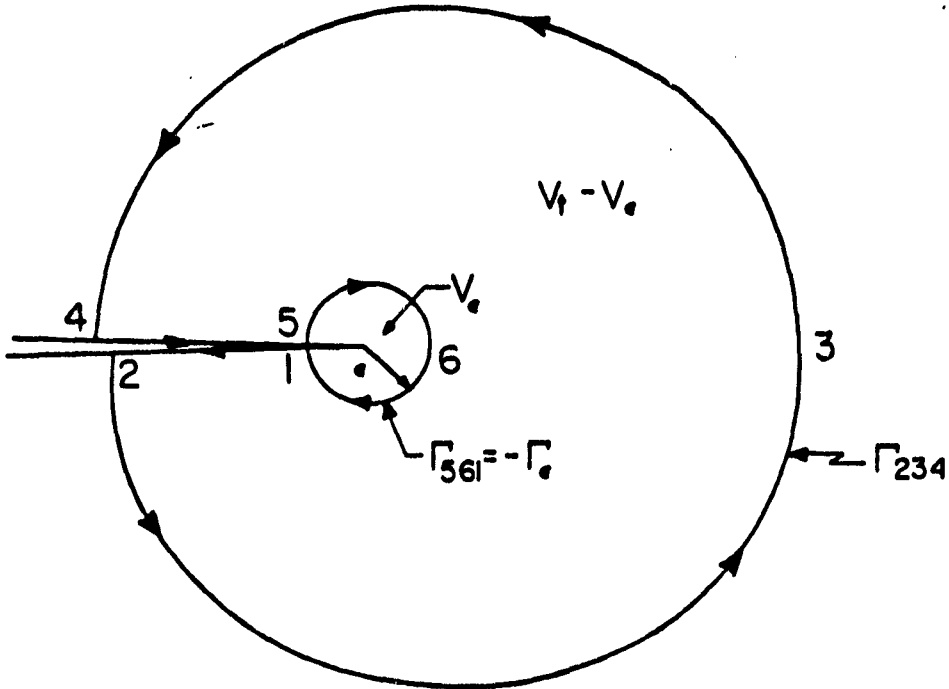
- 14 -

Fig. 2.1   Contours for applying the conservation law to
a two-dimensional, cracked body

By defining $(\Delta \underline{T})_c$ as the limit of $(\Delta \underline{T})_c^\epsilon$ as ϵ goes to zero, it is seen that $(\Delta \underline{T})_c$ is entirely determined by the asymptotic near-tip fields. It will be shown later that the converse to this statement is also valid when the near-tip fields are the HRR fields. That is, it will be shown that $(\Delta \underline{T})_c$ entirely determines the asymptotic near-tip fields.

Often it happens that only the first component of the vector quantity $(\Delta \underline{T})_c$ is of interest. We will write the first component of $(\Delta \underline{T})_c$ as $(\Delta T_1)_c$. Also, the quantities $(\dot{\underline{T}})_c$ and $(\dot{T}_1)_c$ will often be used in place of $(\Delta \underline{T})_c$ and $(\Delta T_1)_c$. These quantities are related by

$$(\dot{\underline{T}})_c = \lim_{\Delta t \to 0} \frac{(\Delta \underline{T})_c}{\Delta t} \tag{2.12}$$

However, in the presentation of numerical evaluations of $(\Delta T_1)_c$ we use $(\dot{T}_1)_c$ as a convenient, approximate notation for $(\Delta T_1)_c / \Delta t$.

We now consider two special cases of (2.11). For symmetrical deformation about the x_1 axis and cracks oriented along the x_1 axis with traction free crack surfaces, no body forces and negligible inertial effects, the first component of $(\Delta \underline{T})_c$ is

$$(\Delta T_1)_c = \lim_{\epsilon \to 0} \int_{\Gamma_\epsilon} [n_1 \Delta W - n_j (\tau_{ji} + \Delta t_{ji}) \Delta e_{i1}] dS \tag{2.13}$$

$$= \int_{\Gamma_{234}} [n_1 \Delta W - n_j (\tau_{ji} + \Delta t_{ji}) \Delta e_{i1}] dS$$

$$- \int_{V_t} \frac{\partial \tau_{i1}}{\partial y_1} \Delta e_{ji} dV$$

Note that the limit of the volume integral has been written in its explicit form as a result of the arguments for the existence of this limit, given in Appendix A. If, in addition to the above conditions, the strains are infinitesimal and the deformations small, then there is no need to differentiate

- 16 -

between x_1 and y_1, Δt_{j1} becomes identical to $\Delta \tau_{ij}$ and we have (recalling $\Delta e_{ij} = \partial \Delta u_i / \partial y_j$):

$$(\Delta T_1)_c = \underset{\epsilon \to 0}{\text{Lt}} \int_{\Gamma_\epsilon} [n_1 \Delta W - n_j(\tau_{j1} + \Delta \tau_{j1}) \frac{\partial \Delta u_1}{\partial x_1}] dS \qquad (2.14)$$

$$= \int_{\Gamma_{234}} [n_1 \Delta W - n_j(\tau_{j1} + \Delta \tau_{j1}) \frac{\partial \Delta u_1}{\partial x_1}] dS$$

$$- \int_{V_t} \frac{\partial \tau_{ij}}{\partial x_1} \Delta \epsilon_{ij} dV$$

The replacement of Δe_{ij} by $\Delta \epsilon_{ij}$ in the volume integral is made possible by the symmetry of τ_{ij} and thus $\partial \tau_{ij} / \partial x_1$.

Physical Interpretation of $(\Delta \underline{T})_c$

It has been shown by Atluri [27], that the vector $(\Delta \underline{T})_c$ has the following physical meaning. Let two bodies with non-propagating[1] cracks be identical except for the second body having an additional, arbitrarily directed, infinitesimal increment in crack length characterized by the vector $\underline{dc}$. It is assumed that both bodies experience identical load histories. Define total potential energy increments corresponding to the time increment Δt as[2]

$$\Delta E_1 = \Delta \psi_1 + \Delta \Omega_1 + \Delta K_1 \qquad (2.15a)$$

$$\Delta E_2 = \Delta \psi_2 + \Delta \Omega_2 + \Delta K_2 \qquad (2.15b)$$

for the first and second bodies, respectively. In (2.15), $-\Delta \psi$ is the incremental work of external forces, $\Delta \Omega$ is the incremental stress-work and ΔK is the increment in the kinetic energy. (It should be noted that $\Delta \Omega$ includes the inelastically dissipated energy.) Then

---

[1] Atluri [27] has shown that the $1/r$ singularity in kinetic energy, which is associated with dynamically propagating cracks, changes the interpretation.

[2] Note that sign convention for ΔE_1 and ΔE_2 is opposite to [27] so as to conform to conventional usage.

$$(\Delta T_1)_c \, b d c_1 = -(\Delta E_2 - \Delta E_1) \tag{2.16}$$

where b is the length of the crack front.

If one is only interested in self-similar crack extension in the x_1-direction, then $dc_2 = dc_3 = 0$ and

$$(\Delta T_1)_c = -\frac{\Delta E_2 - \Delta E_1}{b d c_1} \tag{2.17}$$

Therefore, $(\Delta \underline{T})_c$ is related to the incremental potential energy difference between two bodies which are identical except for an incremental crack length difference $\underline{dc}$.

Finite Elasticity and $\underline{J}$

As noted previously, the constitutive law (2.1) can be specialized to elastic behavior by choosing γ to be zero. Therefore, $(\Delta \underline{T})_c$ as defined by (2.11) is a valid crack-tip characterizing parameter for general nonlinear elasticity with finite strains, large deformation, body forces and inertial effects. Howerver, the basic premise of elastic behavior is that the constitutive relations are independent of the histories of deformation and stress. This means that the constitutive relations can be derived from a potential. For instance, a potential, U, exists for $\underline{t}$, the first Piola-Kirchhoff stress, such that

$$\underline{t}^T = \frac{\partial U}{\partial \underline{e}} \tag{2.18}$$

In the following, we consider the reference configuration to be the stress-free, undeformed configuration at $t=0$, and therefore drop the subscript t for convenience. As a result of the existence of the relation (2.18), it is possible to state two identities which are analogous to those of (2.5) and (2.6) for the case $\tau \equiv 0$.

$$\underline{\nabla} U = \frac{\partial U}{\partial e_{mn}} \frac{\partial e_{mn}}{\partial x_1} = \underline{\nabla} \underline{e} : \underline{t}^T \tag{2.19}$$

and

$$\underline{\nabla} \cdot [\underline{t} \cdot \underline{e}] = \underline{\nabla} \cdot \underline{t} \cdot \underline{e} + \underline{\nabla}\underline{e} : \underline{t}^T \tag{2.20}$$

Similarly, the linear momentum balance (i.e., equilibrium) condition is now

$$\underline{\nabla} \cdot \underline{t} + \rho(\underline{f} - \underline{a}) = 0 \tag{2.21}$$

and the boundary conditions

$$\underline{n} \cdot \underline{t} = \bar{\underline{t}} \text{ on } S_t \tag{2.22}$$

$$\underline{e} = \bar{\underline{e}} \text{ on } S_e \tag{2.23}$$

Noting the similarity of equations (2.18) through (2.23) with (2.4) through (2.9) it is easy to arrive at the following conservation law

$$\underline{0} = \int_V (\underline{\nabla}U - \underline{\nabla} \cdot [\underline{t} \cdot \underline{e}] - \rho(\underline{f} - \underline{a}) \cdot \underline{e})dV \tag{2.24}$$

$$+ \int_{S_t} [\underline{n} \cdot \underline{t} - \bar{\underline{t}}] \cdot \underline{e}dS + \int_{S_e} \underline{n} \cdot \underline{t} \cdot (\underline{e} - \bar{\underline{e}})dS$$

Following the procedure used in deriving $(\Delta \underline{T})_c$ from (2.2) we apply the divergence theorem to (2.24) for the volume $V - V_\epsilon$ and take the limit as ϵ goes to zero. The path-independent vector quantity resulting from this procedure will be called $\underline{J}$.

$$\underline{J} = \underset{\epsilon \to 0}{Lt} \int_{\Gamma_\epsilon} [\underline{n}U - \underline{n} \cdot \underline{t} \cdot \underline{e}]dS \tag{2.25}$$

$$= \int_{\Gamma_{234}} [\underline{n}U - \underline{n} \cdot \underline{t} \cdot \underline{e}]dS + \underset{\epsilon \to 0}{Lt} \left\{ \int_{V-V_\epsilon} \rho(\underline{a} - \underline{f}) \cdot \underline{e}dV \right.$$

$$+ \int_{\Gamma_{12}} \underline{n}UdS + \int_{\Gamma_{45}} \underline{n}UdS - \int_{S_t} \bar{\underline{t}} \cdot \underline{e}dS - \int_{S_e} \underline{n} \cdot \underline{t} \cdot \bar{\underline{e}}dS \left. \right\}$$

In writing (2.22) through (2.25) it is understood that ρ is the mass density in the reference configuration, $\underline{n}$ is the unit normal in the reference configuration, $\underline{f}$ are arbitrary body forces per unit mass, $\underline{a}$ is the absolute material

acceleration, and $\underline{\bar{t}}$ are prescribed tractions per unit undeformed area S_t.

We now consider several special cases of (2.25). If the problem being considered involves a crack oriented along the x_1 coordinate direction and is loaded so that only mode I crack-tip behavior occurs, then J_1 is of primary interest and we have:

$$J_1 = \int_{\Gamma_{234}} [n_1 U - n_1 t_{ij} e_{j1}] dS + \left. \underset{\epsilon \to 0}{Lt} \right\} \int_{V-V_\epsilon} (a_i - f_i) e_{i1} dV \qquad (2.26)$$

$$- \int_{S_t} \bar{t}_i e_{i1} dS - \int_{S_e} n_1 t_{ij} \bar{e}_{j1} dS \left. \right\}$$

If in addition the problem involves infinitesimal strains, small displacements and traction-free crack surfaces, we have

$$J_1 = \int_{\Gamma_{234}} \left[n_1 U - n_1 \tau_{ij} \frac{\partial u_i}{\partial x_1} \right] dS + \int_V \rho(a_i - f_i) \frac{\partial u_i}{\partial x_1} dV \qquad (2.27)$$

where use has been made of the existence arguments of Appenix A in taking the limit of the volume integral.

For elastic behavior and non-propagating cracks, Atluri [27] shows that $\underline{J}$ has the meaning of energy release rate to a process zone V_ϵ in the sense that:

$$J_k b dc_k = - \left[\frac{DE_\epsilon}{Dt} \right] dt \qquad (2.28)$$

where b is the length of the crack front,

$$\frac{DE_\epsilon}{Dt} = \frac{D\psi_\epsilon}{Dt} + \frac{D\Omega_\epsilon}{Dt} + \frac{DK_\epsilon}{Dt}$$

and

$$\left[\frac{DE_\epsilon}{Dt} \right] dt = E_\epsilon(t + dt) - E_\epsilon(t)$$

For an elasto-dynamically propagat'ng crack (i.e., singular kinetic energy) Atluri [27] concludes that

$$J_k bdc_k = \left[\frac{DL_\epsilon}{Dt}\right] dt \tag{2.29}$$

where L_ϵ is the Lagrangian (i.e., $L_\epsilon \equiv X_\epsilon - \psi_\epsilon - \Omega_\epsilon$) such that

$$\frac{DL_\epsilon}{Dt} = -\frac{D\psi_\epsilon}{Dt} - \frac{D\Omega_\epsilon}{Dt} + \frac{DK_\epsilon}{Dt}$$

Therefore, J_k has the meaning of "rate of change of Lagrangian per unit crack growth".

We now consider the special case of steady-state creep behavior.

Steady-State Creep and C*

It has been shown that $(\Delta \underline{T})_c$ characterizes the crack-tip field for materials which exhibit creep behavior such as in (2.1). It is known that under certain conditions of applied loading, the constitutive relation (2.1) can (after long times) result in a steady-state. This steady-state is primarily charcterized by the time independence of the stresses (i.e., $\Delta U = \Delta t_{ji} = 0$). Specializing (2.13) to steady-state conditions, we define the steady-state value of $(\Delta \underline{T}_1)_c$:

$$(\Delta T_1)_{css} = \underset{\epsilon \to 0}{Lt} \int_{\Gamma_\epsilon} [n_1 \tau_{ij} \Delta e_{ij} - n_j \tau_{ji} \Delta e_{i1}] dS \tag{2.30}$$

$$= \int_{\Gamma_{234}} [n_1 \tau_{ij} \Delta e_{ij} - n_j \tau_{ji} \Delta e_{i1}] dS - \int_{V_t} \frac{\partial \tau_{ij}}{\partial y_1} \Delta e_{ij} dV$$

Because (2.1) results in a power-law relation at steady-state, which is analogous to the power law deformation-theory plasticity (or essentially nonlinear elasticity), Goldman and Hutchinson [26] have suggested a path-independent C_1^* integral,

$$C_1^* = \int_\Gamma \left[n_1 W^* - n_j \tau_{ij} \frac{\partial \dot{u}_i}{\partial x_1}\right] dS \tag{2.31}$$

where

$$W^* = \int_0^{\dot{\epsilon}_{ij}} \tau_{ij} d\dot{\epsilon}_{ij} \tag{2.32}$$

- 21 -

The question of how C_1^* and $(\Delta T_1)_{css}$ are related, is a natural one. Before obtaining an equation relating C_1^* to $(\Delta T_1)_{css}$, however, the conservation integral (2.2) will be used to derive a generalized $\underline{vector}$ integral $\underline{C}^*$.

In specializing (2.2) to steady-state we note that now stress is a function of the strain rate, and that stress increments are zero. Thus, $\Delta W = \tau : \Delta \underline{e}$. Also we may write:

$$\int_{V_t} [\nabla_t \Delta W - (\nabla_t \tau) : \Delta \underline{e}] dV = \int_{V_t} \tau : \nabla_t \Delta \underline{e} \, dV$$

Thus, at steady-state, we may write (2.2) as:

$$\underline{0} = \int_{V_t} [\tau : (\nabla_t \Delta \underline{e}) - \nabla_t \cdot (\tau \cdot \Delta \underline{e}) - \rho_t (\underline{f} - \underline{a}) \cdot \Delta \underline{e}] dV$$

$$+ \int_{S_t} [\underline{n}_t \cdot \tau - \underline{\bar{t}}] \cdot \Delta \underline{e} \, dS + \int_{S_e} \underline{n}_t \cdot \tau \cdot (\Delta \underline{e} - \Delta \underline{\bar{e}}) dS$$

or equivalently, in rate form,

$$\underline{0} = \int_{V_t} [\tau : (\nabla_t \dot{\underline{e}}) - \nabla_t \cdot (\tau \cdot \dot{\underline{e}}) - \rho_t (\underline{f} - \underline{a}) \cdot \dot{\underline{e}}] dV \tag{2.33}$$

$$+ \int_{S_t} [\underline{n}_t \cdot \tau - \underline{\bar{t}}] \cdot \dot{\underline{e}} \, dS + \int_{S_e} \underline{n}_t \cdot \tau \cdot (\dot{\underline{e}} - \dot{\underline{\bar{e}}}) dS$$

Using the symmetry of τ we note that:

$$\tau : \nabla_t \dot{\underline{e}} = \tau : \nabla_t \left[\frac{1}{2} (\dot{\underline{e}} + \dot{\underline{e}}^T) \right] = \tau : \nabla_t \dot{\underline{\varepsilon}} \tag{2.34}$$

As a result of the incompressibility condition ($\dot{\varepsilon}_{ii} = 0$) we have

$$\tau : \nabla_t \dot{\underline{\varepsilon}} = \tau' : \nabla_t \dot{\underline{\varepsilon}} \tag{2.35}$$

and $\quad W^* = \int_0^{\dot{\varepsilon}_{ij}} \tau'_{ij} d\dot{\varepsilon}_{ij} \tag{2.36}$

which leads to

$$\frac{\partial W^*}{\partial \dot{\epsilon}_{ij}} = \tau'_{ij} \tag{2.37}$$

Combining the results of the above manipulations we have:

$$\nabla_t W^* \equiv \frac{\partial W^*}{\partial y_i} = \frac{\partial W^*}{\partial \dot{\epsilon}_{mn}} \frac{\partial \dot{\epsilon}_{mn}}{\partial y_i} = \underline{\tau}' : \nabla_t \dot{\underline{\epsilon}} = \underline{\tau} : \nabla_t \dot{\underline{\theta}} \tag{2.38}$$

Using (2.38) and the divergence theorem while applying (2.33) to $V_t - V_\epsilon$, we define the vector quantity $(\underline{C}^*)^\epsilon$:

$$\int_{\Gamma_{234}} [\underline{n}_t W^* - \underline{n}_t \cdot \underline{\tau} \cdot \dot{\underline{e}}]dS - \int_{V_t - V_\epsilon} \rho_t (\underline{f} - a) \cdot \dot{\underline{e}} dV \tag{2.39}$$

$$+ \int_{\Gamma_{12}} \underline{n}_t W^* dS + \int_{\Gamma_{45}} \underline{n}_t W^* dS - \int_{S_t} \overline{\underline{t}} \cdot \dot{\underline{e}} dS - \int_{S_e} \underline{n}_t \cdot \underline{\tau} \cdot \overline{\dot{\underline{e}}} dS$$

$$- \int_{\Gamma_\epsilon} [\underline{n}_t W^* - \underline{n}_t \cdot \underline{\tau} \cdot \dot{\underline{e}}]dS \equiv (\underline{C}^*)^\epsilon$$

If we define the limit of $(\underline{C}^*)^\epsilon$ as $\epsilon \to 0$ to be $\underline{C}^*$, we have a quantity which characterizes the crack-tip field and is independent of the selection of Γ_{234}. Restricting our attention to problems involving symmetric deformations about the x_1 axis and cracks oriented along the x_1 axis, with traction-free crack faces, no body forces and negligible inertia effects, we find that

$$C_1^* = \underset{\epsilon \to 0}{Lt} \int_{\Gamma_\epsilon} [n_1 W^* - n_j \tau_{j1} \dot{e}_{11}]dS = (C_1^*)^c \tag{2.40}$$

$$= \int_{\Gamma_{234}} [n_1 W^* - n_j \tau_{j1} \dot{e}_{11}]dS$$

In computing W^* it is convenient to invert (2.1), substitute the result into (2.36) and use the following identity to complete the integration:

$$\frac{d(\dot{\epsilon}_{eq})^{\frac{1+n}{n}}}{d\dot{\epsilon}_{ij}} = \frac{2}{3}(\frac{1+n}{n})(\dot{\epsilon}_{eq})^{\frac{1-n}{n}} \dot{\epsilon}_{ij} \tag{2.41}$$

- 23 -

The result of this manipulation is:

$$W^* = \frac{n}{1+n} (\gamma)^{\frac{1}{n}} (\dot{\epsilon}_{eq})^{\frac{1+n}{n}} \tag{2.42}$$

or $$W^* = \frac{n}{1+n} \gamma (\sigma_{eq})^{1+n} \tag{2.43}$$

Relationship of $(\dot{T}_1)_{css}$ and C_1^* for Steady-State Creep

Now we will relate C_1^* of (2.40) to the steady-state value of $(\Delta T_1)_c$.
First we rewrite (2.30) in rate form as:

$$(\dot{T}_1)_{css} = \underset{\epsilon \to 0}{Lt} \int_{\Gamma_\epsilon} [n_1 \tau_{ij} \dot{e}_{ij} - n_j \tau_{j1} \dot{e}_{i1}] dS \tag{2.44}$$

$$\equiv \int_{\Gamma_{234}} [n_1 \tau_{ij} \dot{e}_{ij} - n_j \tau_{j1} \dot{e}_{i1}] dS - \int_{V_t} \frac{\partial \tau_{i1}}{\partial y_1} \dot{e}_{ij} dV$$

Using the notation $\dot{W} = \tau_{ij} \dot{e}_{ij}$ we have

$$(\dot{T}_1)_{css} = \int_{\Gamma_{234}} (n_1 \dot{W} - n_j \tau_{j1} \dot{e}_{i1}) dS \tag{2.45}$$

$$- \int_{V_t} \frac{\partial \tau_{i1}}{\partial y_1} \dot{e}_{ij} dV$$

Noting that:

$$\dot{W} = \tau_{ij} \dot{e}_{ij} = \tau_{ij} \frac{1}{2} (\dot{e}_{ij} + \dot{e}_{ji}) = \tau_{ij} \dot{\epsilon}_{ij} \tag{2.46}$$

it is seen that $\dot{W}$ is the rate of stress-working density, while W* is just a
mathematical potential for τ_{ij}'. As a result of incompressibility we can write[1]

$$\dot{W} = \sigma_{eq} \dot{\epsilon}_{eq} = \gamma (\sigma_{eq})^{1+n} = (\frac{1}{\gamma})^{\frac{1}{n}} (\dot{\epsilon}_{eq})^{\frac{1+n}{n}} \tag{2.47}$$

as contrasted to W* of (2.42) and (2.43). Comparing the left equalities of

---

[1]This result is only valid for steady-state creep and is obtained through the
substitution of the steady-state specialization of (2.1) into (2.46).

(2.40) and (2.44), it is seen that $(\dot{T}_1)_{css}$ and C_1^* are related by:

$$(\dot{T}_1)_{css} = C_1^* + \lim_{\epsilon \to 0} \int_{\Gamma_\epsilon} n_1 (\dot{W} - W) dS \qquad (2.48a)$$

$$= C_1^* + \frac{\gamma}{n+1} \lim_{\epsilon \to 0} \int_{\Gamma_\epsilon} n_1 (\dot{\sigma}_{eq})^{n+1} dS \qquad (2.48b)$$

Appendix B gives several numerical examples of relation (2.48) for two rather extreme values of n.

It is now clear that $\underline{C}^*$ and $(\Delta\underline{T})_c$ are not equivalent quantities under any condition despite their being derivable from the same conservation law[1]. The quantity $(\Delta\underline{T})_c$ follows more directly from the conservation law and is the more general quantity not only in that it is applicable to nonsteady as well as steady-state creep but also in that it is applicable to constitutive laws which are more general than (2.1). The quantity $\underline{C}^*$ relies on the special property of (2.1) which allows the existence of a potential W^* for the stresses (τ'). Furthermore, since W^* does not have any physical meaning, whereas $\dot{W}$ has the meaning of stress-working density, it is understandable that $(\Delta\underline{T})_c$ has an energy interpretation whereas $\underline{C}^*$ does not. It is for this reason that it seems more appropriate to refer to experimental measurements of $-\frac{dE}{da}$ as measurements of $(\dot{T}_1)_c$ as opposed to measurements of C_1^* or $\dot{J}_1$.

The HRR Field

We now give the HRR field in terms of $(\Delta T_1)_c$. Whereas similar relations have been written in terms of C_1^* for steady-state creep [36], the relations in terms of $(\Delta T_1)_c$ will be valid for nonsteady creep as well as steady-state creep. The HRR field as given in [37] but modified for creep by replacing ϵ_{ij} and u_i by $\dot{\epsilon}_{ij}$ and $\dot{u}_i$ respectively, is:

---

[1] Note that these equations are derived on the assumption that $\dot{\tau}_{ij} \equiv 0$ (i.e., creep steady-state). Therefore, in order to have a well defined creep constitutive law we must have $\gamma \neq 0$ and n finite.

$$[\tau_{ij}, \sigma_{eq}] = K_\sigma r^{\frac{-1}{n+1}} [\tilde{\sigma}_{ij}(\theta), \tilde{\sigma}_{eq}(\theta)] \qquad (2.49a)$$

$$\dot{\varepsilon}_{ij} = \gamma K_\varepsilon r^{\frac{-n}{n+1}} \tilde{\varepsilon}_{ij}(\theta) \qquad (2.49b)$$

$$\dot{u}_i = \gamma K_\varepsilon r^{\frac{1}{n+1}} \tilde{u}_i(\theta) \qquad (2.49c)$$

where $\tilde{\sigma}_{eq}(\theta)$ has been normalized to have a maximum value of unity and K_σ and K_ε are amplitude factors which are related by

$$K_\varepsilon = (K_\sigma)^n \qquad (2.49d)$$

It can therefore be seen that the asymptotic crack-tip fields are entirely determined when K_σ (or K_ε) is known or specified. Combining (2.49a,b,c) with the first equality of (2.14), using (2.49d) and rearranging, gives:

$$K_\sigma \doteq \left(\frac{(\Delta T_1)_c}{\gamma I^* \Delta t}\right)^{\frac{1}{n+1}} = \left(\frac{(\dot{T}_1)_c}{\gamma I^*}\right)^{\frac{1}{n+1}} \qquad (2.50)$$

where I^* is analogous to I defined by Eq. (24) of [6] except for the factor $n/(n+1)$ multiplying the energy density term. To be explicit,

$$I^* = I + \frac{1}{n+1} \int_{-\pi}^{\pi} [\tilde{\sigma}_{eq}(\theta)]^{n+1} \cos\theta d\theta \qquad (2.51)$$

It is therefore seen that knowing the value of $(\dot{T}_1)_c$ is equivalent to knowing K_σ and thus is sufficient for defining all aspects of the asymptotic crack-tip field during nonsteady creep as well as under steady-state creep conditions.

SECTION III

DERIVATION OF FINITE ELEMENT EQUATIONS

Before stating the variational principle and deriving the finite element equations, it is beneficial to illustrate the constitutive behavior to which the finite element model is addressed.

Elastic/Viscoplastic Constitutive Relations

A rather general rate constitutive law proposed by Perzyna [38], can be written in incremental form as:

$$\Delta\epsilon_{ij} = \frac{1}{2\mu}\Delta\tau'_{ij} + \frac{1-2\nu}{3E}\Delta\tau_{kk}\delta_{ij} + \gamma<\Phi(F)>\frac{\partial f}{\partial\tau_{ij}}\Delta t \qquad (3.1)$$

where μ, E and ν are the elastic shear modulus, Young's modulus and Poisson's ratio, respectively, τ'_{ij} $(=\tau_{ij} - \frac{1}{3}\tau_{kk}\delta_{ij})$ is the deviatoric stress and γ is a viscosity constant of the material. In writing (3.1) it is implied that

$$\Delta\epsilon_{ij} = \Delta\epsilon^e_{ij} + \Delta\epsilon^{vp}_{ij}$$

where $\Delta\epsilon^e_{ij}$ and $\Delta\epsilon^{vp}_{ij}$ are the elastic and viscoplastic strain increments, respectively. The yield function $F(\tau_{ij}, \epsilon^{vp}_k)$ governs the magnitude of the incremental viscoplastic strains through the function $<\Phi(F)>$ where

$$<\Phi(F)> = \begin{cases} 0 & \text{for } F \leq 0 \\ \Phi(F) & \text{for } F > 0 \end{cases} \qquad (3.2)$$

The relative magnitudes for the incremental viscoplastic strain components are seen to depend on the factor $\partial f/\partial \tau_{ij}$.[1] This implies that $\Delta \epsilon_{ij}^{vp}$, when considered as a vector in nine-dimensional stress space, is always directed along the normal to the surface $f(\tau_{ij}, \epsilon_k^{vp})$.

By choosing $F \equiv f = \sigma_{eq} [\sigma_{eq} = (3/2(\tau'_{ij} \tau'_{ij})^{1/2}]$ such that $\partial f/\partial \tau_{ij} = (3/2) (\tau'_{ij}/\sigma_{eq})$, and choosing $\phi(F) = (F)^n$ we find that (3.1) becomes

$$\Delta \epsilon_{ij} = \frac{1}{2\mu} \Delta \tau'_{ij} + \frac{1-2\nu}{3E} \Delta \tau_{kk} \delta_{ij} + (3/2)\gamma(\sigma_{eq})^{n-1} \tau'_{ij} \Delta t \qquad (3.3)$$

This represents the special case of creep behavior which is considered exclusively in this study.[2] It should be understood, however, that the finite element model which is described below is applicable to the more general behavior represented by (3.1).

Derivation of Finite Element Equations

The finite element model is derived from the principle of virtual work

$$\int_V \tau_{ij} \delta \epsilon_{ij} dV - \int_{S_\sigma} \overline{t}_i \delta u_i dS = 0 \qquad (3.4)$$

In the present finite element analysis, we assume only infinitesimal deformations and strains; hence there is no need to differentiate between the deformed and undeformed configurations.

In writing (3.4) it should be noted that τ_{ij} are the stresses existing at time $t + \Delta t$ (where t is the current time), $\overline{t}_i$ are the prescribed tractions on S_σ at $t + \Delta t$, and $\delta u_i [\delta \epsilon_{ij} = (1/2)(\delta u_{i,j} + \delta u_{j,i})]$ are arbitrary compatible virtual displacements.

Following customary procedures we introduce the element displacement shape functions which relate element displacement u_i to element nodal

---

[1] It is common to choose $f \equiv F$ in which case we have what is called an associative law.

[2] While (3.3) is known to deviate from real material behavior (especially for primary creep) it is a widely used constitutive law and therefore has been adopted in the present study.

- 28 -

displacements {q}

$$u_i = \{u\} = [N]\{q\}; \quad \delta u_i = \{\delta u\} = [N]\{\delta q\} \tag{3.5}$$

We again use the customary notation wherein strain (and stress) components are placed in one-dimensional arrays

$$\{\epsilon\} = [B]\{q\}; \quad \{\delta \epsilon\} = [B]\{\delta q\} \tag{3.6}$$

Substituting (3.5) and (3.6) into (3.4) and applying conventional procedures for assembling element matrices into global matrices we have

$$\left\{ \sum_{ele} \left[\int_{V_e} \{\tau\}^T [B] dV \right.\right.$$

$$\left.\left. - \int_{S_{\sigma_e}} \{\bar{t}\}^T [N] dS \right] \right\} \left\{ \sum_{ele} \{\delta q\} \right\} \equiv \{F\}^T \{\delta Q\} = 0$$

Since {δq} are arbitrary virtual nodal displacements, it follows that

$$\left\{ \sum_{ele} \left[\int_{V_e} \{\tau\}^T [B] dV - \int_{S_{\sigma_e}} \{\bar{t}\}^T [N] dS \right] \right\} \equiv \{F\}^T = \{0\}^T \tag{3.7}$$

We now express the stresses {τ} at $t + \Delta t$ in terms of the current stresses, $\{\tau\}_I$, and the incremental stresses corresponding to the time increment Δt:

$$\{\tau\} \equiv \{\tau\}_{I+1} = \{\tau\}_I + \{\Delta \tau\}_{I+1} \tag{3.8}$$

In (3.8) and in the following, the I and I+1 subscripts designate the incremental solution with which the quantity is associated. Application of the incremental elastic constitutive law results in

$$\{\tau\}_{I+1} = \{\tau\}_I + [E]\{\Delta \epsilon_{el}\}_{I+1} \tag{3.9}$$

$$= \{\tau\}_I + [E][\{\Delta \epsilon\}_{I+1} - \{\Delta \epsilon_{vp}\}_{I+1}]$$

where $\{\Delta \epsilon_{vp}\}_{I+1}$ are the incremental viscoplastic strains and [E] is the matrix

of elastic constants. Substituting (3.9) into (3.7), taking the transpose, and placing the known terms on the right hand side we have the final form of the finite element equations:

$$[K]\{\Delta Q\}_{I+1} = \{T\}_{I+1} + \{S_{vp}\}_{I+1} - \{R\}_I \tag{3.10}$$

where

$$[K] = \sum_{ele} \int_{V_e} [B]^T [E][B] dV \tag{3.11}$$

$$\{T\}_{I+1} = \sum_{ele} \int_{S_{\sigma_e}} [N]^T \{\bar{t}\}_{I+1} dS \tag{3.12}$$

$$\{S_{vp}\}_{I+1} = \sum_{ele} \int_{V_e} [B]^T [E]\{\Delta \epsilon_{vp}\}_{I+1} dV \tag{3.13}$$

$$\{R\}_I = \sum_{ele} \int_{V_e} [B]^T \{\tau\}_I dV \tag{3.14}$$

The above volume integrals are evaluated in the current work by 2x2 Gauss quadrature. The array {T} is input directly in terms of node point forces.

Solution Procedures

It should be noted that [K] of (3.10) is just the elastic stiffness and therefore only needs to be formed and decomposed[1] once. This results in significant savings in the number of computations per time step as compared to methods using stiffness matrices which must be reformed at each step (i.e., tangent stiffness methods). It should also be noted that the term $\{S_{vp}\}_{I+1}$ is computed from incremental viscoplastic strains $\{\Delta \epsilon_{vp}\}_{I+1}$ which are esti-mated using $\{\tau\}_I$ and the material constitutive law (3.1). Only for the

---

[1]The equations (3.10) are solved in the current work by the decomposition $[K] = [L][D][L]^T$ where [D] is a diagonal matrix (the only nonzero entries are those on its diagonal) and [L] is a lower triangular matrix (the only nonzero entries are those below its diagonal); see for example [39].

special situation when the stresses do not change with time will this estimate be exact. Having obtained the incremental nodal displacements $\{\Delta Q\}_{I+1}$ by solving (3.10), one can easily find the total incremental strains $\{\Delta\epsilon\}_{I+1}$ via the incremental analogue of (3.6). We now describe two procedures for obtaining $\{\tau\}_{I+1}$.

The first and simpler method to obtain $\{\tau\}_{I+1}$ is to substitute the estimated $\{\Delta\epsilon_{vp}\}_{I+1}$ used in solving for $\{\Delta Q\}_{I+1}$ into (3.9). If one does this, then it happens that

$$\{R\}_{I+1} = \{T\}_{I+1} \tag{3.15}$$

and therefore (3.10) becomes for the next step[1]

$$[K]\{\Delta Q\}_{I+2} = \{T\}_{I+2} + \{S_{vp}\}_{I+2} - \{T\}_{I+1} \tag{3.16}$$

$$= \{\Delta T\}_{I+2} + \{S_{vp}\}_{I+2}$$

This method was compared to the following method and was found to require smaller time steps to achieve similar results.

Rather than using the estimated values of $\{\Delta\epsilon_{vp}\}_{I+1}$ and (3.19) to determine $\{\tau\}_{I+1}$, the constitutive relation (2.1) is integrated over the current time step at each Gaussian quadrature point with the condition that total strain $\{\epsilon\}$ varies linearly with respect to time from $\{\epsilon\}_I$ to $\{\epsilon\}_{I+1}$. (The present study uses an Eulerian scheme with each time step being divided into five subincrements.) The result of this procedure is better adherence to the postulated constitutive law at the expense of introducing a somewhat unequilibrated stress state. The amount of disequilibrium depends on the accuracy of the original estimate for the incremental viscoplastic strains and thus on the time step size.

At this point one has two alternatives. The first is to use the

---

[1]This procedure results in the current model reducing to that of Zienkiewicz and Cormeau [40].

viscoplastic strain increments obtained through the time integration procedure as an improved estimate and to re-solve (3.10) for the current time step. This procedure would, after several iterations, result in a stress state which is equilibrated to within some small user specified tolerance. With this type of procedure the time steps could be as large as those used with tangent stiffness methods. Further, it is reasonable to expect the solution to be at least as accurate as if a tangent stiffness method were used.[1]

The second alternative is to go immediately to the next time step with the understanding that the term $\{R\}_I$ in (3.10) results in the disequilibrium from the Ith step being corrected in the I+1 step. This feature is the result of the virtual work statement (3.4) being written in terms of total stress and tractions rather than incremental quantities. Owing to this corrective nature and to the diminishing returns one obtains from additional iterations, the second alternative is used in the present study.

Regulation of Time Steps

The creep calculations use a variable time step size which is automatically regulated by the finite element program based on two criteria. The first criterion is the maximum percent difference between the incremental equivalent estimated creep strain and the incremental equivalent integrated creep strain for all the Gauss points in the mesh:

$$C_1 = \text{Max} \left| \frac{\Delta\bar{\epsilon}_{EST} - \Delta\bar{\epsilon}_{INT}}{\Delta\bar{\epsilon}_{INT}} \right| \tag{3.17}$$

The second criterion is the maximum ratio of incremental equivalent integrated

---

[1]This procedure could actually be more accurate if similar constitutive law integration procedures and equilibrium iterations are not performed with the tangent stiffness procedure. Also, it has been shown [41] that many element types become overly stiff when using the tangent stiffness method for modeling constitutive behavior approaching incompressibility. This problem is not encountered with the current method.

creep strain to the equivalent elastic strain:

$$C_2 = \text{Max}\left[\overline{\Delta\epsilon}_{INT} \frac{E}{\sigma}\right]$$ (3.18)

The user specified, maximum permissible values for C_1 and C_2 are $\overline{C}_1$ and $\overline{C}_2$, respectively. The size of the next step is then obtained from

$$\Delta t_{I+1} = \Delta t_I \cdot \text{Min}\left[\frac{\overline{C}_1}{C_1}, \frac{\overline{C}_2}{C_2}\right]$$ (3.19)

Note that the initial time increment cannot be determined from (3.19) and must be specified by the user so as to satisfy the two step size criteria.

In the present study, the values of $\overline{C}_1$ and $\overline{C}_2$ are 0.2 and 1.0, respectively. With these values, it has been found that the initial time steps are controlled by $\overline{C}_1$ while later time steps are controlled by $\overline{C}_2$. The values of C_1 and C_2 are strongly affected by the mesh refinement since a finer mesh results in Gauss points being closer to the crack-tip and therefore having larger stresses and strain rates. To determine the sensitivity of the solution to the selection of $\overline{C}_1$ and $\overline{C}_2$, a compact specimen was analyzed with the above criteria and also with $\overline{C}_1$ and $\overline{C}_2$ being halved (i.e., $\overline{C}_1 = 0.1$ and $\overline{C}_2 = 0.5$). It was found that the load point displacement differed by less than 0.5% for all time and that the steady-state solutions were essentially identical. It therefore appears these values of $\overline{C}_1$ and $\overline{C}_2$ are small enough to ensure that the solutions to be discussed do not depend on these step size criteria.

SECTION IV

ELEMENTS FOR SINGULAR CRACK-TIP BEHAVIOR

This section describes and compares several two-dimensional crack-tip singularity elements. Perhaps the primary motivation for introducing singular crack-tip elements into finite element models is the significant savings in computational expense. It is shown in Section V, for example, that 57 element model with elastic, $r^{-1/2}$, singular elements results in a more accurate solution than a non-singular 102 element model. The savings in CP time in this case is greater than 50%. Generally, one must consider that some additional effort is required to develop and implement a special crack-tip element and that this tends to offset the savings in CP time. It has been discovered, however, that the very commonly used, eight-noded, isoparametric element can be made to produce an $r^{-1/2}$ strain singularity by merely shifting mid-side node locations via the node definition input data [42,43]. Therefore, a very convenient means for modeling linear elastic crack-tip behavior exists. It has also been shown [44] that a 1/r type strain singularity can be obtained with this element type thus providing a suitable element for non-hardening plasticity problems. For more general singularity behavior, such as the $r^{-n/(n+1)}$ strain singularity associated with the HRR crack-tip field of power-law plasticity or creep, one must resort to sepcially formulated elements.

In the following sections, we consider special elements for linear

elastic problem ($r^{-1/2}$ strain singularity) as well as special elements for problems involving the HRR, $r^{-n/(n+1)}$, strain singularity. In discussing these elements, an attempt is made to point out their advantages and disadvantages.

Elements for Linear Elastic Materials

Although many special elements have been used for linear elastic fracture analysis (see Atluri [45] for review), we consider here only the eight-noded isoparametric element. There are two basic forms in which the eight-noded isoparametric element can be used as a linear elastic crack-tip element. In the first form, the two midside nodes adjacent to the corner node located at the crack-tip are shifted toward the corner node so that they occupy the quarter-point of their respective sides. This form is illustrated in Fig. 4.1 by the Type A crack-tip mesh. The second form in which the element can be used is illustrated in Fig. 4.1 by the Type B crack-tip mesh. In this form, the eight-noded element is degenerated to a triangular element by defining two corner nodes and their midside node to be the same node which is located at the crack tip. Then the two midside nodes adjacent to the crack-tip corner node are shifted to their quarter-points. It is important that only one node be used at the crack-tip, as opposed to three superposed nodes, since the latter case has been shown [44] to result in the 1/r type strain singularity.

Barsoun [43,44] notes that numerical experimentation shows the degenerate triangular form yields more accurate results than the nondegenerate element. He goes on to recommend that the four-sided configuration be abandoned based on the premise that the $r^{-1/2}$ singularity exists only along the edges of the element and also that the strain energy for this element becomes unbounded if exact integration is used [44]. Ying [46], on the other hand, concludes that the $r^{-1/2}$ singularity does exist within the four-sided element as well as along its edges and that the strain energy for the element is bounded (and thus

Mesh type A
Square 8-node isoparametric
elements

Mesh type B
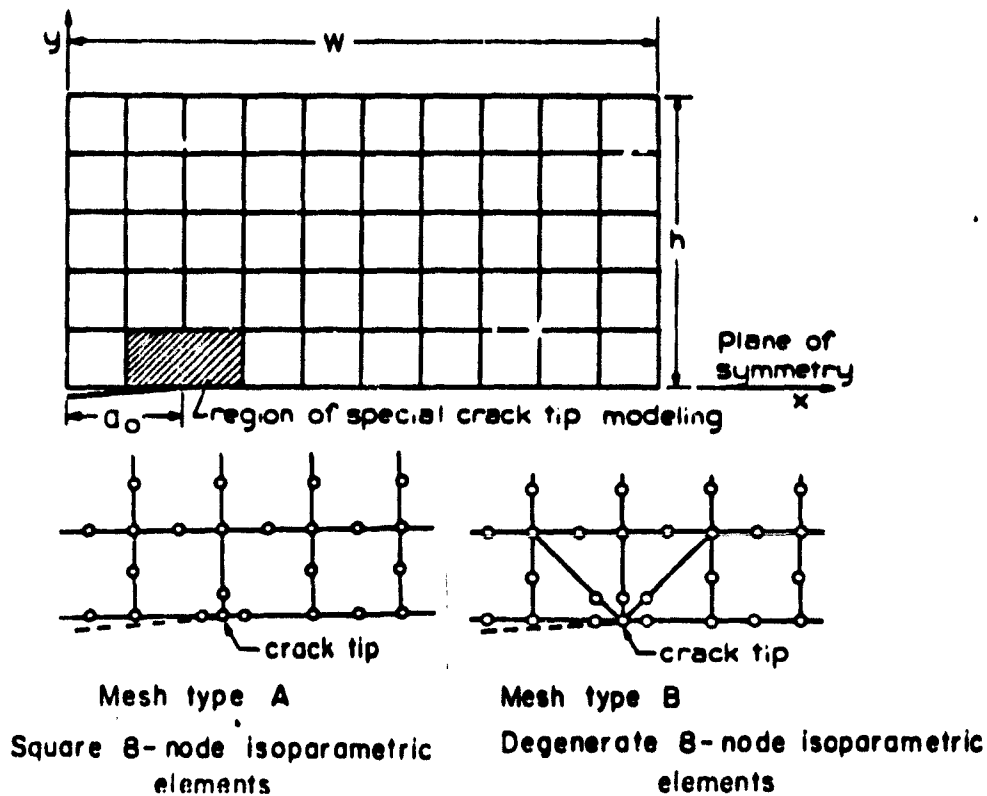Degenerate 8-node isoparametric
elements

Fig. 4.1 Several crack-tip mesh configurations

the element stiffness is well defined).

Apart from the above considerations, there are two aspects of the degenerate Type B element which inherently make it preferable to the nondegenerate element. The first is that the process of collapsing one side of the element to coincide with the crack-tip results in the element local coordinates being transformed into a form of polar coordinates. Since the element's shape functions are defined in the element local coordinates it is to be expected that angular bias will be much less apparent for this element type. The second feature of the degenerate triangular element which makes i preferable is that it is geometrically better suited for creating crack-tip finite element meshes of arbitrary refinement. Since the angular dependence of the near tip solution is significant, this flexibility for increasing the mesh refinement in the angular direction is important. Combining these two aspects with the numerical evidence cited by Barsoum, it seems the triangular, degenerate element is the better element for modeling the elastic crack-tip singularity. For this reason, all quarter-point element calculations in the present study use the degenerate triangular form. In particular, the mesh configuration Type B of Fig. 4.1 has been used exclusively.

Elements for Materials with HRR Crack-Tip Fields

In the previous section, we discussed crack-tip elements for linear elastic material behavior. It has been seen that the standard eight-noded isoparametric element can be made to have the $r^{-1/2}$ strain singularity and thus is useful for analysis of cracks in linear elastic materials. It can be shown (see for example, Atluri [45]) that this is the only singularity which this eight-noded element can exhibit. However, it can also be shown that higher order elements of the isoparametric family can result in singularities of the type $r^{-n/(n+1)}$, provided n is an integer. If we denote the order of the isoparametric

interpolation as m, then singularities of the type $r^{(1-t)/t}$ can be obtained for t an integer such that $t \leq m$ [45]. In terms of the HRR power law exponent n, this means we can have singularities of the type $r^{-n/(n+1)}$ where n in an integer such that $\leq m-1$.

Based on the above discussion, it can be seen that it is possible to employ isoparametric elements as HRR crack-tip elements provided one is satisfied with integer values of the power law exponent, n. By choosing the highest value of n which one is interested in modeling, one can then program the n+1 order isoparametric element. The problem with this approach is that values of n for common materials can be as high as 20. This implies that one would need to program an isoparametric element of order 21. While this is perhaps within reason, it will be shown that nonisoparametric elements can be derived which are more readily implemented.

Two Crack-Tip Elements from the Literature

In this discussion of special elements we limit consideration to two-dimensional, triangular elements with straight sides. The elements are derived in terms of the triangular polar coordinates (ρ, σ) illustrated in Fig. 4.2 and which are related to the global cartesian coordinates (x_i) by

$$x_i = x_i^1 + \rho(x_i^2 - x_i^1) + \frac{1}{2}(\sigma + 1)(x_i^3 - x_i^2)) \tag{4.1}$$

In (4.1), the superscripts denote the node number. The crack-tip is assumed to be located at node 1 (i.e., at $\rho=0$). The geometric mapping of (4.1) is similar to circular polar coordinates in that the transformation cannot be inverted at $\rho=0$.

We now consider several choices for the assumed displacement fields within the triangular region. The first choice is

$$u_i(\rho, \sigma) = u_i^1 + \rho^\lambda(u_i^2 - u_i^1) + \frac{1}{2}(\sigma + 1)(u_i^3 - u_i^2)) \tag{4.2}$$
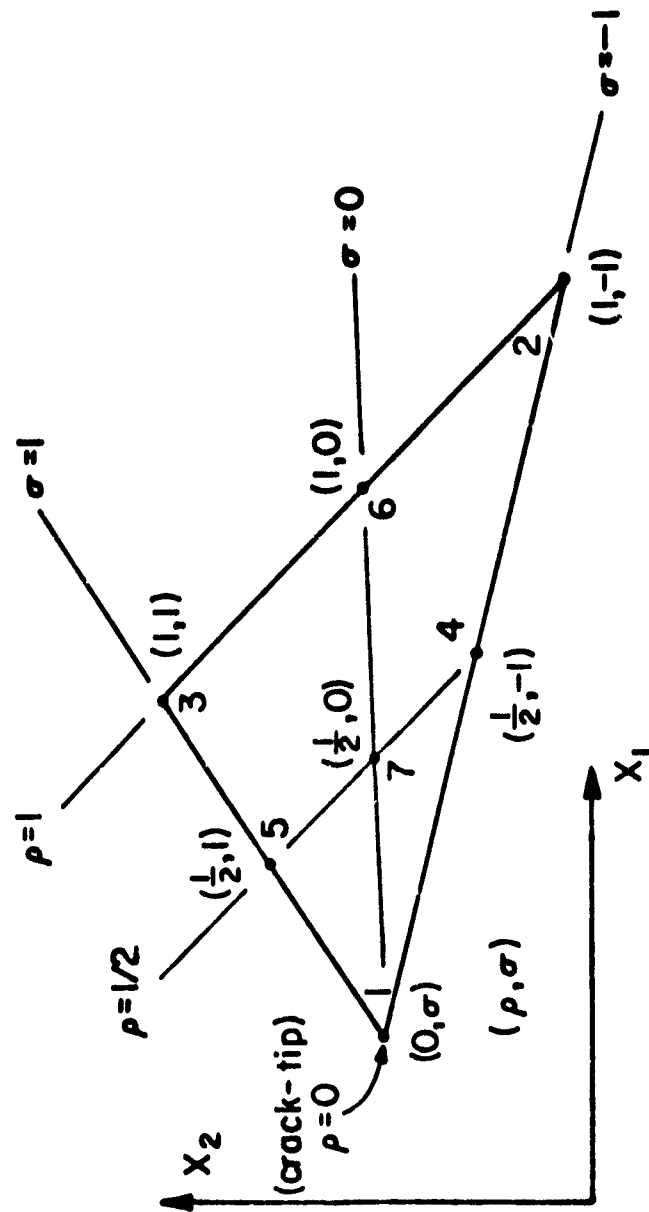
Fig. 4.2 Coordinate systems and node numbering conventions for the conforming, seven-noded arbitrary strain singularity element.

It can be seen that (4.2) is similar in form to (4.1) except that ρ is replaced by ρ^λ ($0 < \lambda < 1$) so as to induce a singularity in the displacement derivatives. The three-noded element resulting from (4.1) and (4.2) is of the type proposed by Tracey and Cook [47]. Inspection of (4.2) reveals that this element permits rigid body translation but does not permit rigid body rotations or constant strain modes. While problems exist for which this element provides reasonable results, the lack of rigid body and constant strain modes make this an undesirable element for general anlaysis.

We now consider a straightforward procedure which allows an alternative to (4.2) to be written which (i) provides all the rigid body modes as well as all the constant strain modes, (ii) results in the desired r^λ displacement behavior and (iii) results in compatible displacement fields with adjacent elements. First note that we can be assured our assumed displacement field contains all rigid body and constant strain modes provided it can accomodate the following general displacement field

$$u_1 = a_1 + b_1 x_1 + c_1 x_2 \tag{4.3a}$$

$$u_2 = a_2 + b_2 x_1 + c_2 x_2 \tag{4.3b}$$

where a_i, b_i and c_i are constants. Clearly, a_1 and a_2 provide for rigid translation modes, while b_1 and c_2 provide for constant strains, ϵ_{11} and ϵ_{22}, respectively. The constants c_1 and b_2 provide a rigid rotation if $c_1 = -b_2 \neq 0$ and a constant shear strain, ϵ_{12}, if $c_1 = b_2 \neq 0$. If we substitute (4.1) into (4.3) and regroup terms we have the result

$$u_1 = a_1^* + b_1^* \rho + c_1^* \rho \sigma \tag{4.4a}$$

$$u_2 = a_2^* + b_2^* \rho + c_2^* \rho \sigma \tag{4.4b}$$

Starting from (4.4), we can now proceed to add terms as desired with the only condition being that we maintain compatible displacements with neighboring singular and nonsingular elements

We now consider a general approach for establishing displacement shape functions for triangular crack-tip elements. Since both displacement components will follow the same form, we drop the subscript for simplicity. We now write

$$u(\rho,\sigma) = \frac{1}{2}(1 + \sigma)f_3(\rho) + \frac{1}{2}(1 - \sigma)f_2(\rho) \qquad (4.5)$$

with

$$f_2(\rho) = a_2 + b_2\rho + c_2\rho^\lambda \qquad (4.6a)$$

$$f_3(\rho) = a_3 + b_3\rho + c_3\rho^\lambda \qquad (4.6b)$$

Inspection of (4.5) shows that on the element side 1-2, $u(\rho,-1) = f_2(\rho)$ and on side 1-3, $u(\rho,1) = f_3(\rho)$. It can also be seen that $u(1,\sigma)$ is linear on side 2-3. Since f_2 and f_3 each have three unknowns, it follows that element sides 1-2 and 1-3 must have three nodes. This means two new nodes must be created. Since the geometric properties of the element do not depend on the locations of these nodes their positions along the edges of the element are arbitrary. In the following, however, we choose to place these nodes at the midsides. These new nodes correspond to positions 4 and 5 in Fig. 4.2. Denoting the nodal displacements by u^j, $j=1,5$, we now use the following conditions to determine the six unknowns in (4.6a) and (4.6b)

$$u(0,\sigma) = u^1; \quad u(1,-1) = u^2; \quad u(1,1) = u^3 \qquad (4.7)$$

$$u(\tfrac{1}{2},-1) = u^4; \quad u(\tfrac{1}{2},1) = u^5$$

The result is

$$a_2 = a_3 = u^1; \quad b_2 = u^2 - u^1 - c_2; \quad b_3 = u^3 - u^1 - c_3 \qquad (4.8)$$

$$c_2 = \frac{2u^4 - u^2 - u^1}{2^{1-\lambda} - 1}; \quad c_3 = \frac{2u^5 - u^3 - u^1}{2^{1-\lambda} - 1}$$

Substituting (4.8) and (4.6) into (4.5) and defining the functions multiplying

u^i as N_i^5 we have

$$u(\rho,\sigma) = \sum_{i=1}^{5} N_i^5 u^i \qquad (4.9)$$

where

$$N_1^5 = 1 - \rho - \frac{1}{\beta}(\rho^\lambda - \rho); \quad N_2^5 = \phi_1^5 \psi_1^5;$$

$$N_3^5 = \phi_2^5 \psi_2^5; \quad N_4^5 = \phi_1^5 \psi_2^5; \quad N_5^5 = \phi_2^5 \psi_2^5$$

with

$$\beta = 2^{1-\lambda} - 1$$

$$\phi_1^5 = \frac{1}{2}(1 - \sigma) \qquad \phi_2^5 = \frac{1}{2}(1 + \sigma)$$

$$\psi_1^5 = \rho - \frac{1}{\beta}(\rho^\lambda - \rho) \qquad \psi_2^5 = \frac{2}{\beta}(\rho^\lambda - \rho)$$

By examination, it can be seen that (4.9) has terms similar to those of (4.4) and thus can represent all the rigid body and constant strain modes. From the form of (4.5,6,8) it can be seen that the element must be compatible with neighboring elements. Therefore, we have an element whihc satisfies all the requirements which we originally stipulated. If the σ in Fig. 4.2 and in (4.9) is replaced by $2\sigma' - 1$ we recover the form of the equations suggested by Stern [48].

As a result of the appearance of ρ^λ in the shape functions for this element, the integration involved in evaluating the stiffness matrix (particularly the integration with respect to ρ) is not suited to Gauss quadrature. In [48], Stern derives a special integration rule, which when combined with standard Gauss quadrature for integration with respect to σ, results in exact stiffness integrations. Unfortunately, the expression (28) in [48] which specifies the relative radial location of the quadrature points is apparently in error. The corrected expression is as follows:

$$x_1 = \xi x_2 = \left[\frac{1 + \lambda - 2\lambda x_2^{\lambda-1}}{2\lambda - \lambda(1 + \lambda)x_2^{\lambda-1}}\right]^{\frac{1}{\lambda-1}} \tag{4.10}$$

where x_1 and x_2 denote the values of ρ at which the sampling points are located. The corresponding weights are then given by

$$x_1 = \frac{\frac{1}{2}x_2^{\lambda-1} - \frac{1}{\lambda+1}}{x_1 x_2^{\lambda-1} - x_1^{\lambda}} \tag{4.11}$$

$$w_2 = \frac{\frac{1}{2}x_2^{\lambda-1} - \frac{1}{\lambda+1}}{x_2 x_1^{\lambda-1} - x_2^{\lambda}} \tag{4.12}$$

This quadrature rule integrates terms of the type ρ, ρ^{λ} and $\rho^{2\lambda-1}$ exactly. Since the rule has four parameters (x_1, x_2, w_1, w_2) and is only required to integrate three types of terms, the locations of the quadrature points are not uniquely defined. Selection of x_2 according to the following cirterion results in both the numerator and denominator of the bracketed term of (4.10) being positive and thus results in a valid quadrature rule.

$$\left[\frac{\lambda(1+\lambda)}{2\lambda}\right]^{\frac{1}{1-\lambda}} < x_2 \leq 1 \tag{4.13}$$

Stern [48] presents a family of elements which are developed so as to be compatible with surrounding nonsingular polynomial based elements of arbitrary order. While it should be possible to verify that each member of this family does indeed satisfy the requirements which were discussed in deriving the above element, this procedure provides little insight to the method for deriving such elements. In the next section, we generalize the procedure used in arriving at (4.9) to derive an element which is compatible with quadratic elements (e.g., eight-noded isoparametric elements).

Derivation of a New Crack-Tip Element

In this section we generalize the procedure used in the previous section

to derive a crack-tip element which (i) contains all rigid body and constant strain modes, (ii) results in compatible displacement fields with neighboring singular and nonsingular elements and (iii) results in an arbitrary strain singularity at the crack-tip fo the type $r^{\lambda-1}$ $(0<\lambda<1)$.

We start in the same manner as before by writing the displacement field in the form

$$u(\rho,\sigma) = (1-\sigma^2)f_1(\rho) + \frac{1}{2}\sigma(\sigma-1)f_2(\rho) + \frac{1}{2}\sigma(\sigma+1)f_3(\rho) \qquad (4.14)$$

where

$$f_i(\rho) = a_i + b_i\rho + c_i\rho^\lambda \qquad (4.15)$$

Noting that the form of (4.15) requires three displacements being specified along each of three radial line segments ($\sigma=-1$, $\sigma=0$, $\sigma=1$) we introduce node points at locations 4 through 7 as illustrated in Fig. 4.2. At this point it is seen that this procedure will result in an interior node. It will be shown later that this node can be eliminated in a number of ways.

Denoting the nodal displacements by u^j, $j=1,7$ we now use the following conditions to determine the nine unknowns in (4.14,15):

$$u(0,\sigma) = u^1; \quad u(1,-1) = u^2; \quad u(1,1) = u^3 \qquad (4.16)$$

$$u(\tfrac{1}{2},-1) = u^4; \quad u(\tfrac{1}{2},1) = u^5; \quad u(1,0) = u^6$$

$$u(\tfrac{1}{2},0) = u^7$$

The result is

$$a_1 = a_2 = a_3 = u^1 \qquad (4.17)$$

$$b_1 = u^6 - u^1 - c_1; \quad b_2 = u^2 - u^1 - c_2; \quad b_3 = u^3 - u^1 - c_3$$

$$c_1 = \frac{1}{\beta}(2u^7 - u^6 - u^1); \quad c_2 = \frac{1}{\beta}(2u^4 - u^2 - u^1)$$

$$c_3 = \frac{1}{\beta}(2u^5 - u^3 - u^1)$$

with $\quad \beta = 2^{1-\lambda} - 1$

Substituting (4.17) and (4.15) into (4.14) and defining the functions multiplying u^i as N_i^7 we have

$$u(\rho,\sigma) = \sum_{i=1}^{7} N_i^7 u^i \tag{4.18}$$

where

$$N_1^7 = 1 - \rho - \frac{1}{\beta}(\rho^\lambda - \rho)$$

$$N_2^7 = \phi_2^7 \psi_2^7; \quad N_3^7 = \phi_3^7 \psi_2^7; \quad N_4^7 = \phi_2^7 \psi_1^7$$

$$N_5^7 = \phi_3^7 \psi_1^7; \quad N_6^7 = \phi_1^7 \psi_2^7; \quad N_7^7 = \phi_1^7 \psi_1^7$$

with

$$\phi_1^7 = 1 - \sigma^2; \quad \phi_2^7 = \frac{1}{2}\sigma(\sigma - 1); \quad \phi_3^7 = \frac{1}{2}\sigma(\sigma + 1)$$

$$\psi_1^7 = \frac{2}{\beta}(\rho^\lambda - \rho) \qquad \psi_2^7 = \frac{1}{\beta}[(1 + \beta)\rho - \rho^\lambda]$$

Inspection of the derived shape functions verifies that this element satisfies all the requirements which we stipulated at the beginning of the derivation. It was noted that this element has an interior node. While interior nodes are generally avoided so as to reduce the bandwidth of the equations to be solved, it seems that in the case of crack-tip elements the advantage of having additional degrees of freedom in the vicinity of the crack-tip more than compensates for the few additional equations which are involved.

We now consider several alternatives for eliminating the interior node of this element and note that one of these results in the corresponding element of Stern [48]. We start by substituting (4.15) into (4.14); using the condition that $f_1(0) = f_2(0) = f_3(0)$ and regrouping terms we can write

$$u(\rho,\sigma) = [a_1 + b_1\rho + c_1\rho^\lambda] \qquad \text{(con't on next page)} \tag{4.19}$$

$$+ \frac{1}{2}\sigma[(b_3 - b_2)\rho + (c_3 - c_2)\rho^\lambda]$$

$$+ \sigma^2\left[\left(\frac{b_2}{2} + \frac{b_3}{2} - b_1\right)\rho + \left(\frac{c_2}{2} + \frac{c_3}{2} - c_1\right)\rho^\lambda\right]$$

It should be understood that any arbitrary condition relating u^7 to one, several or all of u^1 through u^6 will suffice to remove the interior node (i.e., node 7) from the element relations. However, it seems more natural to eliminate the node by the removal of one of the terms of (4.19). Noting that the first two terms of the first square bracket and the first term of the second square bracket represent the rigid body modes and constant strain modes, we are left with four terms which can possibly be deleted so as to eliminate the interior node.

If we choose to eliminate the term $c_1\rho^\lambda$ by constraining c_1 to be zero we see from (4.17) that this implies $u^7 = \frac{1}{2}(u^6 + u^1)$. This choice would somewhat defeat the objective of having singular displacement derivatives and thus is not advisable. Furthermore, it is inconsistent to retain the higher order terms $\sigma\rho^\lambda$ and $\sigma^2\rho^\lambda$ while not retaining ρ^λ. Note that the term $\sigma\rho^\lambda$ cannot be used to eliminate u^7 since u^7 does not appear in its coefficient (i.e., in either c_2 or c_3). Therefore we are left with the terms $\sigma^2\rho$ and $\sigma^2\rho^\lambda$. Either of these terms can be chosen to eliminate u^7. Stern's element [48] corresponds to the case in which the coefficient of $\sigma^2\rho$ is set identically to zero.

Of the elements discussed above, only the seven-noded element has been implemented in the present study. In Section V, this element is used for elastic analysis as well as for creep analysis. The special quadrature rule proposed by Stern [48] and summarized in (4.10) through (4.13) has been used exclusively in evaluating this element's stiffness.

SECTION V

CREEP CRACK GROWTH COMPUTATIONS

Description of Problems

The creep crack growth analyses which will be presented in this chapter deal with three distinct problems. The following sections introduce each problem by describing the physical aspects such as geometry, loading and material properties as well as by describing why the problem was selected and what is hoped to be gained by its consideration.

All calculations in this chapter assume infinitesimal strains and small deformations. The crack propagation calculations use quarter-point crack-tip elements and a mesh shifting/remeshing procedure.

Problem I: Non-Steady Creep of a Compact Specimen

The compact specimen geometry was chosen for study because of its widespread use in fracture experiments and because numerical solutions for this problem have appeared in the literature thus providing results with which to compare. The dimensions of the specimen as well as the material properties and applied loading (see Fig. 5.1) were chosen to coincide with those used recently by Ehlers and Riedel [33]. The problem is used for a mesh refinement sensitivity study and for exploring various aspects of the $(\dot{T}_1)_c$ and C_1^* contour integrals during both nonsteady and steady-state creep.

Several finite element meshes have been uased in the analysis. All
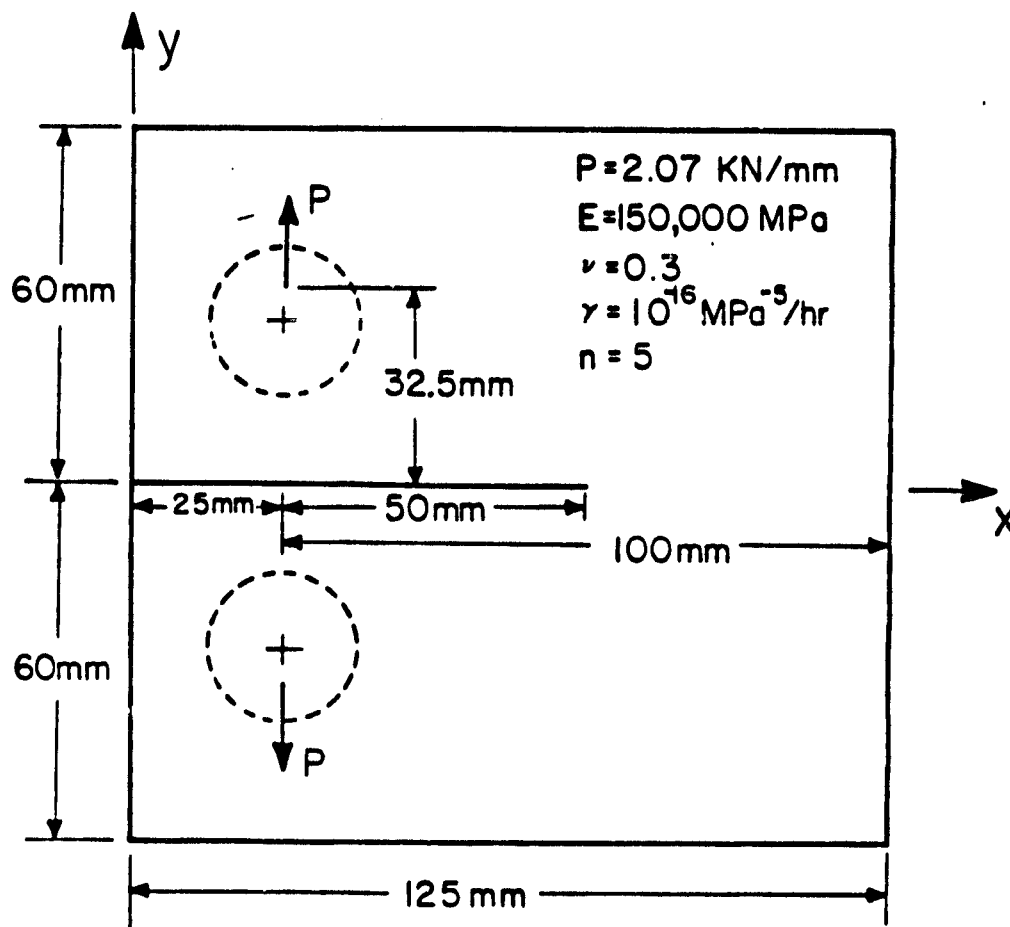
Fig. 5.1 Compact specimen geometry, loading condition, and material properties

of these meshes employ two-dimensional, eight-noded, isoparametric elements. The integrations for these elements are accomplished with 2x2 Gauss quadrature and therefore only elements with straight sides are employed. As seen from the meshes in Fig. 5, 2, the pin-loading hole is not modeled. In all models the horizontal placement of the point load corresponds with the load line of the ASTM standard geometry (x = 25.0 mm). The vertical position is y = 32.5mm. A sensitivity study showed that shifting the load to y = 40 mm has virtually no effect on the pertinent aspects of the solution.

Most of the meshes contain collapsed eight-noded isoparametric elements at the crack-tip as illustrated in Fig. 6.2. In several calculations, the midside nodes of these crack-tip elements are shifted to their quarter-points so as to produce an $r^{-1/2}$ strain singularity at the crack-tip. Also, several calculations are performed with a special conforming seven-noded, triangular element which imposes the HRR, $r^{-n/(n+1)}$, type strain singularity. Table 5.1 identifies the meshes for which calculations are made and also gives the load point displacement and J_1 for the elastic solutions. These J_1 values are compared to those based on the expression for K_I given by Srawley [49].

Problem II: Constant Velocity Propagation in a Creeping Strip

This problem is concerned with a finite height, infinitely wide strip, with a semi-infinite crack. Loading consists of uniformly applied displacement rates at the top and bottom edges. This problem has been chosen for two reasons. First, since the strip is infinitely wide and the boundary conditions do not change with time, the propagating crack-tip fields can be expected to reach a "convecting steady-state" creep condition. Here we use the phrase "convecting steady-state" to mean that the field remains unchanged in time with respect to a coordinate system which is centered at and moving with the crack-tip. This terminology is used so as not to confuse this condition with the usual steady-state creep condition in which material stress rates are zero.
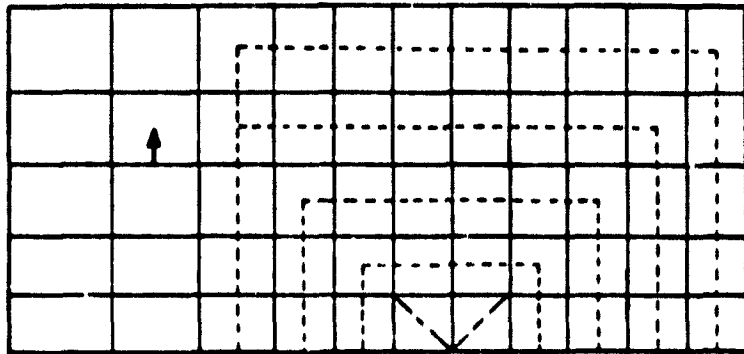
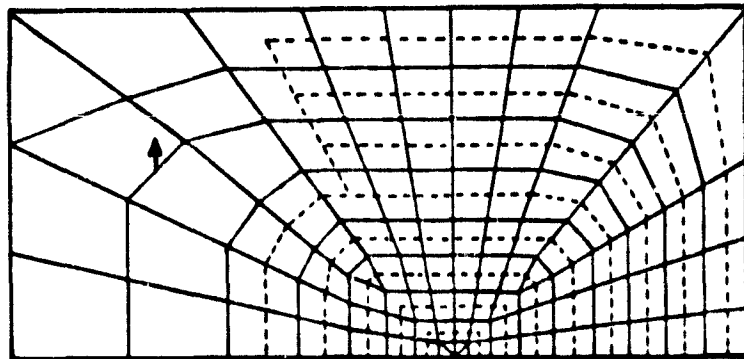**55 elements:**
198 nodes
384 d.o.f.

57 elements:
200 nodes
388 d.o.f.

a. The 55 (square crack tip elements) and 57 (triangular crack tip elements) element meshes

b. The 102 element mesh (331 nodes; 642 d.o.f.)
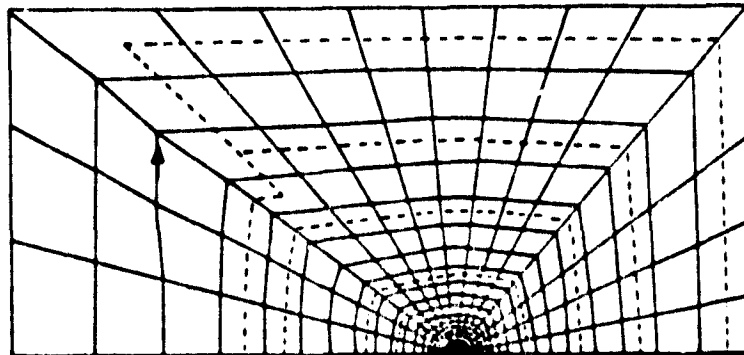
c. The 300 element mesh (941 nodes; 1840 d.o.f.)

Fig. 5.2 Finite element meshes for the compact specimen
(contour integral paths are indicated by dashed lines)

Table 5.1 Summary of Computational Aspects and Comparison with Results from the Literature

Solution No.	Mesh description (see Fig. 3)	Elastic Solution				Creep Solution				
		load point displacement (mm)	J_1 (N/mm)	difference from 24.2 [49](%)	CP time[†] (sec)	At initial/final[†] (hrs)	number of steps[†]	CP time[†] per step (sec)	quasi steady-state[†] C^* (N/m·hr)	difference from [12] 134 (%)
1	55 elements (non-singular)	0.224	22.8	(-5.8)	15	1.0 /34	40	5	90.	-32.8)
2	57 elements (1/4-point)	0.234	24.2	(0.0)	15	0.009 /17	61	5	121.	(- 9.7)
3	102 elements (non-singular)	0.231	24.0	(-0.8)	34	0.02 /24	50	8	116.	(-13.4)
4	102 elements p 3 y = 40 mm (non-singular)	0.232	24.0	(-0.8)	34	0.02 /24	50	8	116.	(-13.4)
5	102 elements (1/4-point)	0.233	24.3	(0.4)	34	0.0004/ 6.0	143	8	130.	(- 3.0)
6	300 elements (non-singular)	0.234	24.1	(-0.4)	276	0.0008/ 7.3	121	32	131.	(- 2.2)
7	57 elements (elastic, 7-node)	0.234	24.2	(0.0)	18	0.005 /16	66	5	121.	(- 9.7)
8	57 elements (creep, 7-node)	0.229	23.6	(-2.5)	18	0.005 / 9.1	97	5	126.	(- 6.0)
9	102 elements (elastic, 7-node)	0.233	24.2	(0.0)	38	0.0003/ 6.4	90	8	131.	(- 2.2)
10	102 elements (creep, 7-node)	0.232	24.1	(-0.4)	38	0.0003/ 3.7	132	9	132.	(- 1.5)

*Control Data CYBER 74
†Solutions 1-8 are stopped at 600 hours; solutions 9-10 are stopped at 300 hours

In the convecting steady-state case, stress rates for material points are not zero. As a result, C_1^* cannot (in a strict sense) be a valid crack-tip parameter. As should be clear from earlier discussions, $(\dot{T}_1)_c$ is a valid parameter at all crack speeds since it does not require material stress rates to be zero. From a practical point of view, if the crack speed is low enough, then one can expect C_1^* to be a useful quantity. By varying the crack propagation speeds for this problem over the range of velocities observed experimentally (for a given material), it should be possible to determine if this range has any portions in common with the range of velocities for which C_1^* is a useful parameter.

The second reason for choosing this problem is that C_1^* can be evaluated analytically for the special case when the crack is stationary. This allows an independent check on the finite element calculations and serves as a reference for the analyses in which the crack is propagating. The analytical evaluation of C_1^* parallels the evaluation of J_1 for a similar elastic strip problem as discussed by Rice [50]. (See Appendix E) It should be noted that C_1^* has been shown to be related to the steady-state value of $(\dot{T}_1)_c$ and therefore it is possible to obtain $(\dot{T}_1)_{css}$ for the stationary crack case from C_1^* and equation (B.1) of Appendix B. The direct evaluation of $(\dot{T}_1)_c$ in terms of either its integral representation or its energy representation requires knowledge of the stresses in the region of the strip adjacent to the crack-tip and therefore is not a trivial task.

The material properties used in this problem are representative of 304 stainless steel at 650°C. These material properties and the finite element discretization are given in Fig. 5.3. The mesh for this problem may at first appear rather coarse; however, elastic and steady-state creep solutions obtained with this mesh are sufficiently accurate to justify its use. The comparison of computed elastic J_1 values and steady-state C_1^* values with their analytic
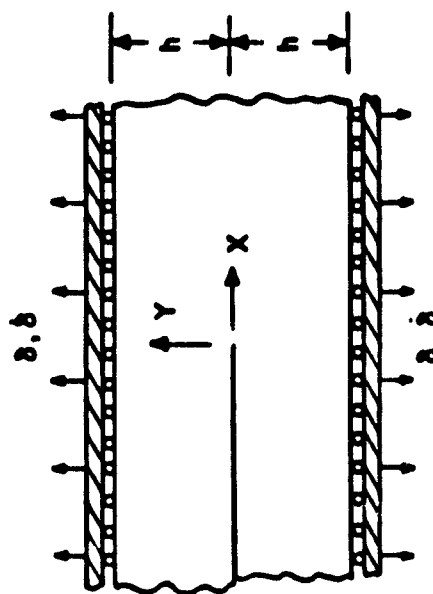
Fig. 5.3 Strip geometry, finite element mesh and material properties
(contour integral paths are indicated by dashed lines)

Table 5.2 Summary of Analysis Parameters for Creep Crack Growth in the Plane Strain Strip of Fig. 5.3

C_1^* (N/mm·hr)	Analytic Results				Computed Results		$\frac{da}{dt}$ from (6.4) (mm/hr)	
	remote τ_{yy} (MPa)	$\dot{\delta}$ (mm/hr)	δ (elastic) (mm)	J_1 (N/mm)	C_1^* (N/mm·hr)	J_1 (N/mm)	average	upper bound
0.05	83	$3.44 \cdot 10^{-4}$	$5.04 \cdot 10^{-2}$	4.18	$4.99 \cdot 10^{-2}$	4.19	$1.00 \cdot 10^{-4}$	$5.00 \cdot 10^{-4}$
5.0	148	$1.94 \cdot 10^{-2}$	$8.95 \cdot 10^{-2}$	13.2	4.99	13.2	$2.22 \cdot 10^{-2}$	$1.11 \cdot 10^{-1}$
50.0	197	$1.45 \cdot 10^{-1}$	$1.19 \cdot 10^{-1}$	23.5	49.8	23.5	$3.30 \cdot 10^{-1}$	1.65

values is given in Table 5.2.

Problem III: Creep Crack Growth in Double-Edge-Crack Specimens

The purpose of considering this problem is to apply the model to a problem for which experimental data exists. While much experimental data has been reported in the literature, most authors do not include sufficient information to allow a numerical simulation of their experiments. The current problem is based on the experiments of Koterazawa and Iwata [51]. The primary reasons for selecting this work for study are that crack length versus time histories were given and that the experiments were performed on 304 stainless steel for which high temperature elastic and creep properties were already available.

The geometry of the experimental specimens is given in Fig. 5.4. The finite element mesh for the calculations is shown in Fig. 5.5 with contour integral paths being indicated by dashed lines. It can be seen that the mesh takes advantage of the two planes of symmetry for the specimen and does not model the 60° notch.[1] The initial crack length indicated in Fig. 5.5 corresponds to the notch depth in the specimen. All calculations for this specimen assume plane stress conditions and use the material properties given in Fig. 5.3. Elastic J_1 results for two crack lengths are compared in Table 5.3 with those (based on formulas for K_I) from [52] and are seen to be in good agreement.

Compact Specimen Analyses

The following describes several calculations for a compact specimen during transition from an initial elastic state to one of steady-state creep. The geometry, loading, material properties and other details were described in the first section of this chapter as Probelm I. We first consider results for the 300 element mesh of Fig. 5.2 in terms of C_1^* and then $(\dot{T}_1)_c$. Then we address

---

[1]Modeling the notch would have required the mesh shifting subroutines to be generalized.
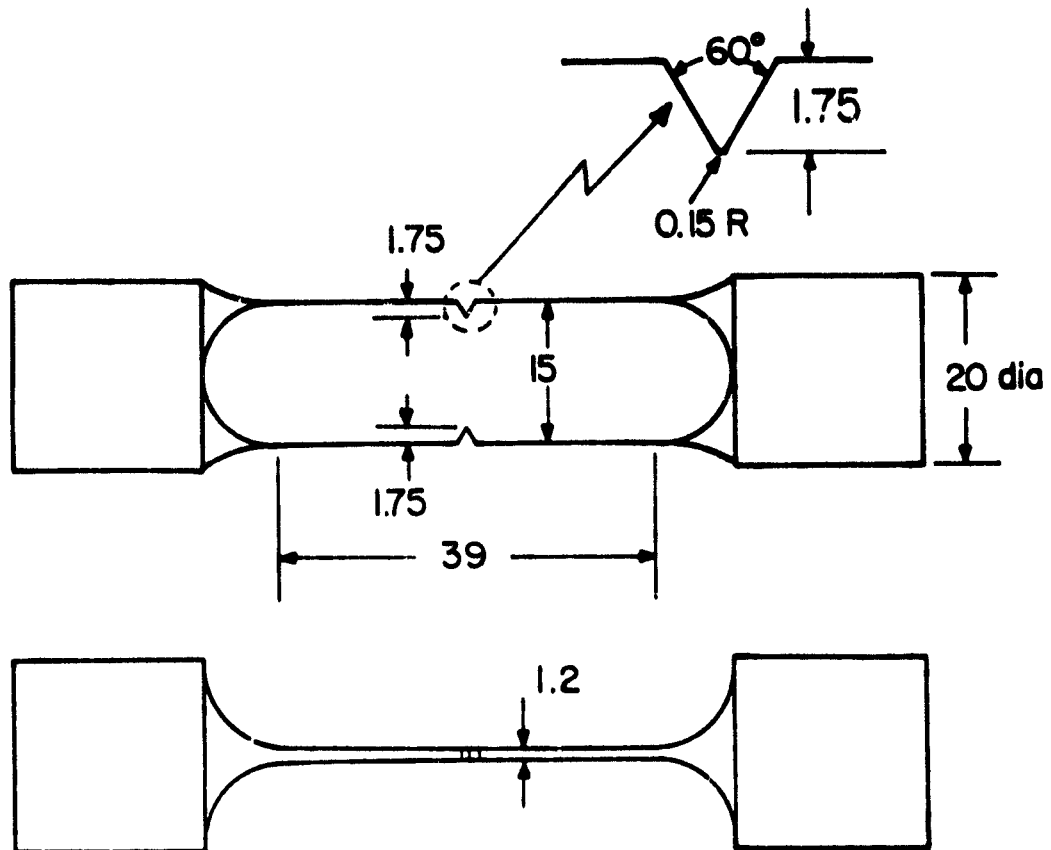
(dimensions in mm)

Fig. 5.4 Double-edge-notch specimen geometry used by
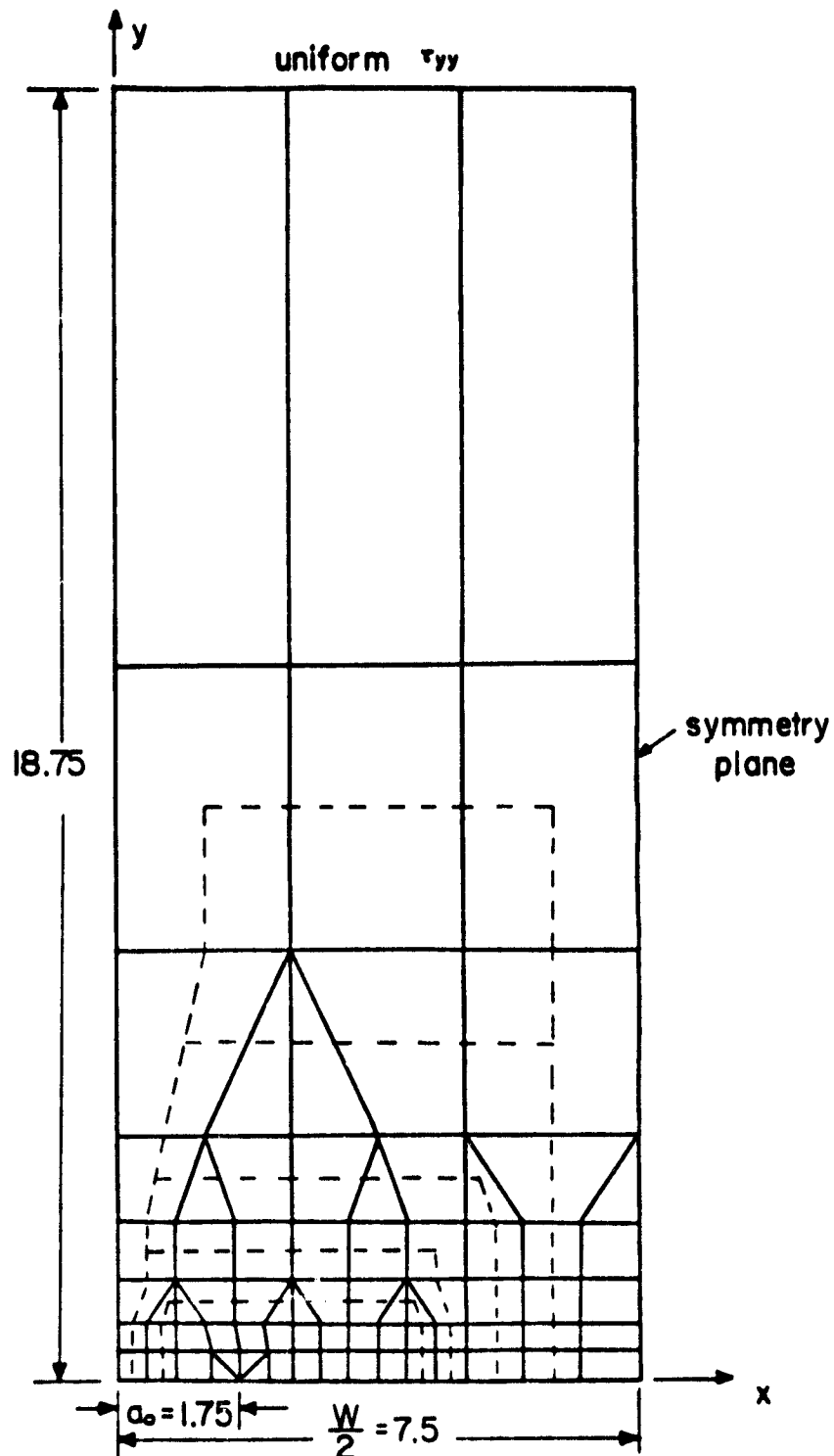Koterazawa and Iwata [51].

Fig. 5.5 Finite element mesh for simulation of
double-edge-notch experiments
(contour integral paths are indicated by dashed lines)

Table 5.3 Computational Aspects of the Elastic and Non-Steady Creep
Portion of the Double-Edge-Crack Calculations

applied stress (MPa)	crack length (mm)	Elastic Solution			Creep Solution		
		J_1 (N/mm)	difference from [52] (%)	CP time* (sec)	Δt(hr) initial/final	steps to steady-state†	total CP time (sec)
157	1.75	1.12	(-2.1)	38	$8 \cdot 10^{-8}/1.9 \cdot 10^{-2}$	90	795
176	1.75	1.40	(-2.6)	38	$8 \cdot 10^{-8}/9.5 \cdot 10^{-3}$	100	880
157	2.75	1.79	(-3.3)	38	$4 \cdot 10^{-8}/8.6 \cdot 10^{-3}$	211	1820
176	2.75	2.25	(-3.2)	38	$2 \cdot 10^{-8}/4.4 \cdot 10^{-3}$	205	1770

*Control Data CYBER 74

†Solutions are stopped at times indicated in Figs. 5.19 and 5.20

the topics of mesh refinement and the use of special crack-tip singularity elements.

Calculation of $(\dot{T}_1)_c$ and C_1^* for Nonsteady Creep

The path-independence of $(C_1^*)^\xi$ during nonsteady creep is illustrated in Fig. 5.6 using results from the 300 element mesh. The ξ superscript designates the particular Γ_{234} contour which is used, with ξ being the nondimensional distance from the crack-tip to the point where the contour crosses the crack plane. Therefore, ξ is zero at the crack-tip and has a maximum value of unity when the contour is at the boundary of the specimen. Values of $(C_1^*)^\xi$ are plotted as a function of time for nine values of ξ ranging from 0.03 to 0.92. It is seen that $(C_1^*)^\xi$ is largest for contours close to the crack-tip (small ξ) and that as steady-state is approached, the values from all contours converge to C_1^*. The solution has essentially reached steady-state at 300 hours. After 300 hours, the values of $(C_1^*)^\xi$ for all nine contours are within 1.5 percent of their average value. This value of C_1^*, as well as values from calculations with the other meshes, is given in Table 5.1.

Now we consider computed values of $(\dot{T}_1)_c^\epsilon$ as approximated by $(\Delta T_1)_c^\epsilon/\Delta t$. The values of $(\Delta T_1)_c^\epsilon$ are obtained through the specialization of (2.10) to the case of infinitesimal strains, small deformations, symmetric mode I behavior and traction-free surfaces:

$$(\Delta T_1)_c^\epsilon = \int_{\Gamma_{234}} \left[n_1 \Delta W - n_j (\tau_{ij} + \Delta \tau_{ij}) \frac{\partial \Delta u_i}{\partial x_1} \right] dS \qquad (5.1)$$

$$- \int_{V_t - V_\epsilon} \frac{\partial \tau_{ij}}{\partial x_1} \Delta \epsilon_{ij} dV$$

Since $(\dot{T}_1)_c$ is the limit of $(\dot{T}_1)_c^\epsilon$ as ϵ goes to zero, $(\dot{T}_1)_c^\epsilon$ is plotted as a function of ϵ for several times (see Fig. 5.7). In this figure, ϵ is the nondimensional size of V_ϵ and is measured in the same manner as ξ, the
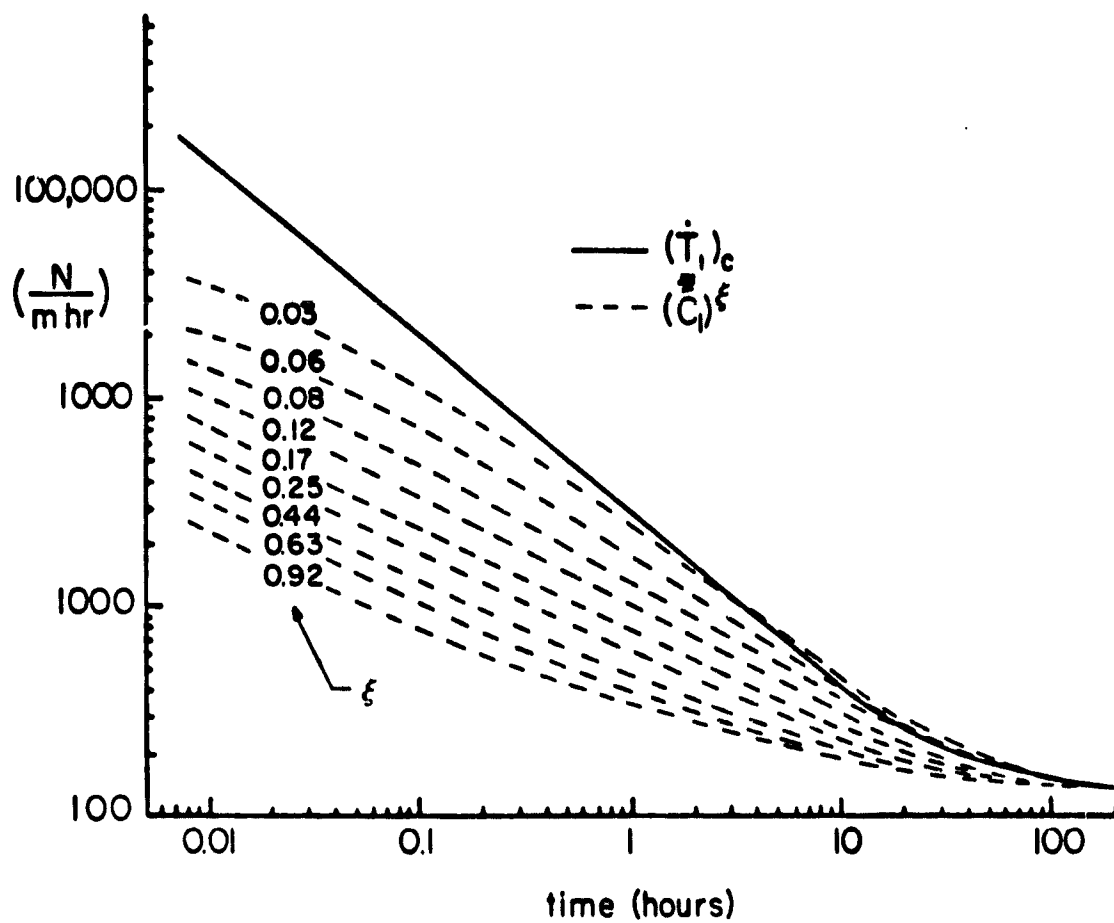
Fig. 5.6 $(\dot{T}_1)_c$ and $(C_1^*)^\xi$ as a function of time for several contour integral paths
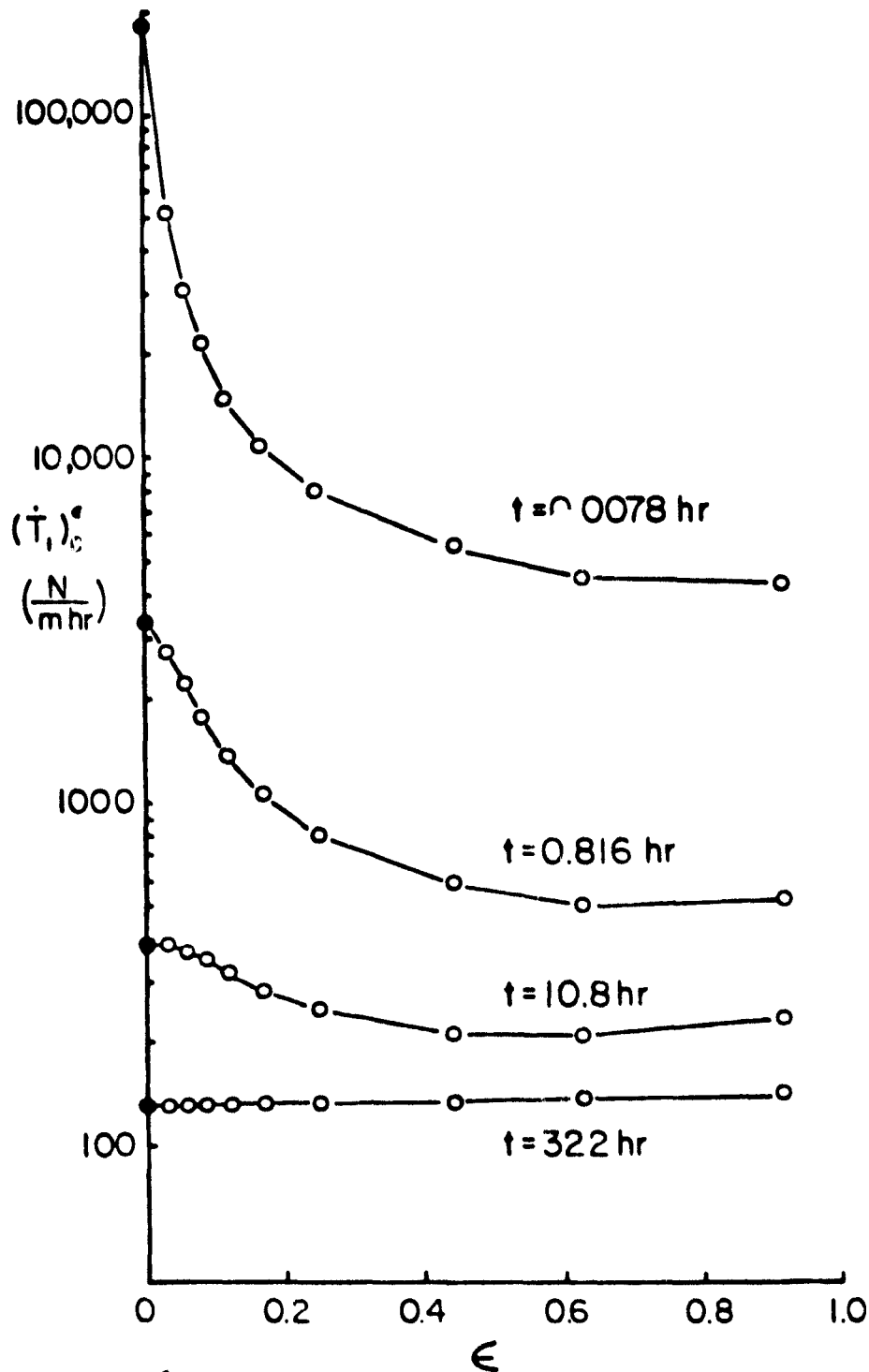
(results from 300 element mesh)

Fig. 5.7 $(\dot{T}_1)_c^\epsilon$ as a function of ϵ for several times
during non steady creep
(results from 300 element mesh)

nondimensional size of Γ_{234}. The open points are the values of $(\dot{T}_1)_c^\epsilon$, as computed by (5.1), for nine contours in the 300 element model. The value of the crack-tip parameter $(\dot{T}_1)_c$ is given by the intersection of each respective curve with the $\epsilon = 0$ axis. Due to the large gradient in $(\dot{T}_1)_c^\epsilon$ for small ϵ it is seen that the accuracy of any extrapolation based solely on these evaluations of $(\dot{T}_1)_c$ (i.e., open points) would be of questionable accuracy, except perhaps near steady-state conditions. The solid points at $\epsilon = 0$ in Fig. 5.7 have been obtained using (2.14). It is seen that these values of $(\dot{T}_1)_c$ appear to be reasonable extrapolations of the curves of $(\dot{T}_1)_c^\epsilon$ (5.1) thus giving some degree of confidence in their accuracy.

Path Independence of $(\dot{T}_1)_c$

Based on arguments put forth in earlier portions of this paper, the value of $(\dot{T}_1)_c$ obtained through (2.14) should be independent of the path (i.e., Γ_{234}) which is used in its computation. This path-independence is illustrated by Fig. 5.8a where $(\dot{T}_1)_c$ is plotted as a function of the nondimensional distance of Γ_{234} from the crack-tip, ξ, for several times. Generally, the path-independence is seen to be quite good. The largest deviation from path-independence in this figure is for the intermediate time of 10.8 hours with the difference between the extreme contour values being less than three percent. To further emphasize this path-independence, $(\dot{T}_1)_c$ is plotted as a function of time in Fig. 5.6. As a result of its path-independence, $(\dot{T}_1)_c$ is represented by a single curve. Interestingly, this curve is a straight line for times before approximately 10 hours.

Riedel and Rice [36] have arrived at the following approximation for K_σ (which they call A(t) based on the assumed approximate path-independence of J_1 during the initial portion of nonsteady creep:

$$K_\sigma \doteq \left[\frac{K_I^2 (1 - \nu^2)/E}{(n+1)\gamma It} \right] \frac{1}{n+1} \tag{5.2}$$

a. 300 element mesh

b. 102 element mesh with
quarter-point singularity

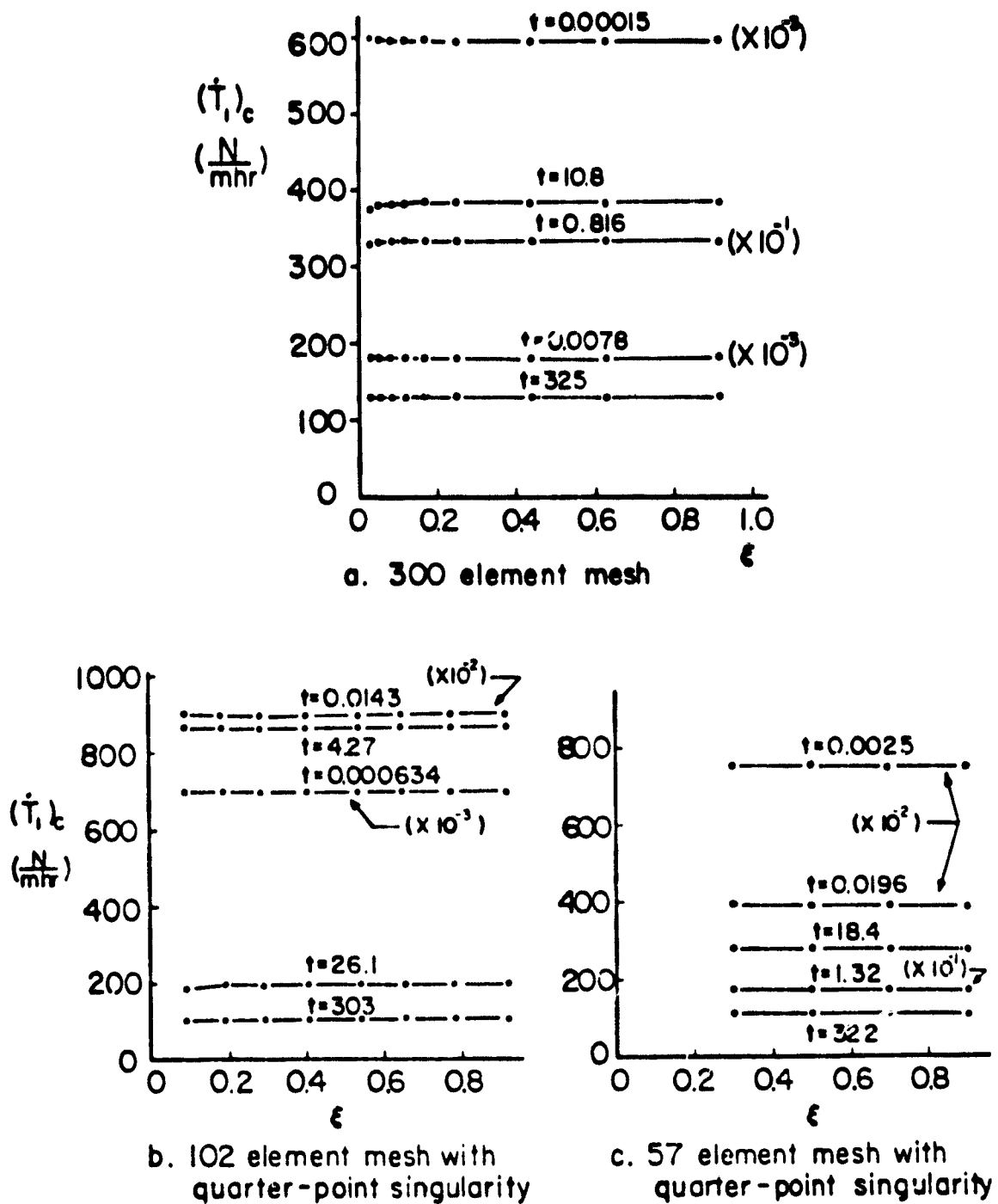c. 57 element mesh with
quarter-point singularity

Fig. 5.8 Path-independence of $(\dot{T}_1)_c$ for several times
during non steady creep
(ξ is the non-dimensional size of Γ_{234})

Comparing (5.2) with (2.50) one concludes that $(\dot{T}_1)_c$ should behave like $1/t$ for times when (5.2) is valid. In a log-log plot of $(\dot{T}_1)_c$ versus time this would result in a straight line with a slope of -1. The straight line shown in Fig. 5.6 is inclined from the horizontal by 40° and therefore has a slope of -0.84. The current work has resulted in some evidence that J_1 is approximately path-independent during initial nonsteady creep but that its value tends to increase with time. This tendency for J_1 to increase with time could explain the rather significant departure of the current results from the behavior of (5.2).

Quarter-Point Singularity Element Calculation

We next consider the results of computations using 57 and 102 element meshes with quarter-point singularities. The purpose of considering these less refined meshes is to determine if the expense and effort in using the 300 element model is necessary for obtaining accurate results. Table 5.1 summarizes the results of these meshes for the limiting cases of purely elastic behavior and steady-state creep behavior. For the elastic problem it is seen that the results from these meshes agree with the 300 element mesh results to within one percent. At steady-state the 102 element model still agrees with the 300 element mesh (in terms of C_1^*) to within one percent while the 57 element model now differs by approximately eight percent.

The contours used for the 57 and 102 element mesh are indicated in Fig. 5.2. The 57 element mesh has four contours while the 102 element mesh has eight. The path-independence of $(\dot{T}_1)_c$, as computed from (2.14), is illustrated for these two meshes in Fig. 5.8b and 5.8c. It is seen that the degree of path-independence in both is similar to that observed for the 300 element mesh. Since we have evidence that the 57 element mesh is less accurate than the other meshes at steady-state, it appears that high quality of the path-independence cannot generally be interpreted as meaning the solution is accurate.

To determine the adequacy of the 57 and 102 element meshes for the non-steady creep problem we now compare their $(\dot{T}_1)_c$ histories with that obtained with the 300 element mesh (see Fig. 5.9). The curve appearing in this figure has been placed through computed points from the 300 element mesh. The results of the 102 element mesh agree almost perfectly with this curve for times between 0.2 hours and 16 hours. Prior to this period and after this period the results fall below the curve by as much as 20 percent. While little can be said about the absolute accuracy of the calculations for early portions of nonsteady creep, we know (based on Appendix B) that $(\dot{T}_1)_c$ should agree numerically with C_1^* at steady-state to within a few percent. Therefore it can be said that the values of $(\dot{T}_1)_c$ from the 102 element mesh are significantly in error at steady-state. Recalling that this model gave a steady-state value of C_1^* which agree quite well with the 300 element mesh results (see Table 5.1) it is perhaps surprising that such a significant error in the steady-state value of $(\dot{T}_1)_c$ can exist. To better understand the results of this model, $(\dot{T}_1)_c^\epsilon$ is plotted as a function of ϵ in Fig. 5.10. It is noted from this figure that the values of $(\dot{T}_1)_c$ based on (2.14) (i.e., the solid points) appear to be reasonable extrapolations for times when the results are in agreement with the 300 element mesh results. However, as steady-state is approached, it is seen that these solid points no longer appear reasonable. If, however, one extrapolates the values of $(\dot{T}_1)_c^\epsilon$ to $\epsilon = 0$ for the bottom two curves of Fig. 5.10, it is found that these values of $(\dot{T}_1)_c$ are in good agreement with the 300 element mesh results.

In comparing the equations for evaluating C_1^*, $(\dot{T}_1)_c^\epsilon$ and $(\dot{T}_1)_c$, it is seen that $(\dot{T}_1)_c$ is the only one of the three which involves an integration over the crack-tip quarter-point elements. Based on this and the apparently good accuracy of C_1^* and $(\dot{T}_1)_c^\epsilon$ it is believed that the integration over these elements is the major cause of discrepancy in $(\dot{T}_1)_c$ between the 102 and 300 element mesh calculations.
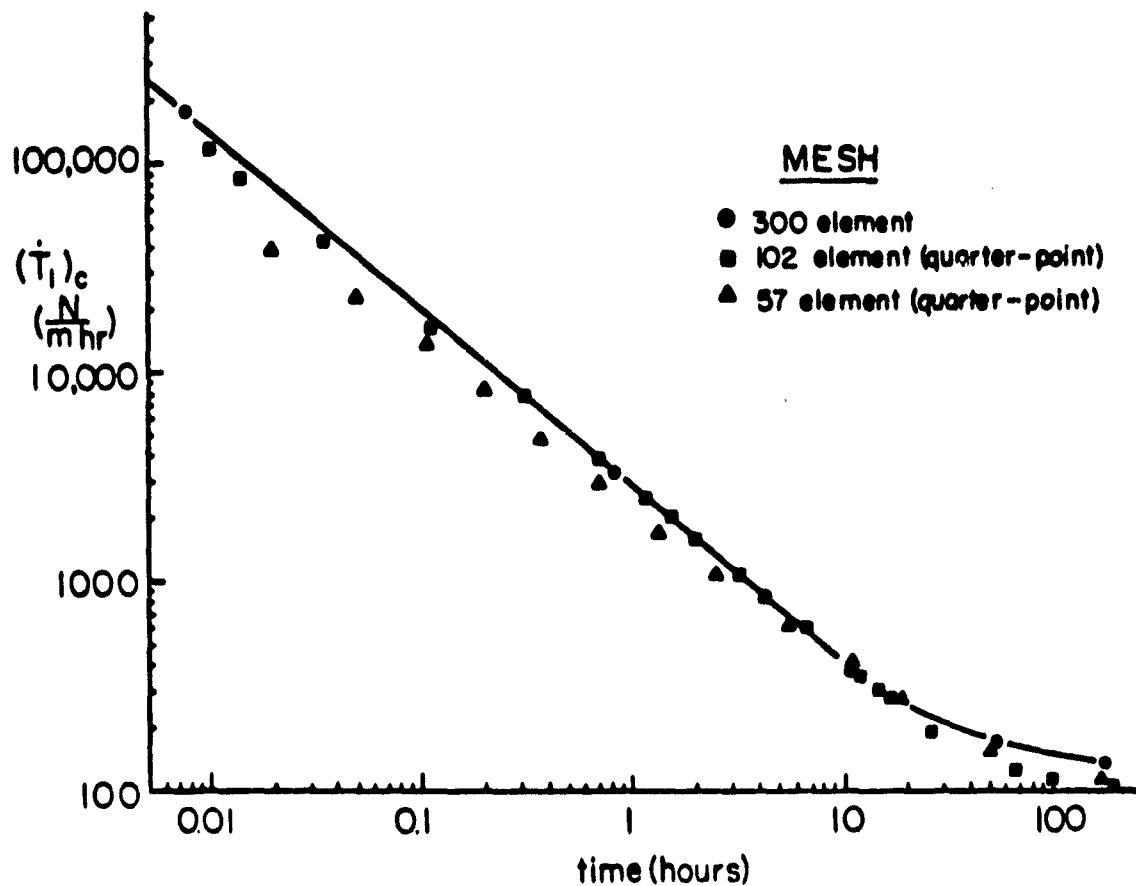
Fig. 5.9 Comparison of $(\dot{T}_1)_c$ from calculations
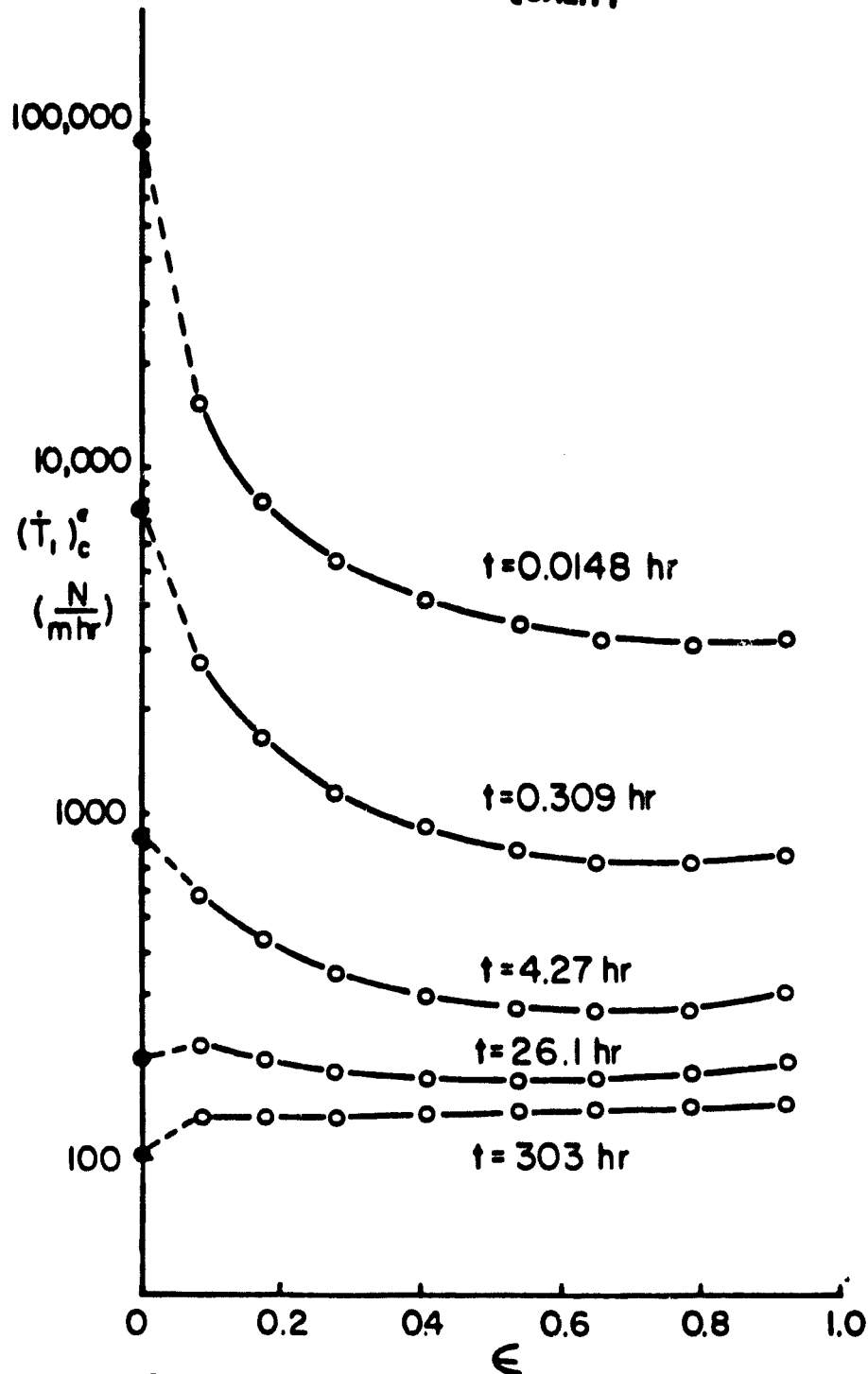with three finite element meshes

Fig. 5.10 $(\dot{T}_1)_c^\epsilon$ as a function of ϵ for several times
during non-steady creep
(results from 102 element mesh with quarter-point singularity)

The 57 element results do not compare favorably with the curve of Fig. 5.9 for any significant portion of the solution. For most times the values of $(\dot{T}_1)_c$ fall below the curve with the percent difference ranging from 50 percent at $t = 0.02$ hr. to 15 percent at steady-state. Based on the discrepancy of C_1^* indicated in Table 5.1 and in the generally bad comparison of $(\dot{T}_1)_c$ in Fig. 5.9, it appears that the 57 element mesh with quarter-point singularity is not sufficiently refined for accurate creep calculations. This conclusion is perhaps a bit unexpected considering the degree of accuracy which this mesh displayed for the elastic probelm (see Table 5.1). The reason for this drastic change of accuracy in going from elastic to creep behavior may be that the crack-tip strain singularity (i.e., $r^{-1/2}$) is inappropriate for the $r^{-n/(n+1)}$ type behavior expected to exist during creep. This topic is addressed in the following.

HRR Singularity Element Calculations

Based on the above observations, several analyses have been made using the seven-noded variable singularity element described previously (Section IV). The elastic solutions obtained with this element agree very well with those using the quarter-point isoparametric element as can be seen from the entries of J_1 in Table 5.1. Also included in Table 5.1 are the quasi-steady-state values of C_1^*. The introduction of the correct strain singularity for steady-state creep ($r^{-n/(n+1)}$) does not significantly affect the 102 element mode's C_1^* but does imporve that of the 57 element model.

The analyses which use the seven-node singular element have the same singularity for the elastic solution and the subsequent creep solutions. Attempts at changing the singularity from the elastic $r^{-1/2}$ to the $r^{-n/(n+1)}$ value between the elastic and first creep solution have created numerical difficulties due to the disequilibrium introduced in the process. No attempt at a gradual transition has been made.

The $(\dot{T}_1)_c$ results using the seven-noded singular element are shown in Fig. 5.11. The solid curve represents the results of the 300 element model. The evaluation of $(\dot{T}_1)_c$ is according to (2.14) with the numerical procedures being identical to those employed with the quarter-point elements except for the contribution of the singular elements to the volume integral. For the quarter-point elements, the stresses are assumed to be distributed lineraly with respect to the local coordinates. The volume integral is then evaluated in terms of quantities at the 2x2 Gauss ponts. For the seven-node element, linear interpolation is used and in addition, several calculations are done assuming radial dependence of the type $\sigma = a + b^{-/(1+n)}$. It can be seen from Fig. 5.11 that none of the calculations agree well with the 300 element results.

Based on this set of calculations, the general disagreement in $(\dot{T}_1)_c$ between the singular crack-tip element models and the 300 element model does not appear to be due to the strength of the singularity which is introduced at the crack-tip. The general accuracy of C_1^* for all the solutions with either elastic or creep type strain singularities supports this view. Rather, it seems likely that the difficulty in computing the volume integral of (2.14) stems from the crack-tip element fields not satisfying the condition

$$\underset{\substack{Lt \\ \epsilon \to 0}}{} \int_{-\pi}^{\pi} \frac{\partial \tau_{ij}(\epsilon, \theta)}{\partial x_1} \Delta \epsilon_{ij}(\epsilon, \theta) d\theta = 0 \tag{5.3}$$

From the discussion of Appendix A it can be seen that if this condition is not satisfied while at the same time the fields have the correct asymptotic (singular) radial dependence, then the volume integral of (2.14) does not exist.

It therefore appears that accurate evaluation of $(\dot{T}_1)_c$ using (2.14) cannot be accomplished if one uses crack-tip singular elements which provide
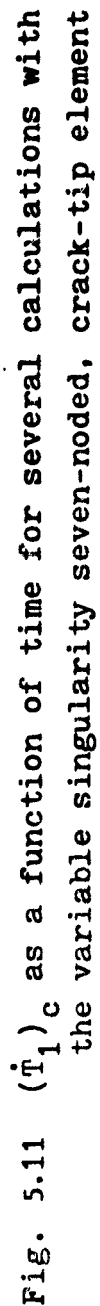
Fig. 5.11 $(\dot{T}_1)_c$ as a function of time for several calculations with the variable singularity seven-noded, crack-tip element

for the satisfaction of condition (5.3). At this point, it appears that one must use a rather refined non-singular mesh (such as the current 300 element mesh) or introduce special crack-tip elements which satisfy (5.3) in order to compute $(\dot{T}_1)_c$ accurately. The next section illustrates that for many probelms of practical importance, a more attractive alternative may exist.

$(\dot{T}_1)_c^{\epsilon}$ as a Crack-Tip Field Parameter

The previous discussion has pointed out some computational difficulties involved with evaluating $(\dot{T}_1)_c$. It was concluded that these difficulties are associated with the contirbution of the crack-tip singularity elements to the volume integral of (5.1). It has been seen that despite the elastic strain singularity introduced by the quarter-point element scheme, the 102 element mesh gives accurate values of C_1^*. Assuming this reflects the general accuracy of this solution, it is desirable to use this relatively inexpensive model as opposed to using a very refined non-singular mesh or to introducing a special crack-tip element which satisfies condition (5.3).

The effect of deleting the crack-tip singular elements from the volume integral of (2.14) is shown in Fig. 5.12. Deleting these elements means that we are in fact evaluating $(\dot{T}_1)_c^{\epsilon}$ where V_{ϵ} is the volume encompassed by the crack-tip elements. We will denote this particular $(\dot{T}_1)_c^{\epsilon}$ as $(\dot{T}_1)_c^{\delta}$. It will be shown that depending on the relative size of the crack-tip elements and the proximity of the solution to steady-state condition, $(\dot{T}_1)_c^{\delta}$ is a good approximation to $(\dot{T}_1)_c$.

The solid curve in Fig. 5.12 represents the results of the 300 element mesh. The dashed curves are $(\dot{T}_1)_c^{\delta}$ in the case of the 57 and 102 element meshes and is $(\dot{T}_1)_c^{\epsilon}$ with $\epsilon = 0.03$ in the case of the 300 element mesh. The crack-tip element sizes for the 57 and 102 element meshes are 10 mm and 2.5 mm (or 20 and five percent of the ligament size), respectively.
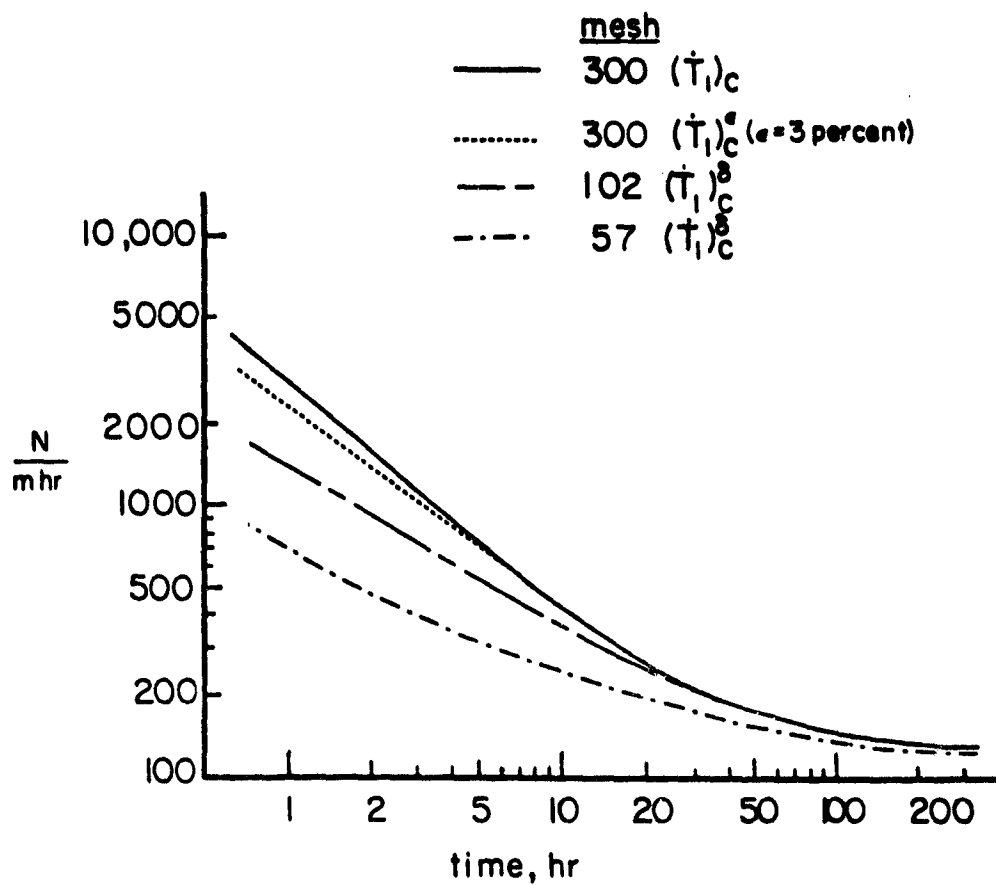
Fig. 5.12 Comparison of $(\dot{T}_1)_c^{\delta}$ and $(\dot{T}_1)_c$ histories
for several finite element meshes

The values of $(\dot{T}_1)_c^\delta$ for the 102 element mesh coincide with the solid cuve for times after about 30 hours. Therefore $(\dot{T}_1)_c^\delta$ is a valid, path independent, crack-tip parameter for times after about 30 hours and for values of $(\dot{T}_1)_c$ beginning at approximately 1.6 of the steady-state value. Fig. 5.6 shows that C_1^* is still significantly path- dependent at 30 hours and thus is not an acceptable crack-tip parameter until much later.

The curve of $(\dot{T}_1)_c^\epsilon$, ($\epsilon = 0.03$), for the 300 element model seems to indicate that the validity of $(\dot{T}_1)_c^\delta$ can be expanded to earlier times by reducing the size of the quarter-point elements. For example, a δ of three percent of the ligament would apparently result in $(\dot{T}_1)_c^\delta$ being valid as early as seven hours and for values of $(\dot{T}_1)_c^\delta$ as large as 4.3 the steady-state value of $(\dot{T}_1)_c$. The curve of $(\dot{T}_1)_c^\delta$ for the 57 element mesh tends to approach the solid curve as steady-state is approached but never acutally converges even at steady-state. This indicates that this mesh is too coarse for $(\dot{T}_1)_c^\delta$ to be a useful parameter.

Constant Velocity Propagation in a Strip

We now present some calculations for the cracked strip problem previously referred to as Problem II. The geometry, loading and material properties for this problem are summarized in Fig. 5.3. The purpose of this problem is to determine how significantly the crack-tip fields are affected by crack propagation velocities commonly observed in experiments. If for realistic crack speeds, the crack-tip field is essentially the same as for a stationary crack, then C_1^* is path independent and characterizes the crack-tip fields. In any case, $(\dot{T}_1)_c$ is a valid parameter.

As noted previously, the steady-state C_1^* values for the infinite strip problem can be obtained analytically without much difficulty. (See Appendix E.) Therefore, the procedure for this set of calculations is to select three values

- 73 -

of C_1^* which span the range of values reported in the literature. The values which have been chosen are 0.05, 5.0 and 50 N/mm.hr. Having these values, the corresponding remote steady-state τ_{yy} is determined as well as the edge displacement which will result in the same remote elastic τ_{yy}. These displacements are applied to the model elastically at $t = 0$. The resulting values of J_1 are compared to the analytic values in Table 5.2. Next, the steady-state edge displacement rates are determined. Using the elastic solution as an initial state, the displacement rate, $\dot{\delta}$, is applied until the model reaches steady-state. The computed steady-state values of C_1^* are compared to their analytic values in Table 5.2. The next step is to determine an upper bound crack velocity for each of the chosen values of C_1^*. The following formula is based on the experimental data reported in [23,24] and represents data from center-crack, double-edge-crack, single-edge-crack, compact, and round-bar specimen types.

$$\frac{da}{dt} = \alpha\, C_1^{*\,1.173} \tag{5.4}$$

where

$$\alpha = \begin{array}{l} 1.68 \cdot 10^{-2} \text{ (upper bound)} \\ 3.36 \cdot 10^{-3} \text{ (average} \end{array}$$

Having reached steady-state, the crack is propagated at the upper bound velocity given by (5.4) until it is determined that a convecting steady-state has been reached.

As noted previously, these calculations use the quarter-point crack-tip element. The crack growth simulation is accomplished through a combination of mesh shifting and remeshing as described in Appendix D. The nominal size of the crack growth increments is 0.4 mm or two percent of the crack-tip element width. For the highest velocity case ($C_1^* = 50$ N/mm.hr), this procedure results in crack growth at approximately every fifth solution step.

Results for a Plane Strain Strip

The results of the plane strain strip calculation with $C_1^* = 50$ N/mm.hr and $\frac{da}{dt} = 1.65$ mm/hr are given in Fig. 5.13. The values of $(\dot{T}_1)_c$ and C_1^* are given for the portion of the calculation prior to steady-state as well as during the crack propagation protion. The band represents the range of values obtained from the four contours illustrated in Fig. 5.3. Both $(\dot{T}_1)_c$ and C_1^* converge to the 50 N/mm.hr value at steady-state. During the crack propagation, it is seen that $(\dot{T}_1)_c$ and C_1^* do not depart significantly from their steady-state value. This means that this combination of loading and crack speed results in the crack-tip fields being essentially at steady-state conditions. This in turn means that both $(\dot{T}_1)_c$ (or $(\dot{T}_1)_c$) and C_1^* are valid crack-tip field parameters.

A closer view of the crack propagation portion of these curves is given in Fig. 5.14. The dashed curves braceting the initial portion of the solid curves represent the degree of path-independence and continue to be representative of the path-independence observed during the crack propagation steps. For both $(\dot{T}_1)_c$ and C_1^*, it is seen that the strip has essentially returned to its steady-state condition prior to each crack growth increment. It is thought that the large departure of $(\dot{T}_1)_c$ (as compared to C_1^*) is more representative of the nonsteadiness of the crack-tip field, since the validity of C_1^* in general, and the numerical evaluation of W* (2.43) in particular, are based on the existence of steady-state conditions.

The effect of remeshing is seen at approximately eight hours. The first two steps after the remeshing were found to result in rather erratic contour integral values and are not indicated in these figures. The equilibrium correction feature of the present model and the automatic time step regulation procedure both act to quickly restore equilibrium at the crack-tip.

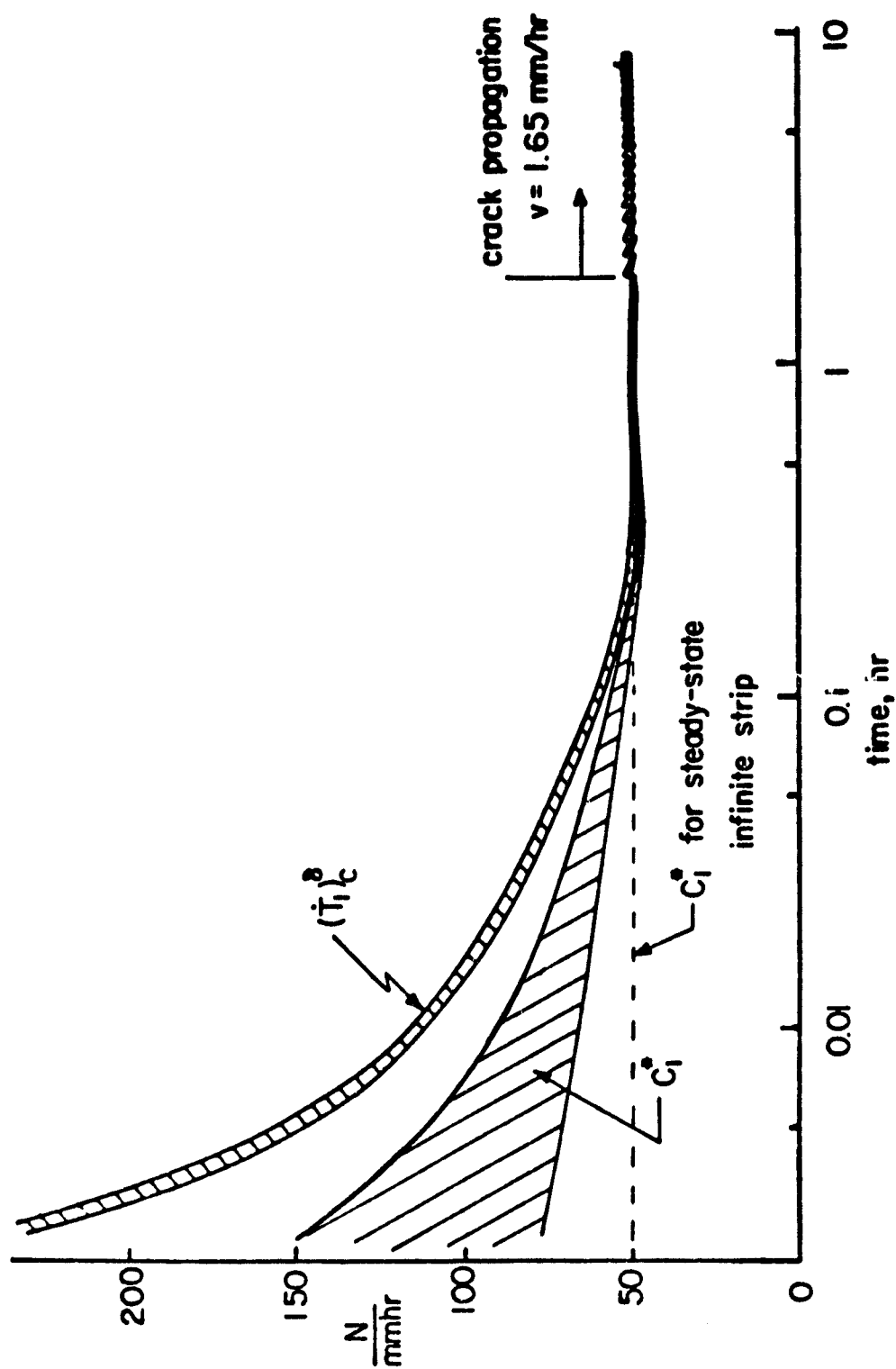The propagation portion of the calculation with $C_1^* = 5$ N/mm.hr and

Fig. 5.13 $(\dot{T}_1)^{\delta}_c$ and C^*_1 for non steady creep, steady-state creep, and crack propagation phases of a plane strain strip analysis
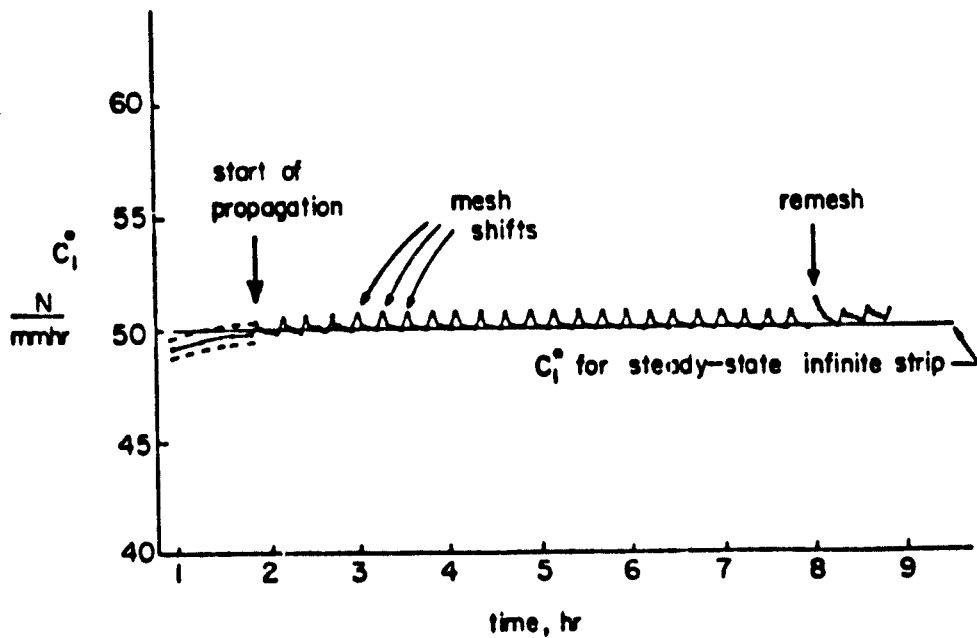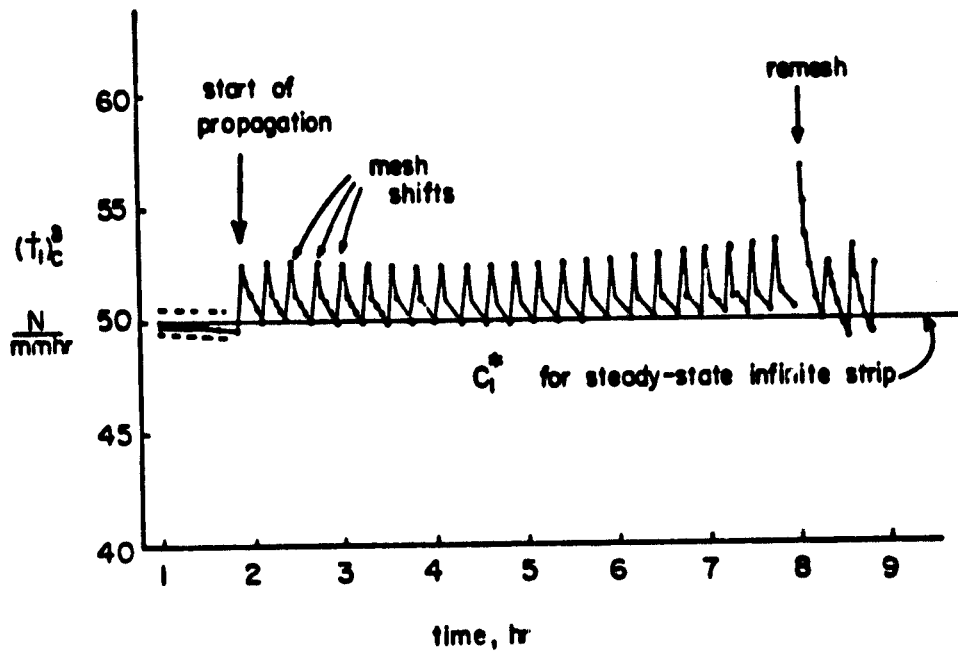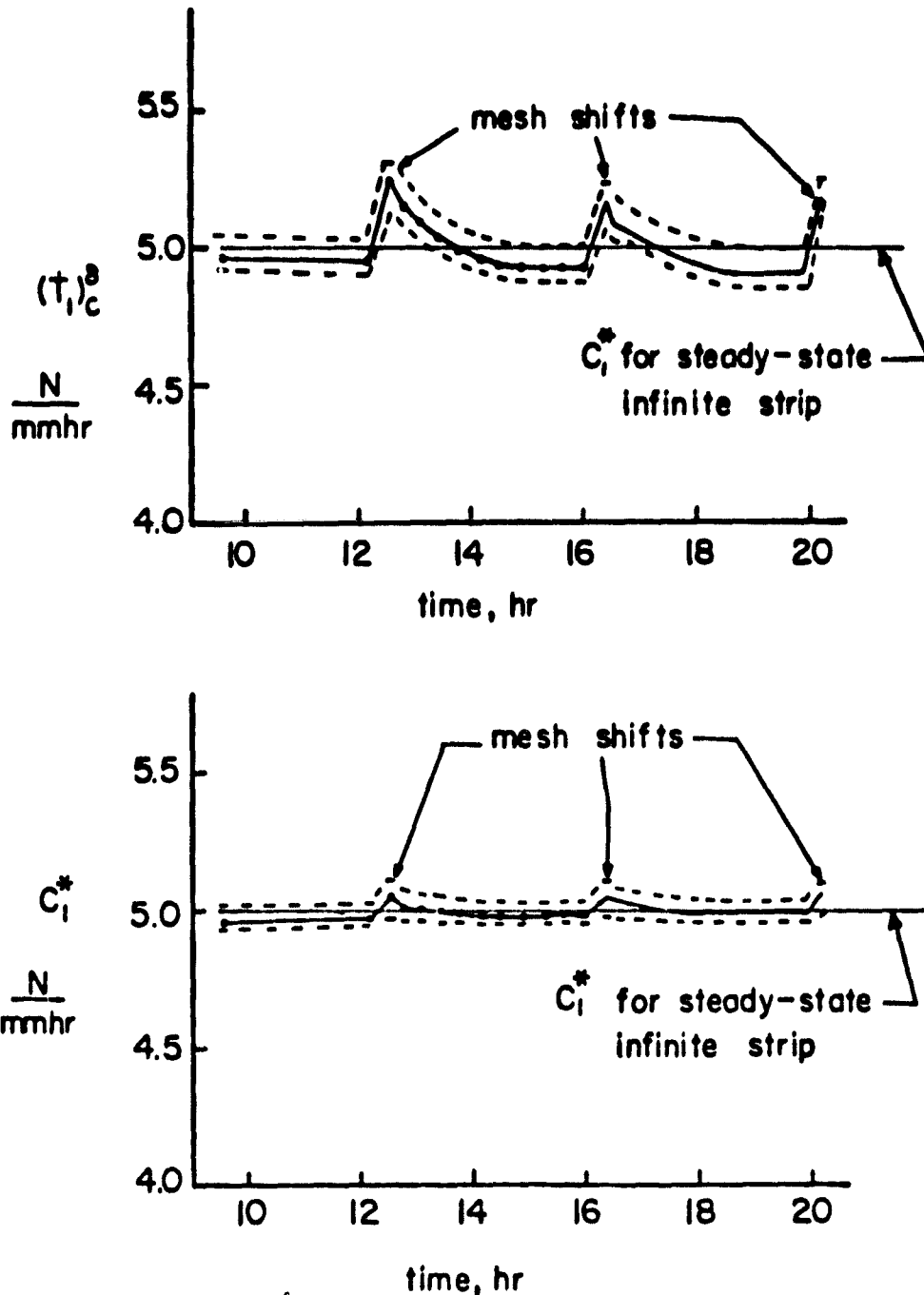
Fig. 5.14 $(\dot{T}_1)_c^6$ and C_1^* for the crack propagation portion of a plane strain strip analysis $(C_1^* = 50 \text{ N/mm} \cdot \text{hr} ; v = 1.65 \text{ mm/hr})$

$\frac{da}{dt} = 0.111$ mm/hr is given in Fig. 5.15. Here again it is seen that both $(\dot{T}_1)_c^\delta$ and C_1^* have converged to the analytical value of C_1^* (to within two percent, which is also about the degree of path-dependence). Comparing these results with those in Fig. 5.14 for the higher C_1^* and crack speed it is seen that steady-state creep conditions were not reached until 12 hours as opposed to approximately two hours in the previous case. Also, the return to the steady-state value after mesh shifting takes more time (two hours compared to 0.25 hours). However, when compared to the time between crack growth steps (both use 0.4 mm) it is seen that the lower velocity case return to steady-state well before the next growth step occurs. This result indicates that lower load levels and crack speeds are inherently closer to steady-state conditions. While this behavior may seem intuitively correct, it should be kept in mind that these results depend on the empirical formula (5.4) which is only valid for 304 stainless steel. It remains to be seen if similar behavior occurs in other materials.

A calculation has also been done for the case of $C_1^* = 0.05$ N/mm.hr. As a result of the large number of solution steps between crack growth steps, when using the maximum velocity of $5 \cdot 10^{-4}$ mm/hr, the calculations used a higher velocity ($5 \cdot 10^{-3}$ mm/hr). Even at this unrealisitcally high velocity (for this level of loading), the behavior is more steady-state-like than the case of $C_1^* = 5.0$N/mm. hr described above.

Results for a Plane Stress Strip

In both plane strain problems discussed above, the steady-state value of $(\dot{T}_1)_c$ is equal to C_1^* to within the accuracy of the calculations. This is consistent with the relationship and comparison of C_1^* and steady-state $(\dot{T}_1)_c$ given in Appendix B. According to the approximate numerical values of this appendix, there should not be as close agreement between C_1^* and $(\dot{T}_1)_c$ in the case of plane stress. The primary purpose of this analysis is to verify this predicted behavior.

Fig. 5.15 $(\dot{T}_1)^6_c$ and C^*_1 for the crack propagation portion of a plane strain strip analysis

$(C^*_1 = 5.0 \, N/mm \cdot hr \, ; \, v = 0.111 \, mm/hr)$

For this plane stress analysis, C_1^* was chosen to be 50 N/mm . hr and the crack was again propagated at 1.65 mm/hr. The remote τ_{yy}, the steady-state displacement rate, $\dot{\delta}$, and the elastic displacement, δ, are 171 MPa, 0.168 mm/hr and 0.114 mm, respectively.

The results of this calculation are given in Fig. 5.16 and 5.17. It is seen from these figures that $(\dot{T}_1)_c^\delta$ does converge to a somewhat higher value at steady-state then C_1^*. The steady-state is seen from Fig. 5.17 to be approximately 52 N/mm . hr which is higher than C_1^* by four percent. While this is a somewhat smaller difference than suggested by Appendix B, the sign of the difference is the same. In light of the approximate integration used in obtaining the numeric values in the appendix, this discrepancy is within reason. As expected, the general behavior for plane stress conditions is essentially the same as for the previous plane strain analyses. Therefore, previous observations concerning the steady-state nature of the crack-tip field during crack propagation are unchanged by the shift to plane stress conditions.

Double-Edge-Crack Specimen Analysis

The following describes several calculations and their results for the problem previously referred to as Problem III. The geometry and finite element mesh for the double-edge-crack specimen are given in Figs. 5.4 and 5.5, respectively. The material properties are those of 304 stainless steel at 650°C and are assumed to be the same as those used in the strip analyses. (See Fig. 5.3) Calculations have been made for remote applied stresses of 157 and 176 MPa. The experimental crack growth histories for these two stress levels are reproduced from [51] in Fig. 5.18. It is seen from these curves that the first two-thirds of the specimen lives are characterized by crack velocities of less than 0.01 mm/hr compared to nearly 0.5 mm/hr as rupture is approached.

The primary purpose of the following calculations is to verify the conclusions which were reached in the previously described strip calculations;
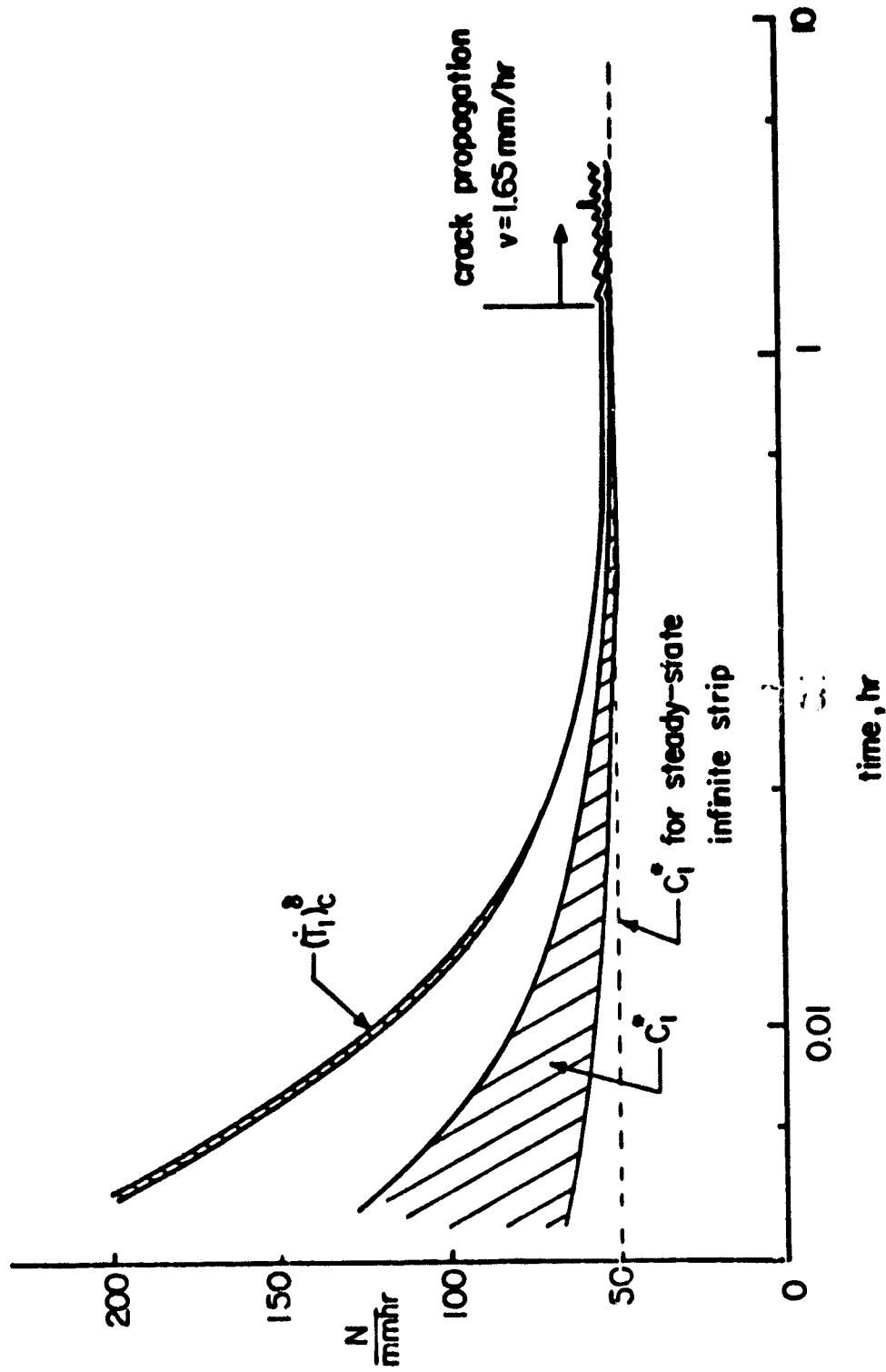
Fig. 5.16 $(\dot{T}_1)_c^\delta$ and C_1^* for non steady creep, steady-state creep, and crack propagation phases of a plane stress strip analysis
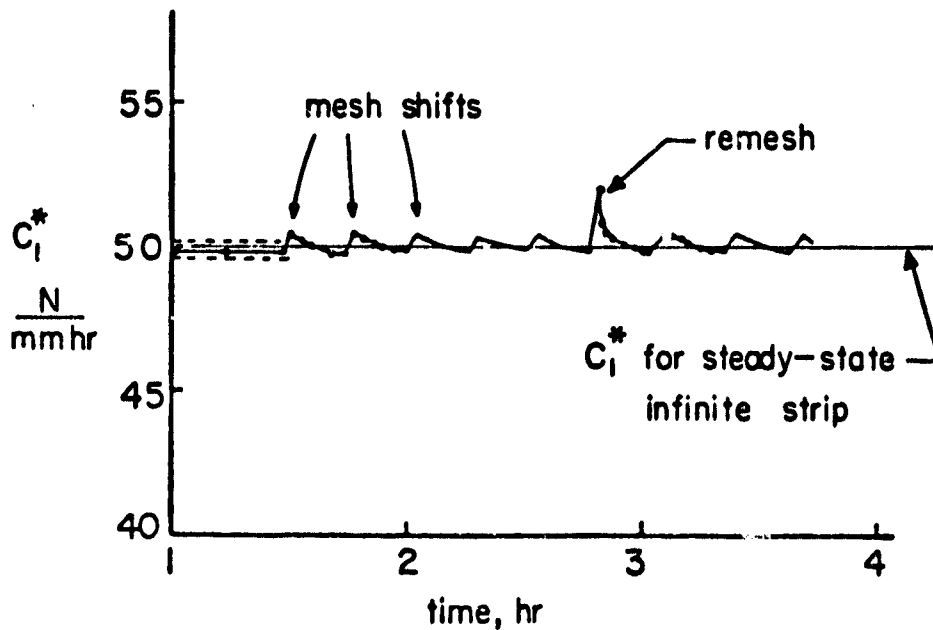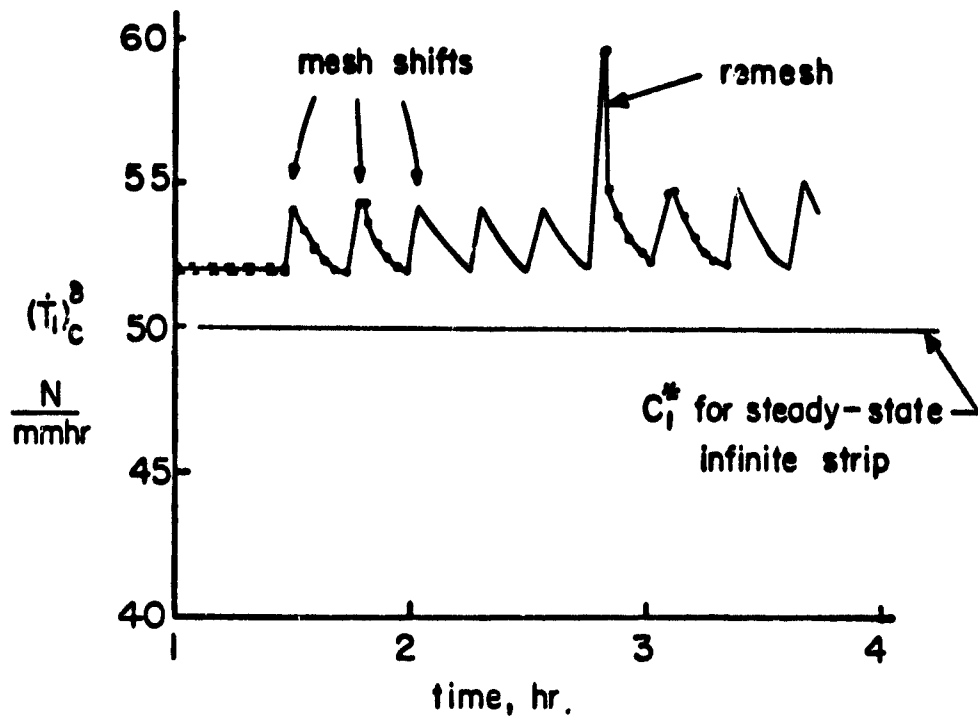
Fig. 5.17 $(\dot{T}_1)_c^\delta$ and C_1^* for the crack propagation portion of a plane stress strip analysis $(C_1^* = 50 \text{ N/mm} \cdot \text{hr}; v = 1.65 \text{ mm/hr})$
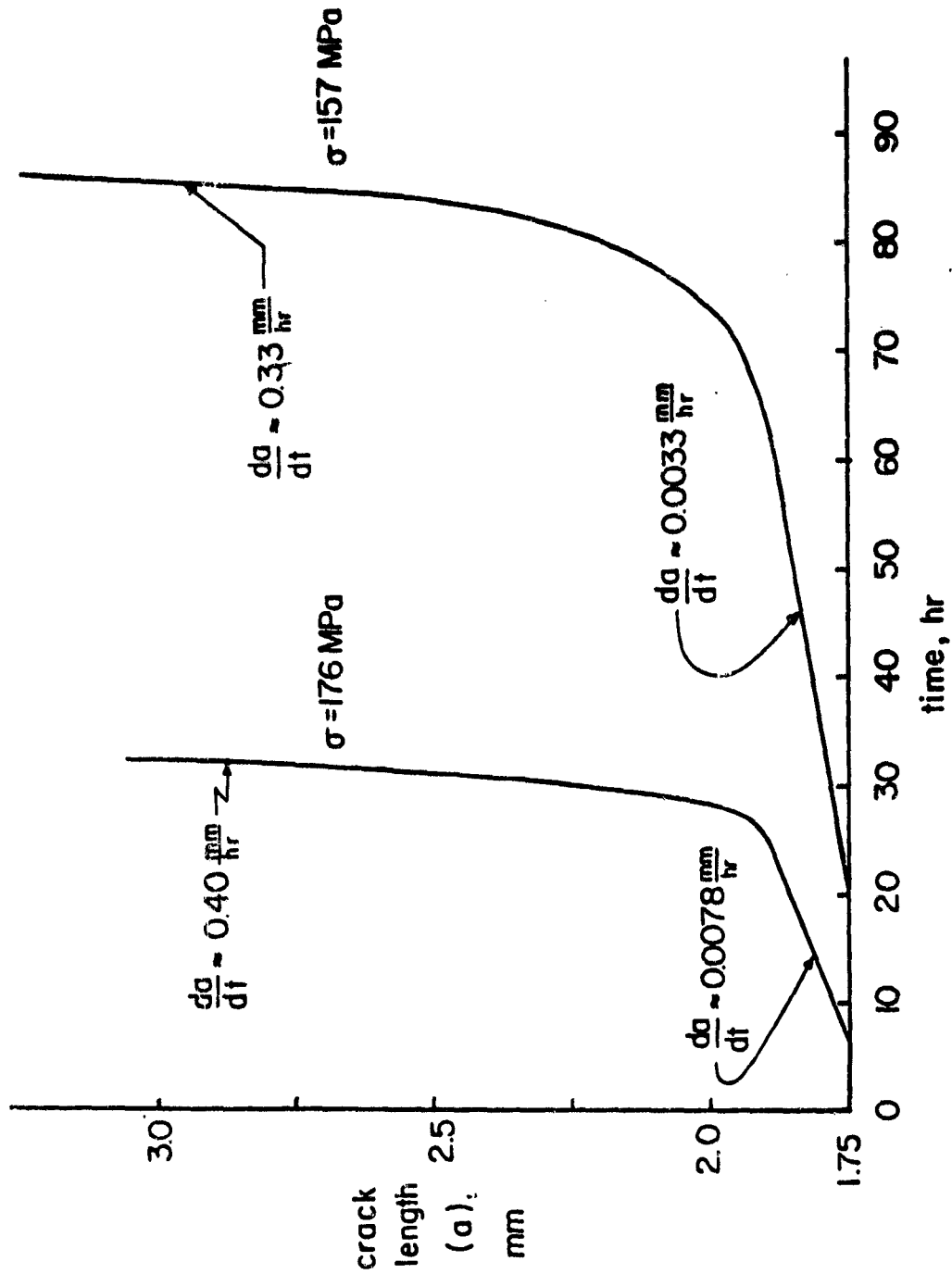
Fig. 5.18 Double-edge-crack specimen crack growth histories (from [77])

that is, that the crack-tip fields are essentially creep steady-state fields even for the most rapid creep crack velocities. These calculations will be a valid check because the input to the calculations is only the remote applied stress and the measured crack velocity history, and does not in any way depend on experimental determination of C_1^* or $(\dot{T}_1)_c$ as did the strip calculations. In fact, Koterazawa and Iwata do not report such measurements in [51].

Analysis of Initial, Low Velocity Crack Growth

This section describes the simulation of the initial portion of the crack velocity histories given in Fig. 5.18. In all of these calculations, the entire load is applied elastically at t = 0 and held constant throughout the subsequent creep solution steps. The convergence of $(\dot{T}_1)_c$ and C_1^* to their steady-state values is shown in Fig. 5.19, with the dashed lines in the C_1^* plots denoting the degree of path-dependence. It is seen that steady-state conditions are reached between a half and one hour after the load is applied. (Table 5.3 summarizes the computational aspects of this portion of the calculation.) Therefore, it is seen by refereing to Fig. 5.18 that crack growth does not begin in the two specimens until well after steady-state conditions are reached. Since the current calculations assume small displacements and infinitesimal strains, and since only the strain and displacement magnitudes depend on time once steady-state is reached, there is no reason to continue the numerical calculations to the crack initiation times indicated by the experimental results. Therefore, the initial crack propagation is simulated at times after steady-state conditions are reached but much earlier indicated by the experiments.

The crack growth simulation results are shown in Fig. 5.19. The crack increment size for this study was approximately 0.01 mm which is nominally 2.4 percent of the crack-tip element size. It can be seen that only one mesh shift (i.e., crack growth step) was modeled. It is clear from this figure that the time it takes for the specimen to return to steady-state is significantly less
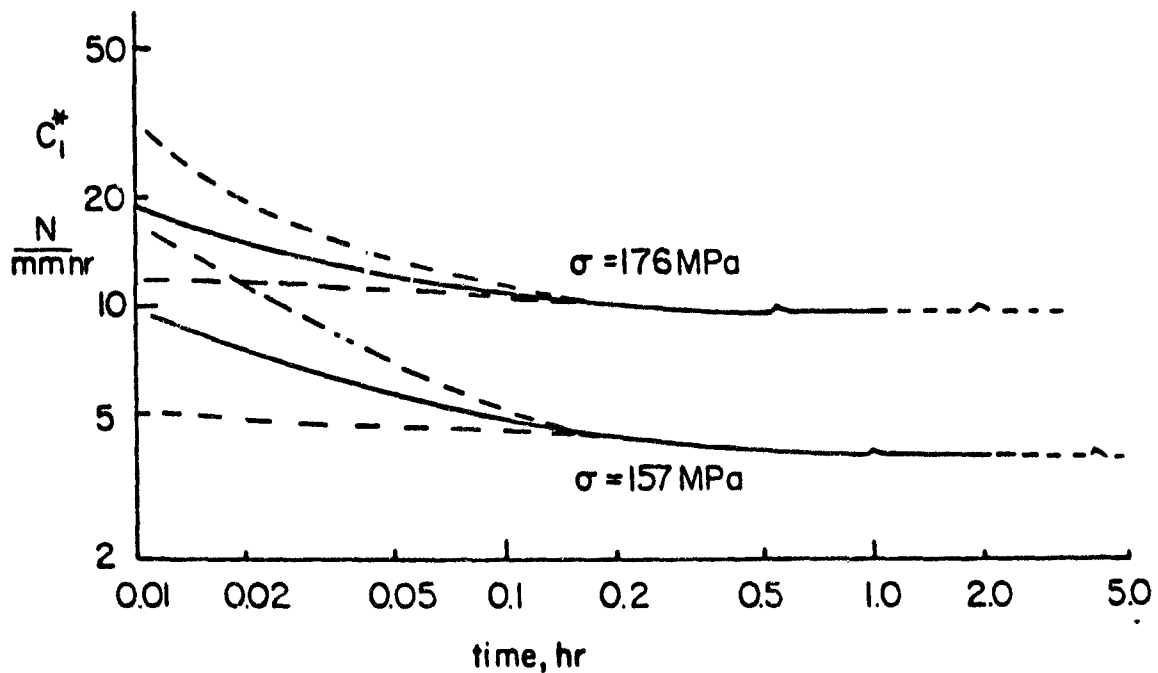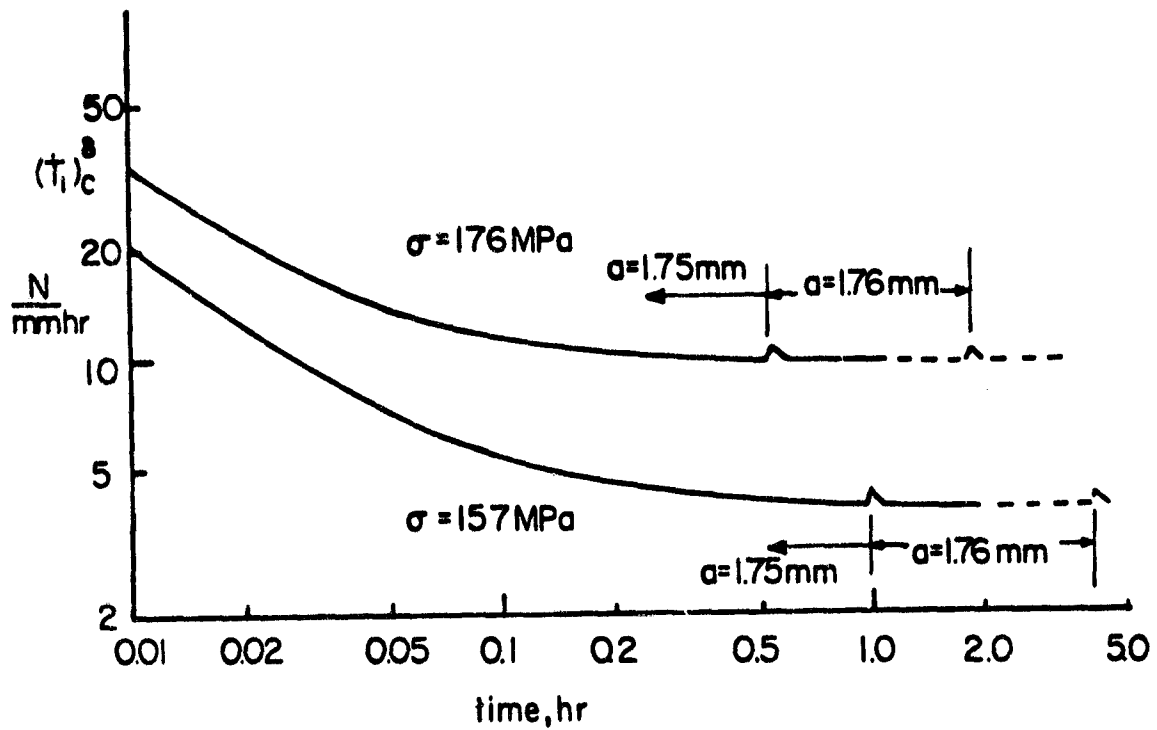
Fig. 5.19 $(\dot{T}_1)_c^\delta$ and C_1^* for non-steady creep, steady-state creep and the first crack growth step of two double-edge-crack analyses

than the time to the next crack growth increment (indicated by dashed lines).
Therefore, the initial portion of the crack growth histories of Fig. 5.18 are
clearly occurring under essentially steady-state conditions and thus C_1^* as
well as $(\dot{T}_1)_c$ are valid crack-tip parameters. Since an increase in C_1^* re-
sults in a more rapid return to steady-state conditions, the above conclusion
will remain valid for the initial constant velocity portions of the curves of
Fig. 5.18.

When crack growth occurs so slowly that the crack-tip is essentially
at steady-state, the crack-tip field does not depend on the history of the
specimer. Therefore, assuming steady-state conditions continue to exist, it is
possible to skip to the final stages of crack growth without modeling the
intermediate crack growth. If it is found that crack growth is still slow
enough for steady-state conditions to exist, then it seems reasonable to expect
that the bevaivor at intermeiate crack lengths is also of a steady-state type.
The following describes the results of this procedure when applied to the
two double-edge-crack specimens.

Analysis of Final Stage of Crack Growth

To analyze the final stage of crack growth, the crack length is in-
creased to 2.75 mm and the process of applying the load elastically and creeping
to steady-state is repeated. Table 5.3 summarizes the computational aspects of
this process. The convergence of $(\dot{T}_1)_c^\delta$ and C_1^* to their steady-state values is
shown in Fig. 5.20. Having reached steady-state, the cracks are grown at the
rate suggested by the last portion of the crack histories (Fig. 5.18) as shown
in Fig. 5.20. The significant increase in the frquency of mesh shifting (compared
to that in Fig. 5.19) due to the velocity increase makes the details of the
curve difficult to distinguish in this figure. However, the time step size is
such that six or seven steps occur between each crack growth increment. Unlike
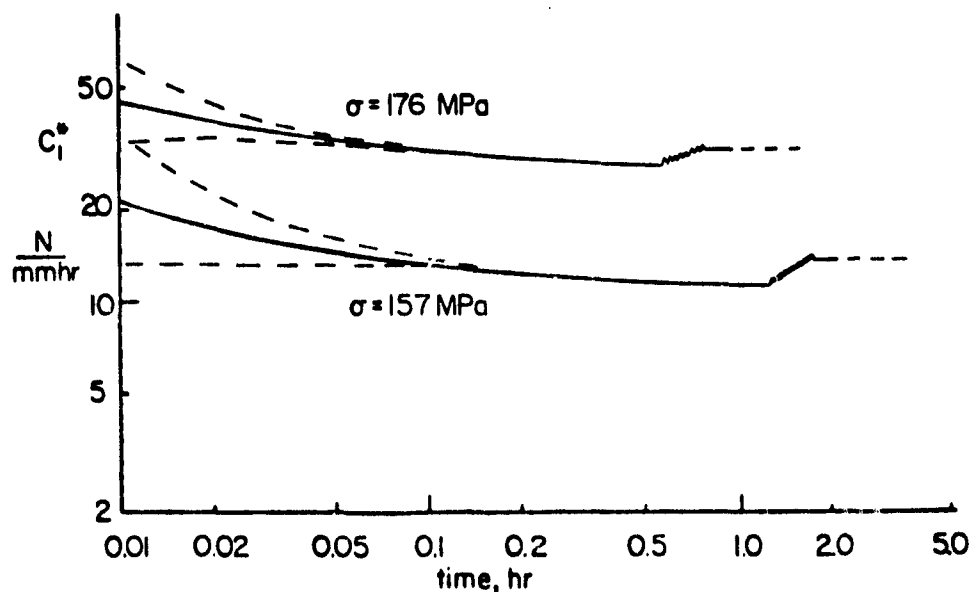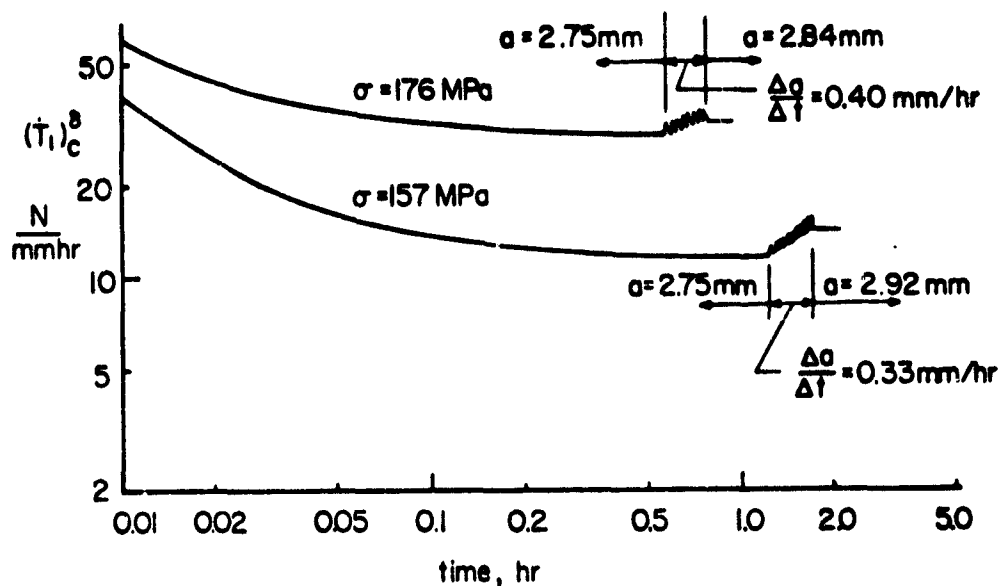the strip problem, the values of $(\dot{T}_1)_c^\delta$ and C_1^* are clearly increasing during

Fig. 5.20 $(\dot{T}_1)_c^{\delta}$ and C_1^* from analyses on final stage of
crack propagation in two
double-edge-crack specimens

this crack propagation process.

It is necessary to determine whether this increase in the crack-tip parameters is due to the crack-tip no longer being at steady-state conditions or whether it is due to the increase in crack length. This is accomplished by continuing the calculation without further crack extension. If the value of the parameters do not change significantly with time, this means the increase was largely due to the crack length increase and that crack growth is still occurring under essentially steady-state conditions. Examination of the final portions of the curves of Fig. 5.20 shows that this is the case.

Based on this analysis; it appears that the conclusions reached as a result of the strip calculations are still valid. Since, (i) the strip analyses are much less expensive than this analysis of the double-edge-crack geometry, (ii) the steady-state C_1^* for the strip is easily obtained analytically and (iii) the crack-tip parameters do not depend on crack length for the strip geometry, it seems that similar studies for other materials and/or other temperatures could most effectively be accomplished through the use of the strip geometry. The need for such studies follows from the vast simplification of fracture analysis and prediction which results if crack growth occurs under steady-state conditions. More will be said about this point in the conclusions.

SECTION VI

CONCLUSIONS

Summary of Results

A finite element model has been derived which is generally applicable to viscoplastic material models. This model uses an initial strain approach which reduces computation time spent on forming and decomposing stiffness matrices and also circumvents the problem of element incompressiblity constraints. Through special features, including a correction term in the finite element equation, this model provides for improved adherence to the postulated constitutive behavior (as compared to the standard initial strain approach) and allows time steps which approach in size those used in tangent stiffness methods. The accuracy and efficiency of this model with eight-node isoparametric elements and the quarter-point crack-tip element approach have been verified through several calculations for a compact specimen geometry and a strip geometry. Also, a method of simulating crack growth through shifting of the quarter-point singularity elements and periodic remeshing has been described and demonstrated.

It has been shown that despite the fact that C^*_1 characterizes the crack-tip fields under steady-state creep conditions, it does not have an energy or energy rate interpretation. A related path-independent integral parameter $(\dot{T}_1)_c$, however, does have the energy rate interpretation commonly

attributed to C_1^*. Since experimentalists use this energy interpretation to correlate creep crack growth rates, it appears that $(\dot{T}_1)_c$ (as opposed to C_1^*) is gaining acceptance as a useful creep crack growth rate criterion. Furthermore, $(\dot{T}_1)_c$ does not rely on the existence of steady-state creep conditions and thus might be expected to be a valid criterion even if creep crack growth should occur at rates which preclude the existence of steady-state creep conditions at the crack-tip.

A creep crack growth simulation for 304 stainless steel has shown that for realistic load levels and corresponding crack speeds the crack-tip field is essentially at a steady-state creep condition. This means that for this material, the propagating crack-tip field is largely unaffected by the history of crack growth or the history of loading. This feature can greatly reduce the analysis required for predicitng creep crack growth behavior in a component as can be seen from the following suggested methodology.

We assume that the crack propagation speed $\frac{da}{dt}$ is related to $(\dot{T}_1)_{css}$ (i.e., $-\frac{dE}{dt}$) through the power law suggested by experimental data [23, 24].

$$\frac{da}{dt} = \alpha[(\dot{T}_1)_{css}]^\beta \qquad (6.1)$$

Next we determine (e.g., by steady-state creep finite element analysis) $(\dot{T}_1)_{css}$ as a function of crack length. Because of the assumed steady-state crack-tip behavior, this can be accomplished by considering several discrete crack lengths and then fitting a curve. No crack growth simulation procedures are necessary. Combining (6.1) with this result provides the following relationship between time and crack length:

$$t = \int_{a_o}^{a(t)} \frac{[(\dot{T}_1)_{css}]^{-\beta}}{\alpha} da + t_i \qquad (6.2)$$

where a_o is the initial crack length and t_i is the time when crack growth initiates.

The only unknown quantity in (6.2) is the initiation time t_i. If the initiation time for creep crack growth is assumed to be negligible (as might be suggested from the results of [9,10]) then (6.2) immediately provides the predicted crack growth history.

Vitek [11] does not consider t_i to be negligible based on several experiments (compact and double-edge-crack specimens) on two CrMoV steels. Using a dislocation model he further concludes that a measure of crack opening displacement (COD) correlates well with the initiation of crack growth in these experiments. If the same conclusion is valid for 304 stainless steel, then one can presumably predict t_i based on a transient finite element analysis of the initial flawed configuration and a critical value of COD. If initiation occurs long after steady-state conditions are reached, it is then reasonable to estimate t_i using the rate of COD obtained from a steady-state finite element solution. The use of (6.2) and of the critical COD concept has not been investigated in this study.

All of the creep calculations have used the constitutive law which is obtained by generalizing the Norton constitutive law to three dimensions. Whereas this law is a good representation of steady-state creep behavior, it does not, in general, represent the primary stage of creep. Future work should include a study of other creep constitutive laws (such as that of Bodner and Partom [32]). Also, the present model is derived on the assumption that displacements are small and strains infinitesimal. The strains in the vicinity of the crack-tip for the present calculations with 304 stainless steel material properties are on the order of 5-10% and therefore suggest that a finite strain formulation may be more appropriate. A study should be undertaken to examine this aspect of the model.

As noted previously, the creep crack growth prediction methodology expressed in (6.1) and (6.2) has not been tested. A study to assess the

utility of this methodology should therefore be undertaken. This study should consider crack growth initiation as well as crack propagation and should include a range of load levels and several specimen geometries. If the methodology is found to be successful for constant applied loads, then the study should be extended to consider more general load histories.

APPENDIX A

Existence of Limits for Contour Integral Definitions

This appendix discusses the existence of the various limits which have been taken in defining $(\Delta\underline{T})_c$, $(\underline{\dot{T}})_c$ and $\underline{C}^*$. In considering these limits, we make use of the generally accepted result (see [6] for example) that the strain energy density quantities W and $\dot{W}$ as well as the quantity W^* behave as $1/r$ in the vicinity of the crack-tip. This is assumed to be valid for nonsteady as well as steady-state creep and also for the elastic state existing at $t = 0$.

Based on the known asymptotic behavior at the crack-tip (i.e., the HRR fields) the limits of Γ_ϵ contour integrals for equations (2.11,13,14,25,30, 40,44) can be written in the following form provided one takes Γ_ϵ as being a circular contour centered at the crack-tip.

$$\underset{\epsilon\to 0}{Lt}\ \int_{\Gamma_\epsilon} (\frac{1}{\epsilon})\hat{f}(\epsilon,\theta)\epsilon\,d\theta = \int_{-\pi}^{\pi} f(\theta)\,d\theta \tag{A.L}$$

The nonsingular function $\hat{f}(\epsilon,\theta)$ becomes equal to $f(\theta)$ when the limit is taken and reflects the asymptotic nature of the HRR fields.

In the following we limit the discussion to symmetric problems involving only mode I crack-tip deformation. Further, we assume that crack surface tractions and body forces are identically zero. With these conditions, we need only consider $(\Delta T_1)_c$ and we can therefore rewrite (2.11)

$$(\Delta T_1)_c = \underset{\epsilon\to 0}{Lt}\ \int_{\Gamma_\epsilon} [n_1\Delta W - n_j(\tau_{j1} + \Delta t_{j1})\Delta e_{11}]dS \tag{A.2}$$

$$\equiv \int_{\Gamma_{234}} [n_1 \Delta W - n_j (\tau_{j1} + \Delta t_{j1}) \Delta e_{11}] dS$$

$$- \underset{\epsilon \to 0}{Lt} \int_{V_t - V_\epsilon} \frac{\partial \tau_{11}}{\partial y_1} \Delta e_{ij} dV$$

Now consider the limit of the $V_t - V_\epsilon$ integral of (A.2). Inspection of this integral shows that it can be put into the form:

$$C + \underset{\epsilon \to 0}{Lt} \int_{V_t' - V_\epsilon} \frac{1}{r^2} \hat{g}(r,\theta) r dr d\theta \qquad (A.3)$$

$$= C + \underset{\epsilon \to 0}{Lt} \int_\epsilon^R \int_{-\pi}^\pi (\frac{1}{r}) \hat{g}(r,\theta) d\theta dr$$

where V_t' is a small circular region centered at the crack-tip and C is the integral over the region $V_t - V_t'$. The function $\hat{g}(r,\theta)$ is a nonsingular function which becomes $g(\theta)$ in the limit as r goes to zero, where $g(\theta)$ is known in terms of the HRR fields. Upon a first inspection of (A.3) one is tempted to conclude that the limit does not exist since the integrand has a non-integrable singularity at $r = 0$. If, however, we look at the right equality of (A.2) it is seen that this conclusion results in a contradiction. Since we have shown that the limit of the integral on Γ_ϵ does exist (and therefore (A.2) requires that the limit of the integral over $V_t - V_\epsilon$ must exist). A re-inspection of (A.3) shows that the only way for this apparent contraction to be resolved is if the $\hat{g}(r,0)$ of (A.3) has the following property:

$$\int_{\pi-}^\pi \hat{g}(r,0) d\theta \quad \underset{r \to 0}{\longrightarrow} \int_{-\pi}^\pi g(0) d\theta = 0 \qquad (A.4).$$

If function $g(0)$ is known explicitly for the linear elastic case and therefore (A.4) can be directly verified. For the HRR field $g(0)$ is not known explicitly and therefore (A.4) can only be verified numerically.

For infinitesimal strain, nonlinear elasticity, the following relation provides an alternative to verifying (A.4) directly

$$\int_{V-V_\epsilon} \frac{\partial \sigma_{ij}}{\partial x_k} \Delta \epsilon_{ij} dV = \int_{\Gamma_{234}} n_j \Delta \sigma_{ij} \frac{\partial u_i}{\partial x_k} dS - \int_{\Gamma_v} n_j \Delta \sigma_{ij} \frac{\partial u_i}{\partial x_k} dS \quad (A.5)$$

The relation (A.5) (which assumes zero crack surface tractions and no body forces) illustrates that this volume integral of type (A.3) can be expressed in terms of the contour integral of type (A.1). The relation (A.5) can be verified through the divergence theorem, the linear momentum balance condition and the following identities:

$$\frac{\partial \sigma_{ij}}{\partial x_k} = \frac{\partial}{\partial x_k} \left(\frac{\partial W}{\partial \epsilon_{ij}} \right) = \frac{\partial}{\partial \epsilon_{ij}} \left(\sigma_{mn} \frac{\partial \epsilon_{mn}}{\partial x_k} \right) = \frac{\partial \sigma_{mn}}{\partial \epsilon_{ij}} \frac{\partial \epsilon_{mn}}{\partial x_k}$$

$$\frac{\partial \sigma_{mn}}{\partial \epsilon_{ij}} \Delta \epsilon_{ij} = \Delta \sigma_{mn}$$

$$\frac{\partial}{\partial x_n} \left(\Delta \sigma_{mn} \frac{\partial u_m}{\partial x_k} \right) = \Delta \sigma_{mn} \frac{\partial \epsilon_{mn}}{\partial x_k}$$

APPENDIX B

Numerical Difference Between $(\dot{T}_1)_{css}$ and C_1^*

The purpose of this appendix is to give some examples to illustrate the numerical difference between $(\dot{T}_1)_{css}$ and C_1^* as given by (2.48). Using (2.50), (2.49a) and (2.51), we have

$$\frac{(\dot{T}_1)_{css}}{T_1^*} = \frac{I^*}{I} = 1 + \frac{1}{(n+1)I} \int_{-\pi}^{\pi} \tilde{\sigma}_{eq}^{n+1}(\theta)\cos\theta\,d\theta \tag{B.1}$$

The values tabulated in Table B.1 were computed __approximately__ from values of I and plots of $\tilde{\sigma}_{eq}(\theta)$ given in [6] and should be viewed accordingly.

Table B.1 Comparison of $(\dot{T}_1)_{css}$ and C_1^*

	Plane Strain		Plane Stress	
	n = 3	n = 13	n = 3	n = 13
$\dfrac{(\dot{T}_1)_{css}}{C_1^*}$	0.98	1.00	1.11	1.14

It is seen that for the range of n commonly encountered, $(\dot{T}_1)_{css}$ and C_1^* are numerically very similar for plane strain but differ significantly for plane stress.

$C-2$

APPENDIX C

Numerical Methods for Evaluation of Contour Integrals

The numerical procedures for evaluating J_1 as defined by (2.27), $(\Delta T_1)_c$ as defined by (2.14) and C_1^* as defined by (2.31) are described in the following.

General Procedures

In studying the contour integral paths indicated in the finite element meshes of Figs. 5.2,3,5 (dashed lines) it is seen that the paths always pass through the centers of elements as opposed to along their edges. This procedure has been adopted so as to benefit from the presumably more accurate solution within the elements. Each element contour is divided into two segments with the integration being accomplished by two point Gaussian quadrature. All of the integrations are performed in the element local coordinates.

The J_1-Integral for Linear Elastic Analyses

The contour integral portion of (2.27) involves the stresses, τ_{ij}, and the displacement derivatives, $\partial u_j / \partial x_1$. Both of these quantities can be evaluated at the required Gauss points through the element nodal displacements and simple manipulations with element matrices. In the current study, J_1 is only considered as a parameter for linear elastic material behavior and therefore $U = (1/2)\sigma_{ij}\epsilon_{ij}$.

The C_1^*-Integral

The C_1^* integral of (2.31) consists only of a contour integral. The W^* of (2.31) is evaluated using (2.43). The gradient rates are approximated by

$$\frac{\partial \dot{u}_1}{\partial x_1} \doteq \frac{1}{\Delta t} \frac{\partial \Delta u_1}{\partial x_1}$$

and therefore are average rates for the increment as opposed to the rates at the end of the increment. The contour integration procedure for C_1^* is as described above and uses two point quadrature for each element segment. Whereas stresses are easily computed at the required contour Gauss points in the elastic case, the stresses must be computed incrementally in creep analyses and therefore stress information must be stored for each contour integration point unless nonstandard element interpolations are used. In the present study, the stresses at the contour Gauss points are interpolated from the 2x2 element Gauss points through bilinear Lagrangian interpolation (in local coordinates), thus eliminating the need for additional storage.

The $(T_1)_c$-Integral

In the evaluation of (2.14) it is understood that τ_{ij} are the stresses at the beginning of the time increment being considered. The procedures for evaluating the contour integral portion of (2.14) are the same as used in evaluating C_1^*. The incremental stress-work density, ΔW, is computed from

$$\Delta W = (\tau_{ij} + \frac{1}{2} \Delta\tau_{ij})\Delta\epsilon_{ij}$$

The stress derivative appearing in the area integral of (2.14) is evaluated based on the 2x2 element Gauss point values and the assumption that the stresses are distributed bilinearly with respect to element local coordinates. Elements which are entirely within V_t are integrated with the usual 2x2 Gauss quadrature. Elements which are only partially within V_t have each applicable quadrant integrated by one point Gauss quadrature.

APPENDIX D

Simulation of Crack Extension

Modeling the propagation of a crack using the finite element method requires some special procedure for representing the creation of new crack surface. A common procedure is to relax the nodal forces at the crack-tip node, thus in effect allowing the crack to extend to the next node along its path of propagation. This relaxation process can be accomplished in one time step but usually is allowed to extend over several time steps due to the large change in nodal forces which is inherent in the process. The major attraction of this node-release procedure is its simplicity. There are two drawbacks of this procedure which resulted in an alternate procedure being adopted in this study. The first is that the increment in crack growth is directly determined by the nodal spacing in the mesh, therefore restricting the flexibility one has in selecting a time step size, the mesh size and /or the number of nodal force relaxation steps. The second and perhaps more important drawback is that the method is not adaptable to models which use crack-tip singularity elements.

A typical mesh in the vicinity of a crack-tip is shown in Fig. D.1. The region A represents the region being modeled by singular crack-tip elements which in the present case remain centered on the crack-tip. The Type B elements are eight-noded isoparametric elements which distort so that the region A can remain centered on the crack-tip. The sequence of element configurations in Fig. D.1 illustrates the shifting/remeshing procedure used in [53, 54] and adopted here. The region A is moved by shifting nodes without altering element connectivity until the Type B element ahead of the region A becomes
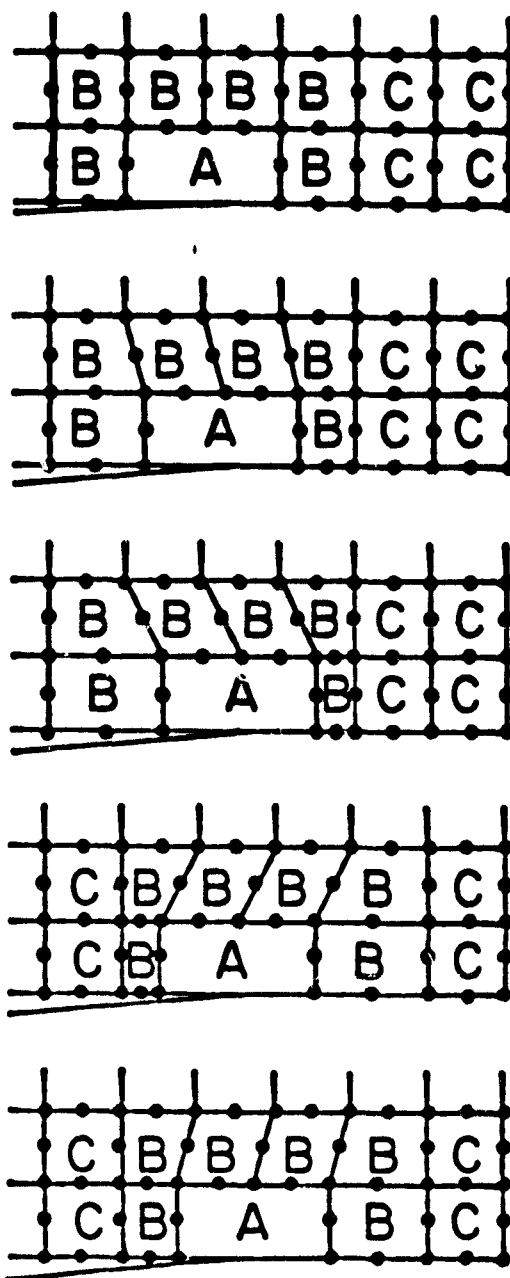
Fig. D.1   Example of mesh shifting/remeshing procedure
for simulation of crack growth

overly distored. At this point, the elements in the vicinity are redefined

so that further shifting is possible. It can be seen that this procedure allows

the increment in crack length to be arbitrarily small and does not involve

release of nodes in the same sense as for the previously described node-

release procedure.

The added flexibility afforded by this shifting procedure does require

some additional work. For example, in the creep crack growth application, nodal

displacements and element integration point stresses are interpolated. The

method of interpolation which is employed in this procedure is discussed next.

We consider that the solution at time t, has been obtained and we now

must find the solution at time t_2. During the interval (t_1, t_2) the crack has

grown by an amount Δa. Since the crack growth simulation procedure requires

that nodes be shifted, and since the solution at t_1 must be represented in terms

of nodal and Gauss point quantities for the shifted mesh, it is necessary to

submit the affected nodes and Gauss point to an interpolation or fitting pro-

cedure.

The simplest interpolation procedure for nodal displacements and the one

used in [53,54] as well as for calculations in the present study is one which

directly uses the element shape functions. In this method, the nodal positions

for t e mesh at t_2 are located in the mesh at t_1. Knowing which element

of the mesh at t_1 encompasses this new node position allows the immediate

calculation of displacements by use of the element shape functions and the

nodal quantities for the mesh at t_1. While this is a consistent procedure

for transferring the solution at t_1 to the mesh at t_2, it should be understood

that the transfer cannot be perfect. That this must be the case can be seen

by considering that spatial derivatives of displacements, etc., are not continu-

ous across element boundaries. Since the element boundaries change position

during the shifting process, points which had continuous derivatives at t_1 will

have discontinous derivatives in the mesh at t_2 and vice-versa.

When the mesh is shifted, the element Gauss points are also shifted; this means the Gauss points represent different material points before and after the shift. In order that the new Gauss point stresses accurately represent the current stress state, it is necessary to interpolate stresses for the new Gauss point locations using the old Gauss point values and locations. The procedure for doing this is to assume the element stresses are distributed bilinearly with respect to the element local coordinates. Then it becomes possible to use bilinear Lagrangian interpolation polynomials and the 2x2 element Gauss point stresses to interpolate within each element. For all creep crack growth calculations in this study, the crack growth increment sizes were chosen small enough that the new Gauss point stresses for each shifted element were always the result of interpolation within that same element.

APPENDIX E

Analytical Evaluation of C_1^* for the Strip Problem

This appendix briefly outlines the anlaytical evaluation of C_1^* for two infinite strip problems and then summarizes the results in tabular form. The first strip problem is that which is illustrated in Fig. 5.3. We shall refer to this problem as Case A. The second problem, or Case B, is similar to Case A in every respect except the top and bottom edges of the strip are "clamped" rather than "on rollers". These boundary conditions are summarized as follows:

Case A: $\dot{u}_y(x,h) = -\dot{u}_y(x,-h) = \dot{\delta}$ (E.1)

$\tau_{xy}(x,h) = \tau_{xy}(x,-h) = 0$

Case B: $\dot{u}_y(x,h) = -\dot{u}_y(x,-h) = \delta$ (E.2)

$\dot{u}_x(x,h) = \dot{u}_x(x,-h) = 0$

The crack surfaces are traction-free in both cases.

We can select a C_1^*-integral contour which allows C_1^* to be evaluated quite easily.[1] Consider a contour of rectangular shape which coincides with the top and bottom edges of the strip, extends far enough ahead of the crack-tip so as to be in a steady-state stress field which is unaffected by the presence of the crack-tip, and extends far enough behind the crack-tip so as to be in stress-free material. We now evaluate C_1^*, as defined by (2.31), through the use of this contour. It can be seen that for both Case A and Case B, the horizontal portions of the contour at $y = \pm h$ do not contribute to the

---

[1]This procedure parallels that used by Rice [50] for the evaluation of J_1 in a similar elastic strip problem.

integral, nor does the portion in the stress-free material. At the veritcal portion of the contour ahead of the crack-tip, the only non-zero term is that involving W^*. Therefore, it is seen that for both Case A and Case B we have

$$C_1^* = 2W_\infty^* h \tag{E.3}$$

where W_∞^* implies W^* existing far ahead of the crack-tip. Using the boundary conditions (E.1) and (E.2) and the assumption of steady-state conditions, it is possible to evaluate the remote steady-state stresses, τ_{ij}. Using (2.43) results in W_∞^* and thus C_1^*. The results of this exercise are summarized in Table E.1.

The corresponding linear elastic strip problem which is obtained by replacing the displacement rate boundary conditions by the corresponding displacement boundary onditions has been treated in a similar manner. These results are also given in Table E.1.

Table E.1 Analytical Solutions for the Infinite Strip Problem

	Steady-State Creep		Linear Elasticity
	$B\left(\frac{h}{\delta}\right)\left(\tau_{yy}^{\infty}\right)^{n}$	$\left(\frac{h}{\delta}\right)\left[C_{1}\ast\left(\frac{n+1}{2nh}\right)B^{\frac{1}{n}}\right]^{\frac{n}{n+1}}$	$\frac{1}{E}\left(\frac{h}{\delta}\right)\tau_{yy}^{\infty}$ and $\frac{1}{E}\left(\frac{h}{\delta 2}\right)J_{1}$
Case A			
plane stress	1	1	1
plane strain	$\left(\frac{2}{\sqrt{3}}\right)^{n+1}$	$\frac{2}{\sqrt{3}}$	$\frac{1}{1-\nu^{2}}$
Case B			
plane stress	$\left(\frac{2}{\sqrt{3}}\right)^{n+1}$	$\frac{2}{\sqrt{3}}$	$\frac{1}{1-\nu^{2}}$
plane strain	*	*	$\frac{1-\nu}{(1+\nu)(1-2\nu)}$

*This case does not have a steady-state solution since the boundary conditions require a volumetric strain rate.

REFFRENCES

[1] Srawley, J.E. and Brown, W.F., "Fracture Toughness Testing Methods", ASTM STP 381, 1965, pp. 133-145.

[2] Brown, W.F. and Srawley, J.E., "Plane Strain Crack Toughness Testing of High Strength Metallic Materials", ASTM STP 410, 1966.

[3] Begley, J.A. and Landes, J.D., "The J-Integral as a Fracture Criterion", ASTM STP 514, 1972, pp. 1-20.

[4] Landes, J.D. and Begley, J.A., "Test Results from J-Integral Studies: An Attempt to Establish a J_{Ic} Testing Procedure", ASTM STP 560, 1974, pp. 170-186.

[5] Westergaad, H.M., "Bearing Pressures and Cracks", J. Appl. Mech., 61, 1939, pp. A49-53.

[6] Hutchinson, J.W., "Singular Behavior at the End of a Tensile Crack in a Hardening Material", J. Mech. Phys. Sol., 16, 1968, pp. 13-31

[7] Rice, J R., Rosengren, G.F., "Plain Strain Deformation Near a Crack Tip in a Power-Law Hardening Material", J. Mech. Phys. Sol., 16, 1968, pp. 1-12.

[8] Irwin, G.R., "Fracture Mechanics", Structural Mechanics, (Proceedings of First Naval Symposium), Pergamon Press, 1960, pp. 557-594.

[9] Nikbin, K.M., Webster, G.A. and Turner, C.E., "Relevance of Nonlinear Fracture Mechanics to Creep Cracking", ASTM STP 601, 1976, pp. 47-62.

[10] Harper, M.P. and Ellison, E.G., "The Use of the C* Parameter in Predicting Creep Crack Propagation Rates", J. of Strain Analysis, Vol. 12, Nov. 3, 1977, pp. 167-179.

[11] Vitek, V., "A Theory of the Initiaion of Creep Crack Growth", Int. J. of Fracture, Vol. 13, No. 1, 1977, pp. 39-50.

[12] Shih, C.F. and Kumar, V., "Estimation Technique for the Prediction of Elastic-Plastic Fracture of Structural Components of Nuclear Systems," Contract RP1237-1, First Seminannual Report for Electric Power Research Institute, General Electric Co., Report, 1979.

[13] Zahoor, A. and Paris, P.C., "Ductile Tearing Instability of a Center-Cracked Panel of an Elastic-Plastic Strain Hardening Material", Engng. Materials and Technology, 103, 1981, pp. 46-54.

[14] Hutchinson, J.W. and Paris, P.C., "Stability Analysis of J-Controlled Crack Growth", ASTM STP 668, 1979, pp. 37-64.

[15] Aihara, S., Machida, S. and Kanazawa, T., "A Study on Unstable Ductile Fracture", Advances in Fracture Research, Vol. 5, Francois, D., (Ed.), Proceedings Fifth Intl. Conf. on Fracture, Cannes, 1981, pp. 2329-2336.

[16] Kanninen, M.F., Hahn, G.T., Broek, D., Stonesifer, R.B., Marchall, C.W., Abou-Sayed, I.S. and Zahoor, A., "Development of a Plastic Fracture Methodology", Battelle _olumbus Laboratory Report to ERPI, Contract 601-1, March 1981.

[17] Kanninen, M.F., Rybicki, E.F., Stonesifer, R.B., Broek, D., Rosenfield, A.R., Marschall, C.W. and Hahn, G.T., "Elastic-Plastic Fracture Mechanics for Two Dimensional Stable Crack Growth and Instability Problems", ASTM STP 668, 1979, pp. 121-150.

[18] Abou-Sayed, I.S., Marschall, C.W. and Kanninen, M.F., "An Assessment of the Fracture Toughness Associated with Flat and Slant Crack Growth in A533B Steel", Advances in Fracture Research, Vol. 1, Francois, D. (Ed.), Proceedings Fifth Intl. Conf. on Fracture, Cannes, 1981, pp. 227-234.

[19] Abou-Sayed, I.S., Broek, D., Forte, T.P. and Stonesifer, R.B., "Plane Stress Fracture under Biaxial Loading", Advances in Fracture Research, Vol. 4, Francois, D. (Ed.), Proceedings Fifth Intl. Conf. on Fracture, Cannes, 1981, pp. 1707-1714.

[20] Fu, L.S., "Creep Crack Growth in Technical Alloys at Elevated Temperature – A Review", Engng. Fracture Mech., Vol. 13, 1980, pp. 307-330.

[21] Landes, J.D. and Begley, J.A., "A Fracture Mechanics Approach to Creep Crack Growth", ASTM STP 590, 1976, pp. 128-148.

[22] Branco, C.M. and Radon, J.C., "Analysis of Creep Cracking by the J-Integral Concept", Engng. Aspects of Creep, Proc. Conf. at Univ. Sheffield, I. Mech. E., 1980, pp. 43-48.

[23] Ohji, K., Ogura, K. and Kubo, S., "The Application of Modified J-Integral to Creep Crack Growth in Austentic Stainless Steel and Cr-Mo-V Steel," Engng. Aspects of Creep, Proc. Conf. at Univ. Sheffield, I. Mech. E., 1980, pp. 9-16.

[24] Koterazawa, R. and Mori, T., "Applicability of Fracture Mechanics Parameters to Crack Propagation Under Creep Condition", J. Engng. Materials and Technology, Vol. 99, Series H, No. 4, 1977, pp. 298-305.

[25] Hoff, N.J., "Approximate Analysis of Structures in the Presence of Moderately Large Creep Deformations", Quart. Appl. Math., 12, 1954, pp. 49-55.

[26] Goldman, N.L. and Hutchinson, J.W., "Fully Plastic Crack Problems: The Center-Cracked Strip Under Plane Strain", Int. J. Solids Structures, 11, 1975, pp. 575-591.

[27] Atluri, S.N., "Path-Independent Integrals in Finite Elastiicty
      and Inclasticity, with Body Forces, Inertia, and Arbitrary Crack-
      Fuce Conoltions", Report No. GIT-CACM-SNA-81-8, Georgia Institute of
      Technology, March, 1981, also Engng. Fracture Mech., (in press).

[28] Riedel, H. and Wagner, W., "The Growth of Macroscopic Cracks in Creeping
      Materials", Advances in Fracture Research, Vol. 2, Francois, D. (Ed.),
      Proceedings Fifth Intl. Conf. on Fracture, Cannes, 1981, pp. 683-390.

[29] Hui, C.Y. and Riedel, H., "The Asymptotic Stress and Strain Field Near
      the Tip of a Growing Crack under Creep Conditions", Brown University
      Engineering Report MRL E-117.

[30] Ohtani, R. and Nakamura, S., "Crack Propagation in Creep (Finite Element
      Analysis)", Journal of the Society of Materials Science, Japan, Vol.
      25, No. 275, 1976.

[31] Hinnerichs, T.D., Viscoplastic and Creep Crack Growth Analysis by the
      Finite Element Method, doctoral dissertation, Air Force Institute of
      Technology, 1980.

[32] Bodner, S.R. and Partom, Y., "Constitutive Equations for Elastic-
      Viscoplastic Strain Hardening Materials", J. Appl. Mech., 42, 1975,
      pp. 385-389.

[33] Ehlers, R. and Riedel, H., "A Finite Element Analysis of Creep Deformation
      in a Specimen Containing a Macroscopic Crack", Advances in Fracture
      Research, Vol. 2, Fracture, Cannes, 1981, pp. 691-698.

[34] Knowles, J.K. and Sternberg, E., "On a Class of Conservation Laws in
      Linearized and Finite Elastostatics", Archive for Rational Mechanics
      and Analysis, Vol. 44, No. 3, 1972, pp. 187-211.

[35] Atluri, S.N., "On Some New General and Complementary Energy Theorems
      for the Rate Problems of Finite Strain, Classical Elastoplasticity",
      J. of Structural Mechanics, Vol. 8, No. 1, 1980, pp. 61-92.

[36] Riedel, H. and Rice, J.R., "Tensile Cracks in Creeping Solids", Brown
      University Report E(11-1) 3084/64 to U.S. Dept. of Energy, 1979.

[37] Hutchinson, J.W., "Plastic Stress and Strain Fields at a Crack Tip"
      J. Mech. Phys. Solids, Vol. 16, 1969, pp. 337-347.

[38] Perzyna, P., "Fundamental Problems in Viscoplasticity", Advan. Appl.
      Mech., 9, 1966, pp. 243-377.

[39] Bathe, K.J. and Wilson, E.L., Numerical Methods in Finite Element
      Analysis, Prentice-Hall, 1976.

[40] Zienkiewicz, O.C. and Cormeau, I.C., "Viscoplasticity - Plasticity and
      Creep in Elastic Solids - A Unified Numerical Solution Apprach",
      Int. J. for Num. Meth. Engng., 8, 1974, pp. 821-845.

[41]   Nagtegall, J.C., Parks, D.M. and Rice, J.R., "On Numerically Accurate
Finite Element Solutions in the Fully Plastic Range", Comp. Meth. in
Appl. Mech. and Engng., 4, 1974, pp. 153-177.

[42]   Henshell, R.D. and Shaw, K.C., "Crack Tip Finite Elements are Unneces-
sary", Int. J. Num. Meth. Engng., 9, 1975, pp. 495-509.

[43]   Barsoum, R.S., "On the Use of Isoparametric Finite Elements in Linear
Fracture Mechanics", Int. J. Num. Meth. Engng., 10, 1976, pp. 25-37.

[44]   Barsoum, R.S., "Triangular Quarter-Point Elements as Elastic and Perfectly-
Plastic Crack Tip Elements", Int. J. for Num. Meth. Engng., 11, 1977,
pp. 85-98.

[45]   Atluri, S.N., "Higher Order, Special, and Singular Elements, Chapter
4," State of the Art Surveys in the Finite Element Method, Eds., A.K.
Noor and W. Pilkey, ASME special pub., to appear in 1981.

[46]   Ying, L.A., "A Note on the Singularity and the Strain Energy of Singular
Elements", Int. J. for Num. Meth. Engng., 1981, (in press).

[47]   Tracey, D.M. and Cook, T.S., "Analysis of Power Type Singularities
Using Finite Elements", Int. J. for Num. Meth. Engng., 11, 1977, pp.
1225-1233.

[48]   Stern, M., "Families of Consistent Conforming Elements with Singular
Derivative Fields", Int. J. for Num. Meth. Engng., 14, 1979, pp. 409-421.

[49]   Srawley, J.F., "Wide Range Stress Intensity Factor Expressions for
ASTM E399 Standard Fracture Toughness Specimens", Intl. J. Fracture,
12, 1976, pp. 475-476.

[50]   Rice, J.R., "A Path Independent Integral and the Approximate Analysis
of Strain Concentration by Notches and Cracks", J. Appl. Mech., 1968,
pp. 379-386.

[51]   Koterazawa, R. and Iwata, Y., "Fracture Mechanics and Fractography of
Creep and Fatigue Crack Propagation at Elevated Temperature", J. of
Engng. and Technology, 98, 1976, pp. 296-304.

[52]   Tada, H., Paris, P.C. and Irwin, G.R., The Stress Analysis of Cracks
Handbook, Del Research Corporation, Hellertown, Pennsylvania, 1973.

[53]   Nishioka, T. and Atluri, S.N., "Numerical Modelling of Dynamic Crack
Propagation in Finite Bodies, by Moving Singular Elements, Part I -
Theory", J. Appl. Mech., ASME, Vol. 47, No. 3, Sept. 1980, pp. 570-576.

[54]   Nishioka, T. and Atluri, S.N., "Numerical Modeling of Dynamic Crack
Propagation in Finite Bodies, by Moving Singular Elements, Part II -
Results", J. Appl. Mech., ASME, Vol. 47, No. 3, Sept. 1980, pp. 577-583.